

THESIS FOR THE DEGREE OF DOCTOR OF PHILOSOPHY

# Nanoplasmonic Biosensing

## Exploring Unique Possibilities

MAGNUS JONSSON



**CHALMERS**

Department of Applied Physics  
Chalmers University of Technology  
Gothenburg, Sweden 2010

THESIS FOR THE DEGREE OF DOCTOR OF PHILOSOPHY

Nanoplasmonic Biosensing – Exploring Unique Possibilities

Göteborg 2010

ISBN 978-91-7385-463-4

© Magnus Jonsson and the respective publishers

Doktorsavhandlingar vid Chalmers Tekniska Högskola

Ny serie nr. 3144

ISSN 0346-718X

Magnus Jonsson

Division of Biological Physics

Department of Applied Physics

Chalmers University of Technology

SE-412 96 Gothenburg

Sweden

Cover picture:

The curve shows the temporal variation in the plasmon resonance of a nanoplasmonic hole sensor upon supported lipid bilayer formation from lipid vesicles, as illustrated in the schematics to the left of the curve. To the right of the curve is illustrated schematically that a nanoplasmonic hole film is electrically conductive (top) and that the holes can be designed to penetrate through the whole substrate (bottom).

Funding:

This work presented in this thesis was funded by the Swedish Research Council for Engineering Sciences (contract number 2005-3140), the Ingvar grant from the Strategic Research Foundation, Vinnova BioNanoIT program (grant no. 2003-00656), the FP7 project ASMENA, GE Healthcare Biosciences AB, St Jude Medical AB, the Royal Society of Arts and Sciences in Göteborg and the Adlerbert Research Foundation, the Friends of Chalmers, Chalmersska Forskningsfonden, Stiftelsen Långmanska kulturfonden and Ångpanneföreningen's Foundation for Research and Development.

Printed at Chalmers Reproservice, Gothenburg, Sweden, 2010

## Abstract

Bioanalytical sensors are indispensable tools in medical diagnostics and drug discovery as well as for life science research, environmental monitoring and food safety. In essence, they are used to detect and determine the concentrations of specific biomolecules in complex mixtures. One increasingly popular biosensing concept is that based on the peculiar optical properties of metal nanostructures. Such structures possess nanoplasmonic properties, which make them colored. In turn, the color of a nanoplasmonic structure is highly sensitive to changes in the refractive index of the surrounding environment. This makes it possible to monitor biomolecular binding events occurring close to the metal surface through changes in the color of the structure.

In the work presented in this thesis, challenges of current biosensor technologies have been addressed by exploring unique possibilities provided by nanoplasmonic sensors. This includes utilizing the tight confinement of the sensitivity to the surface to investigate structural biomolecular changes. Nanoplasmonic structural sensing was further investigated using combined nanoplasmonic and quartz crystal microbalance (QCM) measurements. This was enabled using a thin gold film perforated with nanoholes, which served as both the nanoplasmonic sensor and one of the electrodes of the QCM sensor.

Even with the most sensitive surface-based sensor, molecules can only be detected if they reach the surface and bind. In fact, the transport of molecules to the sensor surface can be a limiting factor for the performance of a biosensor. In this work, two ways of improving mass transport were investigated: (i) flow-through sensing using nanoplasmonic pores and (ii) directed binding to high-sensitivity nanoscale regions using materials-specific surface modifications. Both concepts were shown to enable a reduction in the sensor response time of more than one order of magnitude compared with conventional diffusion limited binding.

Finally, one reason for the potential of nanoplasmonic sensors stems from their competitive performance combined with relatively simple instrumentation and the possibility for scalable and low-cost fabrication. Steps towards a portable nanoplasmonic sensor device, for example to be used for medical diagnostics at point-of-care, were taken by integrating the opto-electrical conversion directly on the sensor chip. This was achieved by designing the nanoplasmonic sensor structure on an array of photoactive diodes. By simple means, specific protein binding could be detected in a label-free and real-time format through changes in the photocurrent output.

**Keywords:** nanoplasmonics, localized surface plasmon resonance, biosensor, artificial cell membrane, structural sensing, quartz crystal microbalance, nanofabrication, nanoholes, nanopores



In 1959 Richard Feynman explained that “*there is plenty of room at the bottom*”.  
He was probably referring to a nanohole.

## Appended papers

- I Supported Lipid Bilayer Formation and Lipid-Membrane-Mediated Biorecognition Reactions Studied with a New Nanoplasmonic Sensor Template  
Magnus P. Jonsson, Peter Jönsson, Andreas B. Dahlin and Fredrik Höök  
*Nano Letters* 2007, **7**, 11, 3462-3468 (letter)
- II Simultaneous Nanoplasmonic and Quartz Crystal Microbalance Sensing: Analysis of Biomolecular Conformational Changes and Quantification of the Bound Molecular Mass  
Magnus P. Jonsson, Peter Jönsson and Fredrik Höök  
*Analytical Chemistry* 2008, **80**, 21, 7988-7995 (article)
- III Locally Functionalized Short-Range Ordered Nanoplasmonic Pores for Bioanalytical Sensing  
Magnus P. Jonsson, Andreas B. Dahlin, Laurent Feuz, Sarunas Petronis and Fredrik Höök  
*Analytical Chemistry* 2010, **82**, 5, 2087-2094 (article)
- IV Improving the Limit of Detection of Nanoscale Sensors by Directed Binding to High-Sensitivity Areas  
Laurent Feuz, Peter Jönsson, Magnus P. Jonsson and Fredrik Höök  
*ACS Nano* 2010, **4**, 4, 2167-2177 (article)
- V Nanoplasmonic Biosensing with On-chip Electrical Detection  
Francesco Mazzotta, Guoliang Wang, Carl Hägglund, Fredrik Höök and Magnus P. Jonsson  
*Biosensors and Bioelectronics*, doi: 10.1016/j.bios.2010.07.008 (article)

## Related work

- VI Specific Self-Assembly of Single Lipid Vesicles in Nanoplasmonic Apertures in Gold  
Andreas B. Dahlin, Magnus P. Jonsson and Fredrik Höök  
*Advanced Materials* 2008, **20**, 8, 1436-1442 (article)
- VII High-Resolution Microspectroscopy of Plasmonic Nanostructures for Miniaturized Biosensing  
Andreas B. Dahlin, Si Chen, Magnus P. Jonsson, Linda Gunnarsson, Mikael Käll and Fredrik Höök  
*Analytical Chemistry* 2009, **81**, 16, 6572-6580 (accelerated article)
- VIII High-performance Biosensing using Arrays of Plasmonic Nanotubes  
John McPhillips, Antony Murphy, Magnus P. Jonsson, William R. Hendren, Ronald Atkinson, Fredrik Höök, Anatoly V. Zayats and Robert J. Pollard  
*ACS Nano* 2010, **4**, 4, 2210-2216 (article)
- IX Synchronized Quartz Crystal Microbalance and Nanoplasmonic Sensing of Biomolecular Recognition Reactions  
Andreas B. Dahlin, Peter Jönsson, Magnus P. Jonsson, Emanuel Schmid, Ye Zhou and Fredrik Höök  
*ACS Nano* 2008, **2**, 10, 2174-2182 (article)
- X A Method Improving the Accuracy of Fluorescence Recovery After Photobleaching Analysis  
Peter Jönsson, Magnus P. Jonsson, Jonas O. Tegenfeldt and Fredrik Höök  
*Biophysical Journal* 2008, **95**, 11, 5334-5348 (article)
- XI Sealing of Submicrometer Wells by a Shear-Driven Lipid Bilayer  
Peter Jönsson, Magnus P. Jonsson and Fredrik Höök  
*Nano Letters* 2010, **10**, 5, 1900-1906 (letter)

## Reviews, book chapters and patents

- XII Nanoplasmonic Biosensing with Focus on Short-range Ordered Nanoholes in Thin Metal Films  
Magnus P. Jonsson, Andreas B. Dahlin, Peter Jönsson and Fredrik Höök  
*Biointerphases* 2008, **3**, 3, FD30-FD40 (review)
- XIII Nanoplasmonic Device  
Fredrik Höök and Magnus P. Jonsson  
Applicant: GE Healthcare Bio-Sciences AB  
PCT application no: PCT/SE2010/051034 (patent)
- XIV Nanoplasmonic Sensing Combined with Artificial Cell Membranes  
Magnus P. Jonsson, Andreas B. Dahlin and Fredrik Höök  
In Alexandre Dmitriev (Ed.) *Nanoplasmonic Sensors* 2011. New York: Springer (invited book chapter)
- XV Noise Reduction in Nanoplasmon Spectroscopy  
Andreas B. Dahlin and Magnus P. Jonsson  
In Alexandre Dmitriev (Ed.) *Nanoplasmonic Sensors* 2011. New York: Springer (invited book chapter)
- XVI Supported Lipid Bilayers, Tethered Lipid Vesicles, and Vesicle Fusion investigated using Gravimetric, Plasmonic, and Microscopy Techniques  
Fredrik Höök, Gudrun Stengel, Andreas B. Dahlin, Anders Gunnarsson, Magnus P. Jonsson, Peter Jönsson, Erik Reimhult, Lisa Simonsson, and Sofia Svedhem  
*Biointerphases* 2008, **3**, 2, FA108-FA116 (review)

## **My contribution to the appended papers**

- I I designed, optimized and performed the sensor fabrication and experiments, some together with PJ. I conducted most of the analysis except for the FRAP experiments, for which PJ was responsible. I wrote the main part of the paper.
- II I took part in the optimization of the combined sensor setup and the sensor fabrication. I carried out the fabrication and performed the experiments, several together with PJ. I wrote the main part of the paper.
- III I developed and carried out the sensor fabrication, designed the computer program, performed the experiments, analyzed the results and wrote the main part of the paper.
- IV I helped with some of the experimental work and took part in the discussion of the results and in the preparation of the manuscript.
- V I supervised FM throughout the project, which was funded by a scholarship that I had obtained. I took part in some of the experimental work, analyzed the data together with FM and wrote the main part of the paper.

# Contents

<b>Abstract .....</b>	<b>iii</b>
<b>Appended papers .....</b>	<b>vi</b>
<b>Related work.....</b>	<b>vii</b>
<b>Reviews, book chapters and patents .....</b>	<b>viii</b>
<b>My contribution to the appended papers .....</b>	<b>ix</b>
<b>Contents.....</b>	<b>x</b>
<b>Abbreviations and acronyms .....</b>	<b>xii</b>
<b>Introduction to the thesis.....</b>	<b>1</b>
<b>Chapter 1 Bioanalytical sensing.....</b>	<b>3</b>
1.1 Biosensor applications .....	3
1.2 Basic principles of biosensing .....	4
1.3 Transduction mechanisms .....	5
1.3.1 Label-free sensors.....	6
1.3.2 Nanobiosensors.....	7
1.4 Specificity and selectivity.....	7
1.5 Biomolecular binding reactions .....	10
1.5.1 Surface coverage at equilibrium .....	10
1.5.2 Reaction limited binding .....	12
1.5.3 Mass transport limitations .....	13
1.6 Summary.....	18
<b>Chapter 2 Lipid membranes.....</b>	<b>19</b>
2.1 The cell membrane .....	19
2.2 Supported cell membrane mimics .....	21
2.2.1 Lipid vesicles .....	21
2.2.2 The supported lipid bilayer (SLB) .....	22
<b>Chapter 3 Plasmonics – basics and sensing .....</b>	<b>25</b>
3.1 Short introduction to the optics of metals .....	25
3.2 Surface plasmon polaritons .....	27
3.2.1 Surface plasmon resonance sensing .....	31
3.3 Localized surface plasmons .....	32
3.3.1 Localized surface plasmons resonance sensing.....	34
3.3.2 LSPR versus SPR sensing.....	36
3.3.3 Performance of LSPR sensors .....	37

<b>Chapter 4 Plasmonic nanoholes .....</b>	<b>39</b>
4.1 Spherical metallic voids .....	39
4.2 Single nanoholes in thin metal films.....	40
4.3 Periodic arrays of nanoholes in metal films .....	41
4.4 Short-range ordered nanoholes in thin metal films.....	42
4.5 Effect of film thickness .....	43
4.6 Effect of hole shape.....	44
4.7 Comparing particles and holes.....	44
<b>Chapter 5 Experimental procedures and methods.....</b>	<b>47</b>
5.1 Fabrication of nanoplasmonic structures.....	47
5.1.1 Sparse colloidal lithography .....	49
5.1.2 Hole-mask colloidal lithography .....	50
5.1.3 Nanosphere lithography .....	51
5.2 Extinction spectroscopy.....	52
5.2.1 Extinction measurements on large areas.....	53
5.2.2 Extinction spectroscopy on small areas .....	54
5.2.3 Data analysis – The centroid method.....	54
5.3 The quartz crystal microbalance.....	56
5.3.1 Theoretical description of the QCM.....	57
<b>Chapter 6 Results and discussion .....</b>	<b>59</b>
6.1 Nanoplasmonic structural sensing – Papers I and II .....	59
6.2 Combined nanoplasmonic and QCM-D sensing – Paper II.....	62
6.3 Flow-through nanoplasmonic sensing – Paper III.....	64
6.4 Improving performance by directed binding – Paper IV.....	66
6.5 Nanoplasmonic sensing with on-chip detection – Paper V .....	68
<b>Chapter 7 Conclusions, reflections and outlook.....</b>	<b>71</b>
<b>Acknowledgements .....</b>	<b>75</b>
<b>Populärvetenskaplig sammanfattning.....</b>	<b>77</b>
<b>References .....</b>	<b>79</b>

## Abbreviations and acronyms

Abs	absorption units
Au	gold
CCD	charged coupled device
CL	colloidal lithography
EBL	electron beam lithography
FIB	focused ion beam
FRAP	fluorescence recovery after photobleaching
FWHM	full width at half maximum
GLAD	glancing angle deposition
HCL	hole-mask colloidal lithography
HP	hole plasmon
HPR	hole plasmon resonance
LED	light emitting diode
LSP	localized surface plasmon
LSPR	localized surface plasmon resonance
NSL	nanosphere lithography
PDA	photo diode array
PEG	polyethylene glycol
PLL	poly-L-lysine
QCM	quartz crystal microbalance
QCM-D	quartz crystal microbalance with dissipation monitoring
RI	refractive index
RIE	reactive ion etching
RIU	refractive index units
SCL	sparse colloidal lithography
SEIRA	surface-enhanced infrared absorption
SEM	scanning electron microscopy
SERS	surface-enhanced Raman spectroscopy
Si	silicon
SiN	silicon nitride
SiO <sub>x</sub>	silicon oxide
SiO <sub>2</sub>	silicon dioxide
SLB	supported lipid bilayer
SPP	surface plasmon polariton
SPR	surface plasmon resonance
TiO <sub>2</sub>	titanium dioxide

## **Introduction to the thesis**

The work presented in this thesis is based on nanoplasmonic bioanalytical sensing. Nanoplasmonic sensors are based on the fascinating optical properties of nanoscale metal structures, perhaps most known for creating beautiful colours in stained glass. A nanoplasmonic sensor is a good example of a nanosensor, not only due to the small size of each sensing element, but also because the concept utilizes phenomena that are unique to nanostructured metals and not provided by the equivalent macroscopic size systems.

In this work, limitations of conventional biosensors and challenges in the field of biosensing have been addressed by (i) exploring opportunities offered by nanosensors in general, (ii) investigating properties specific to nanoplasmonic sensors and (iii) utilizing concepts that are unique to certain nanoplasmonic sensors, with focus on nanoplasmonic holes. Particular efforts have been put into developing nanoplasmonic sensors for the investigation of reactions related to mimics of natural cell membranes. With around half of the most common medical drugs targeting cell membrane associated reactions, such sensor systems may not only serve as important tools in basic research, but could also have direct implications in drug development and for improved medical diagnostics.

The thesis is divided into 7 chapters. The first provides an introduction to bioanalytical sensing by presenting common sensor applications, existing technologies and general challenges. The natural cell membrane and artificial lipid bilayer membranes are presented in Chapter 2. Chapter 3 serves as an introduction to the field of plasmonics. It presents the surface plasmon polariton (SPP) and the localized surface plasmon (LSP) and how these concepts can be used for sensing applications. Chapter 4 is dedicated to plasmonic holes, the type of structure that was explored the most in this thesis. It describes the optical properties of different plasmonic hole structures, with focus on their capabilities for bioanalytical sensing. The chapter ends with a comparison between nanoplasmonic holes and particles. Nanofabrication methods, experimental setups and data analysis are presented in Chapter 5. This chapter also describes the quartz crystal microbalance with dissipation monitoring (QCM-D), a complementary sensing method that was used in this work. The main results from the appended papers are presented in Chapter 6. Finally, conclusions are presented in Chapter 7, together with a discussion on new directions and possible extensions of this work.



# **Chapter 1      Bioanalytical sensing**

This chapter serves as an introduction to bioanalytical sensing, including why there is a need for better and new types of biosensors. Basic principles are presented, important applications discussed as well as challenges and unique possibilities that nanobiosensors may offer.

## **1.1      Biosensor applications**

The concept of sensors includes all devices that are used to monitor and provide information on a physical quantity. Sensors are therefore a natural part of our everyday life in the form of thermometers (temperature sensors), microphones (sound sensors) and cameras (light sensors). The list could easily be made longer. For example, around 100 different sensors can be found in the modern car.

Bioanalytical sensors or biosensors form a sub-group of sensors that are used to monitor and provide information on biological processes, such as biomolecular interactions. Interactions between biomolecules (protein-protein, protein-ligand, etc.) are essential for all living organisms as they control processes ranging from signaling between cells to enzymatic activities. This makes biosensors indispensable research tools in the quest to gain a better understanding of fundamental biological mechanisms.

Biosensors can be used to measure the concentration of a substance in a complex mixture. In turn, increased or lowered levels of specific biomolecules (biomarkers) characterize many diseases, which manifests an important role of biosensors in medical diagnostics. Biosensors are widely used in hospitals today and efforts are put into developing diagnostic instruments for rapid testing at point-of-care, which for instance may enable inexpensive diagnostics in the developing world. There are only a few commercially available point-of-care biosensors today, including pregnancy tests and blood glucose sensors. In addition to a general need for such biosensors, their success is primarily due to relatively simple instrumentation and low cost. The simplicity of biosensors has been explored in this work and will be discussed in more detail below.

Biosensors are also essential tools in the medical drug industry, for example, in the investigation of interactions between potential drugs and drug targets. The fact that many drug targets are associated with cell membranes makes it particularly relevant to develop sensors that enable the investigation of cell membrane related interactions. The development of such sensors was one of the main aims of this work. Other industrial applications of biosensors include

---

food analysis (detection of contaminants, vitamin levels, etc.) and environmental monitoring, such as the detection of pesticides in water.

An early example of a biosensor is the glucose sensor developed by Clark et al. in 1962.<sup>1</sup> However, the very first example of biosensing is considered to be the detection of toxic gases in coalmines. Interestingly, the sensor in this case was a bird. Each coal miner brought a couple of canary birds down into the mine and, because these birds are more sensitive to toxic gases than humans are, signs of distress (or worse) could be interpreted as toxic gas being present and time for evacuation.

## 1.2 Basic principles of biosensing

Regardless of how or what a sensor measures, it should provide some kind of *signal* or *response* to the user. Further, although “yes or no” answers may be sufficient for certain applications (e.g. “yes, you are pregnant!”), it is often preferable if the signal can also provide information on the magnitude of the variable measured (e.g. information on how far you are in your pregnancy). The concentration of an analyte in a suspension will be used as the variable in this discussion on biosensing. Different concentrations will then induce different sensor responses (at equilibrium), forming a concentration-response curve (see Fig. 1.1a). This curve is not necessarily linear and the response typically saturates at some upper value of the concentration. The saturation could be due to limitations of the sensor itself (e.g. saturation of a detector) or because of the interaction investigated (e.g. approaching full coverage for a surface-based sensor). The response typically decreases with decreasing concentration and at some point the signal is comparable to the *noise* in the system or the precision with which changes in the sensor signal can be measured (see also Fig. 1.1b).<sup>\*</sup> This sets the limit of detection in terms of the lowest detectable concentration. The dynamic range of the sensor system is then the range between the lowest detectable concentration and the upper value at which an increase in the concentration does not increase the equilibrium sensor response. As mentioned above and discussed in more detail below, the lower and upper limits are typically not only dependent on the properties of the sensor, but also related to the reaction under investigation, such as the affinity between an analyte-receptor pair.

Real-time sensing offers many advantages over end-point measurements. As illustrated schematically in Fig. 1.1b, real-time measurements can, for example, reveal whether two reactions with the same end responses have different pathways. In the illustration, curve 1 increases monotonically until equilibrium, while curve 2 follows a more complicated pathway. Similarly, real-time sensing can also help improve the dynamic range of a sensor system. This can be

---

<sup>\*</sup> Note that most sensors are based on the monitoring of *changes* in some parameter. The absolute values of the sensor parameter are often less important.

explained by the fact that although two different concentrations above the upper limit of the dynamic range will induce similar sensor signals at equilibrium, they may provide different kinetics and can therefore be distinguished.

The signal induced by the reactions and the noise in the system are indicated in Fig. 1.1b, where the noise corresponds to temporal fluctuations in the sensor parameter that are not due to the reactions under investigation. For clear detection, the signal should be significantly larger than the noise level. The noise level, in turn, is typically related to the acquisition rate and can often be decreased by increasing the acquisition time (or by averaging over a number of data points). Hence, it is often more challenging to accurately monitor the kinetics of a fast reaction compared with a reaction that is slower. On the other hand, very slow reactions can be difficult to monitor accurately because of long-term drifts in the sensor system. The drift could have many origins, from mechanical instability or changes in room temperature to pressure changes in a liquid flow cell etc.

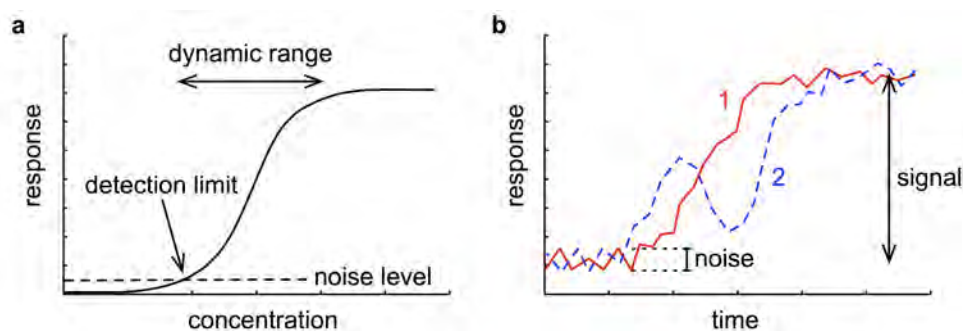


**Figure 1.1.** Schematic examples of (a) a concentration-response curve (equilibrium response) and (b) real-time sensing.

### 1.3 Transduction mechanisms

The sensor signal, or the response can be the intensity of a fluorescence signal, as widely used in DNA arrays and ELISA assays (enzyme-linked immunosorbent assay).<sup>2, 3</sup> Fluorescence-based techniques have proven to be important tools in many fields of research, not only for sensing, but also in, for example, various variants of imaging,<sup>4</sup> including single-molecule detection in living cells<sup>4, 5</sup> and in diffusion measurements using fluorescence recovery after photobleaching (FRAP)<sup>6-9</sup> or fluorescence correlation spectroscopy<sup>10, 11</sup> (see ref 4 for a review of fluorescence-based methods). However, biological reactions in general rely on the detailed three-dimensional structure of the biomolecules and may be affected by the addition of fluorescent markers or other kinds of labels. Furthermore, labeling can be time-consuming and for a mixture of many types of biomolecules it may not even be feasible to label the actual molecule of interest. Therefore, there has been a drive for sensor techniques that sense the target molecule without requiring external labels.

### 1.3.1 Label-free sensors

Sensor techniques that do not require labeling are typically surface-based and transduce biomolecular binding reactions in the vicinity to a surface via corresponding changes in the electrical, mechanical or optical properties of the system. Electrical or electrochemical sensor methods typically measure changes in electrical current, potential or conductivity between electrodes.<sup>12</sup> An example of a sensor with mechanical transduction is the quartz crystal microbalance with dissipation monitoring (QCM-D, see Chapter 5 for details).<sup>13</sup> The QCM-D is based on a piezoelectric quartz crystal, whose mechanical resonance frequency (and damping) changes upon adsorption of mass. The probably most commonly used label-free sensor is the optical surface plasmon resonance (SPR) method,<sup>14</sup> which detects changes in the refractive index (RI) close to the sensor surface, as induced by, for example, biomolecular binding. The SPR technique is based on surface plasmon polariton waves that are optically excited at a metal/dielectric interface, as described in detail in Chapter 3. Other optical techniques that rely on changes in interfacial RI include ellipsometry,<sup>15</sup> dual polarization interferometry,<sup>16</sup> optical waveguide lightmode spectroscopy<sup>17</sup> and optical microcavities.<sup>18</sup> The latter concept was recently found to provide a sensitivity that enables single biomolecular binding events to be monitored in a label-free format. Another interesting optical sensor method is back-scattering interferometry.<sup>19</sup> It can be used to investigate molecular interactions in free solution as opposed to binding to a surface. Electrical, mechanical and optical label-free sensors are all commercially available, for example from the Swedish companies Q-Sense AB (QCM-D), Layerlab AB (impedance-based) and Biacore AB (SPR, now GE Healthcare Biosciences AB). Three sensor systems used in our group are shown in Fig. 1.2.



**Figure 1.2.** Three examples of commercially available biosensors (images taken in our laboratories). The left image shows an E4 system from Q-Sense. The middle image shows the z-LAB One system from Layerlab and the right a Biacore 2000 from GE Healthcare Biosciences.

### 1.3.2 Nanobiosensors

Sensors that are based on nanoscale structures and/or nanoscale phenomena have great potential for challenging existing sensor technologies. Apart from competitive performance, many nanobiosensor methods, including the concept explored in this work, may allow for the development of small, simple and cheap devices, for example, to be used as point-of-care diagnostic instruments. This promise stems partly from the fact that the instrumentation can be simplified compared to many of the conventional techniques (explored in Paper V) and also that simple and cheap nanofabrication methods are available that allow for the production of a wide range of different nanostructures over large areas (see Chapter 5).

In addition, specific nanosensors often provide unique possibilities that can be used to address problems and limitations associated with conventional sensors. For example, in this work we show that nanoscale sensors can be used to improve transport of analytes to the sensor surface (Papers III and IV, discussed in detail below). Further, the mere fact that nanosensors are small is promising with respect to the development of miniaturized and dense array-based sensor devices.<sup>20,21</sup>

Examples of label-free nanobiosensors include silicon nanowires, whose electrical properties can be used to monitor biomolecular binding events in real-time.<sup>21, 22</sup> Mechanical alternatives include micro- and nanocantilevers,<sup>23-26</sup> for which either deflection or changes in the mechanical resonance frequency can be used to study binding reactions. Note that the mechanical oscillation of a cantilever is typically heavily damped when operated in a fluid. This was recently addressed by instead placing the sample solution inside the cantilever using suspended micro- and nanochannels.<sup>27-29</sup> There are also nanosensors with optical transduction. Those based on nanoplasmonics (the peculiar optical properties of metal nanostructures) are particularly promising and have received increased attention the last ten years.<sup>30-32</sup> Most of the work presented in this thesis is based on nanoplasmonics, which will be described in detail in Chapters 3 and 4.

## 1.4 Specificity and selectivity

An interesting feature of label-free sensors is that, although they can detect the binding of molecules, they are typically blind to the type of molecules that bind to the sensor surface. For example, many optical techniques, including those developed in this work, are based on detecting changes in RI close to the sensor surface. In turn, a change in RI can be due to binding of in principle any type of biomolecule. It is therefore highly important to control the surface chemistry in such a way that only the interactions of interest occur on the surface. This is indeed a challenge, but at the same time it makes these sensors versatile in the sense that the surface chemistry can be modified for the application of interest.

---

To be able to measure the concentration of, for example, a specific type of biomolecule in a blood sample, the surface chemistry should be selective. This means that it should promote binding of the biomolecule of interest while adsorption of all other molecules should be minimized (see Fig. 1.3). This is particularly challenging considering that typical biomarkers and other biomolecules of interest are often present in low concentrations (nanomolar or lower), while the concentration of many other molecules, whose adsorption needs to be suppressed, is many orders of magnitude higher.

Polyethylene glycol (PEG) is known to be inert to biomolecular binding.<sup>33</sup> A sufficiently dense layer of PEG on the sensor surface can therefore be used to efficiently suppress unspecific binding of biomolecules. On gold, PEG can be bound by having one end modified with a thiol group (thiolPEG). On materials like glass, silicon dioxide ( $\text{SiO}_2$ ), silicon nitride ( $\text{SiN}^*$ ) and titanium dioxide ( $\text{TiO}_2$ ) it is useful to use PEG that is grafted to poly-L-lysine (PLL-*g*-PEG).<sup>33</sup> After preventing all non-interesting biomolecules from binding to the sensor surface, the task remains to promote binding of the biomolecule of interest. This is typically addressed by the attachment of a receptor moiety to one end of the PEG molecule, to which the analyte can bind specifically. Strategies other than the use of PEG to reduce unspecific biomolecular adsorption include, for example, the use of milk powder or bovine serum albumin, where the latter enables the addition of receptor groups in a similar manner to PEG.<sup>26, 34, 35</sup>

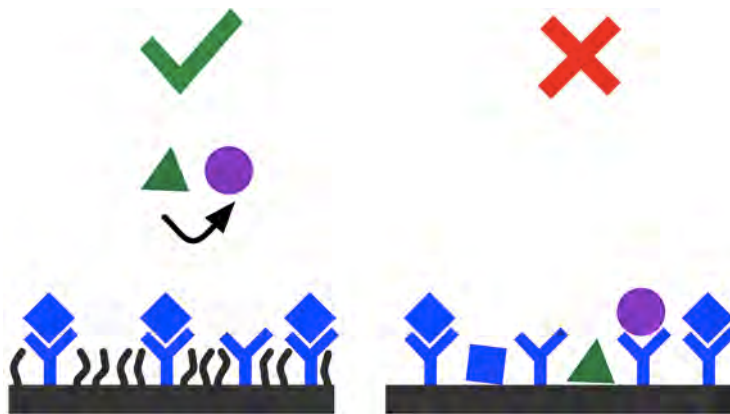


**Figure 1.3.** The illustration on the left shows the preferable situation of both specific and selective binding, while the illustration on the right includes unspecific adsorption of both the analyte and other molecules.

---

\* Note that the stoichiometric form of silicon nitride is  $\text{Si}_3\text{N}_4$ , but not necessarily the form used in experiments, which is why the term SiN is used here.

**Materials-specific surface chemistry.** It is useful if the analyte can be controlled to only bind on the sensitive part of the sensor. One reason is to make sure not to lose precious analyte molecules that otherwise would also bind on regions that do not result in a sensor response. In addition, for nanoscale sensors in particular, directed binding to high-sensitivity areas can help to improve sensor performance. This was explored in Paper IV and is discussed in Chapter 6. For sensors that consist of more than one material, directed binding can be achieved using materials-specific surface modifications. A sensor surface with gold and SiO<sub>2</sub> regions will here be used as an example.

While thiolPEG binds on gold, it does not bind on SiO<sub>2</sub> (or SiN). It is thus possible to modify a gold surface with thiolPEG (with or without bioactive receptor molecules) while leaving neighboring SiO<sub>2</sub> areas unmodified and available for subsequent modifications. For example, PLL-g-PEG can be used in a second step. It will bind to the SiO<sub>2</sub>, but not to the passivated gold regions. In this way, the analyte can be controlled to bind preferentially on gold, SiO<sub>2</sub> or on both materials by having the thiolPEG, the PLL-g-PEG or both bioactive, respectively (see Fig. 1.4).

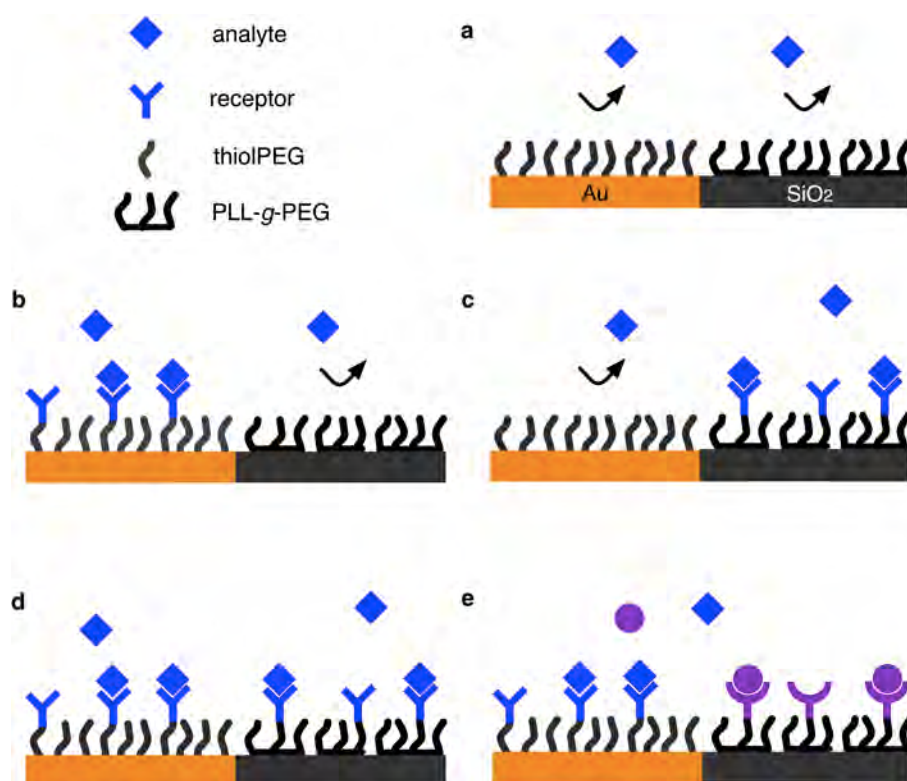


**Figure 1.4.** Schematic illustrations showing different possibilities offered by materials-specific surface chemistry. **(a)** Both surface are passivated. **(b)** Analyte binding is promoted on the Au surface, but suppressed in the SiO<sub>2</sub> region. **(c)** The opposite situation from (b). **(d)** Binding promoted on both surfaces. **(e)** Binding of different analytes is promoted on the two surfaces using an additional receptor.

---

## 1.5 Biomolecular binding reactions

The previous section presented strategies that enable controlled binding of specific biomolecules to sensor surfaces. In this section, the *surface coverage* of bound biomolecules (e.g. in terms of bound mass per area or number of bound molecules per area) will be discussed. The surface coverage is an essential parameter in biosensing. In fact, the sensor response of most label-free sensors, including the ones used in this work, is directly related to the surface coverage and not to the total bound mass or the total number of bound molecules.

The equilibrium situation will be treated first, followed by a discussion on the rate of binding (and the time it takes to reach equilibrium or a detectable coverage) and different limiting factors. In particular, the benefits of using micro and nanofluidics to decrease sensor response times are discussed, with the aim of showing that nanofluidic channels may be used to simultaneously improve the binding rate and sample volume consumption (explored in Paper III). An excellent and more extensive discussion on binding kinetics, mass transport phenomena and the use of fluidics can be found in a recent review by Squires et al.<sup>36</sup>

### 1.5.1 Surface coverage at equilibrium

Most biomolecular interactions are reversible. For a surface-based sensor this means that target analyte molecules will continuously bind and unbind to the receptor molecules on the sensor surface. The change in surface coverage  $\Gamma$  (i.e. the change in number of bound analyte molecules per unit area) with time  $t$  can be described by a first order differential equation:

$$\frac{d\Gamma(t)}{dt} = k_{\text{on}}c[\Gamma_{\text{max}} - \Gamma(t)] - k_{\text{off}}\Gamma(t) \quad (1.1)$$

The first and the second term in Eq. 1.1 represent binding and unbinding (with reaction coefficients  $k_{\text{on}}$  and  $k_{\text{off}}$ ), respectively. The available number of binding sites on the sensor surface represents full coverage,  $\Gamma_{\text{max}}$ , and  $c$  is the concentration of analyte in the solution above the sensor surface. Equilibrium is reached when the rates of binding and unbinding are equal and the relative surface coverage at equilibrium,  $\Gamma_{\text{eq}}/\Gamma_{\text{max}}$ , is then obtained as:

$$\frac{\Gamma_{\text{eq}}}{\Gamma_{\text{max}}} = \frac{1}{1 + \frac{k_{\text{off}}}{k_{\text{on}}c}} = \frac{1}{1 + \frac{K_{\text{D}}}{c}} \quad (1.2)$$

where  $K_{\text{D}}$  is the equilibrium dissociation constant. The inverse of  $K_{\text{D}}$  represents the affinity and thus the strength of the interaction. As shown in Fig. 1.5, the equilibrium surface coverage at different concentrations follows a sigmoidal curve. Two curves with different dissociation constants are shown in the figure.

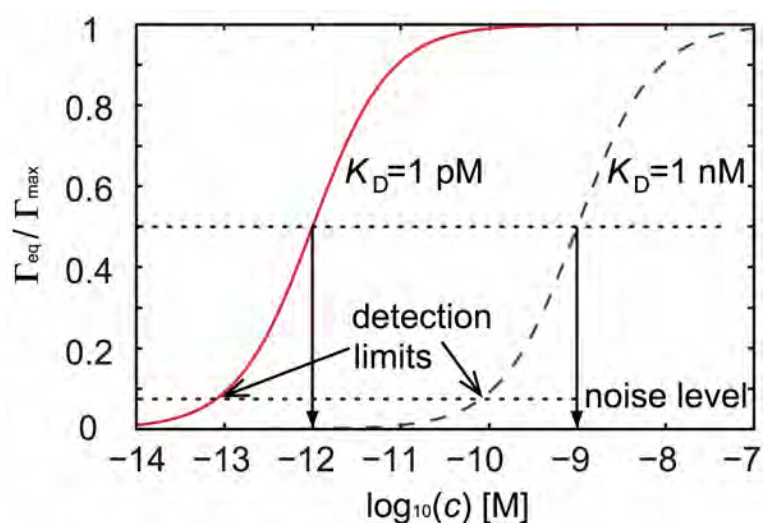


**Figure 1.5.** Relative equilibrium coverage according to Eq. 1.2 ( $\Gamma_{\text{eq}}/\Gamma_{\text{max}}=1$  represents full coverage) with respect to concentration for two interactions with different dissociation constants. The solid curve shows the situation for a strong interaction, such as avidin binding to biotin receptors on a surface. The dashed curve represents a weaker interaction (e.g. antigen-antibody binding).

The solid curve represents a strong biomolecular interaction, such as that between NeutrAvidin (avidin analogue) and biotin receptors immobilized on a sensor surface ( $K_D \sim 1$  pM).<sup>37\*</sup> The dashed curve instead shows the situation for a weaker binding, such as an antigen antibody pair ( $K_D \sim 1$  nM).<sup>34, 38</sup> For an irreversible reaction ( $k_{\text{off}}=0$  and  $K_D=0$ ) we have that  $\Gamma_{\text{eq}}=\Gamma_{\text{max}}$  for all concentrations. The dissociation constant of an interaction corresponds to the concentration at which  $\Gamma_{\text{eq}}/\Gamma_{\text{max}}=0.5$ . Hence, it can be determined from the concentration-response curve under the assumption that the response is either linearly dependent on the surface coverage or that the relation between response and surface coverage is known. The concentration-response curve can, in turn, be obtained experimentally by measuring the equilibrium sensor response at different concentrations. A hypothetical noise level (at around 8% coverage, much higher than for a typical biosensor) of the system was drawn in Fig. 1.5 to emphasize that the detection limit in terms of bulk concentration (with respect to the response at equilibrium) is highly dependent on the strength of the interaction. The reason is simply the difference in equilibrium surface coverage that is reached at the same concentration for reactions with different affinities. Note also that in order for the reduction in bulk concentration upon binding to be negligible, a sufficient amount of material is required in the bulk suspension. For picomolar concentrations of a 60 kDa protein like NeutrAvidin and a sensor with a detection limit of around

\* While values reported for surface-based binding were chosen for the examples used here, it is worth to note that the affinity between avidin and biotin is even stronger in solution ( $K_D \sim 1$  fM).<sup>37</sup>

0.1 ng/cm<sup>2</sup> (corresponding to  $\approx 17$  pmol/m<sup>2</sup>) and a sensor area of 100×100 μm<sup>2</sup>, the minimum sample volume needed is in the order of microliters in order for the concentration not to drop more than around 10% upon binding.

### 1.5.2 Reaction limited binding

From the curves in Fig. 1.5 one might get the impression that it is straightforward to detect, for example, picomolar concentrations when the interaction is strong, while it seems very challenging when the interaction is weak. While the latter is indeed the case, it is in fact often challenging to detect low concentrations also for strong interactions. The discussion above was based on the sensor response that is induced at equilibrium binding conditions and it may not necessarily be feasible to reach equilibrium conditions within a reasonable time scale. The binding kinetics for reaction controlled binding is described by Eq. 1.1 with solutions (using boundary conditions  $\Gamma(0) = 0$  and  $\Gamma(\infty) = \Gamma_{\text{eq}}$  that take an exponential form (often termed the Langmuir isotherm):<sup>37</sup>

$$\frac{\Gamma(t)}{\Gamma_{\text{max}}} = \frac{1}{1 + \frac{K_D}{c}} \left[ 1 - e^{-(k_{\text{on}}c + k_{\text{off}})t} \right] \quad (1.3)$$

From Eq 1.2 it is clear that for a specific concentration, two interactions with the same affinity (and hence the same dissociation constant,  $K_D = k_{\text{off}}/k_{\text{on}}$ ) will have the same equilibrium coverage. However, the rate of the reaction, as determined by the exponential term in Eq. 1.3, is dependent on both  $k_{\text{on}}$  and  $k_{\text{off}}$  and not only on their ratio. This means that for a specific concentration, two interactions with the same affinity, but different  $k_{\text{on}}$  and  $k_{\text{off}}$ , will display different binding kinetics. The time to reach a certain fraction  $x$  of the equilibrium surface coverage is obtained as:

$$t = \frac{-\ln(1-x)}{k_{\text{on}}c + k_{\text{off}}} \quad (1.4)$$

To reach half the equilibrium coverage for picomolar concentrations of NeutrAvidin (binding to biotin on a surface,  $k_{\text{on}} \sim 10^8 \text{ M}^{-1}\text{s}^{-1}$ ,  $k_{\text{off}} \sim 10^{-4} \text{ s}^{-1}$ )<sup>37</sup> gives a time scale in the order of an hour. It would only take a few seconds to reach a detectable surface coverage assuming a detection limit of 0.1 ng/cm<sup>2</sup> for state of the art sensors and a full surface coverage of around 230 ng/cm<sup>2</sup>.<sup>39</sup> However, these time scales only consider limitations set by the interaction itself (reaction limited binding). In the following section it will be explained that transport of molecules to the sensor surface is often the main limitation, which therefore makes the biomolecular uptake slower than what is predicted by Eqs. 1.3 and 1.4.

### 1.5.3 Mass transport limitations

In the discussion above it was assumed that the concentration in close proximity to the sensor surface is equal to the bulk concentration and constant with time. However, upon binding, the region close to the sensor surface becomes depleted of biomolecules, which reduces the local concentration. Subsequent binding then relies on transport of more molecules to the sensor surface. In particular for low concentrations of slowly diffusing analyte molecules, the uptake kinetics can therefore deviate significantly from that described by Eq. 1.3. Instead, the rate of binding is often limited by the transport of molecules to the sensor surface.

**Diffusion limited binding.** Under stagnant conditions, as commonly used in sensor applications, molecules move around by diffusion only. Assuming that all molecules that reach the sensor surface bind instantaneously, the concentration is zero at the surface and increases with the distance from the surface until it reaches that of the bulk solution. Diffusion limited binding to a planar sensor surface can then be described by:<sup>40</sup>

$$\Gamma(t) = 2c\sqrt{\frac{Dt}{\pi}} \quad (1.5)$$

where  $D$  is the diffusion coefficient of the analyte molecules in the sample. Equation 1.5 gives the total number of molecules that has reached the sensor surface per unit area after a certain time. For a 1 pM concentration of streptavidin or NeutrAvidin (molecular weight around 60 kDa) that binds to a biotinylated surface ( $K_D \sim 1$  pM), the equilibrium coverage is around 19 nmol/m<sup>2</sup> (115 ng/cm<sup>2</sup>, half of the maximum surface coverage).<sup>39</sup> With a diffusion coefficient of around  $6 \times 10^{-11}$  m<sup>2</sup>/s, it would take more than 100 000 years to reach this surface coverage. To reach a detection limit of around 0.1 ng/cm<sup>2</sup> it would still take more than a month, which is clearly many orders of magnitudes longer than the times predicted based on reaction limited binding. This illustrates that in this situation the mass transport must be significantly improved in order to reach reasonable response times.

According to the diffusion limited model (Eq. 1.5) the biomolecular uptake does not saturate with time. This is not physically possible for a system with a limited number of binding sites and suggests that, while the initial binding is often limited by mass transport, the uptake must convert to a reaction limited behavior at some stage as the equilibrium surface coverage is approached. At every point in time, the balance between molecules available for binding and the available binding sites, together with the reaction rates, determine the exact behavior of the binding (see Fig 1.6 for schematic illustrations where the two different limiting factors dominate).

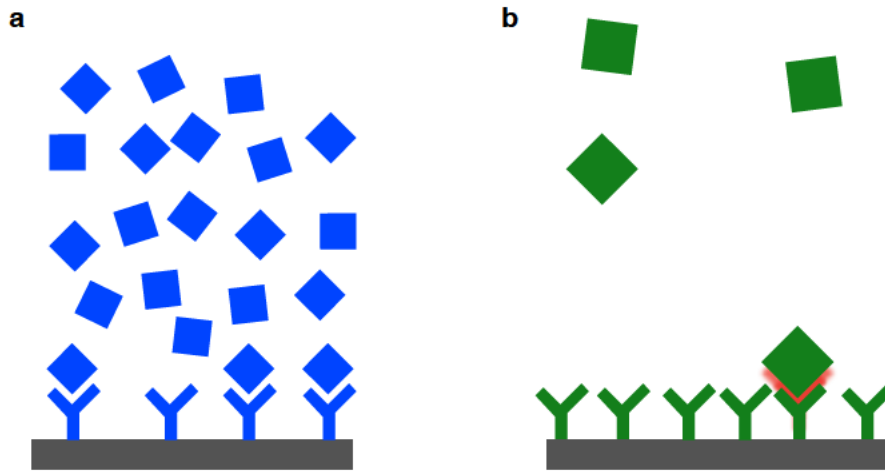


**Figure 1.6.** Schematic illustrations of typical conditions for reaction and mass transport limited binding. **(a)** A typical reaction limited situation: high concentration, small molecules that diffuse quickly and few available binding sites. The bound analyte molecules are drawn a distance from the receptors on purpose to give the impression that the binding is also weak. **(b)** A typical mass transport limited situation: there are only few molecules available for binding and they are also large and diffuse slowly. This is combined with a high surface density of available binding sites. The shaded area depicts a strong affinity between the bound analyte and the receptor.

**Fluidics for improving mass transport.** A discussion will now be presented on the role of fluidics in sensing applications. Note that most prefactors will be neglected in the derivations and the absolute values in this section are only rough estimates. Focus is instead on the orders of magnitudes and the scaling behaviors, which are valuable when comparing different systems and for understanding the influence of different parameters on the mass transport. Furthermore, it is assumed that all molecules that reach the surface bind instantaneously and remain bound.

For diffusive transport under stagnant conditions, the layer above the sensor surface that is being depleted from molecules during binding is continuously growing. The depletion length  $\delta$  scales as  $(Dt)^{1/2}$  and typically extends hundreds of micrometers already after a few minutes. Now assume that the sample solution is instead constantly flown over the sensor surface. In this way, transport of new molecules will compete with the growing depletion zone. The depletion zone will reach a steady state that can be estimated by comparing the time scale  $\tau_D$  for molecules to diffuse through the depletion zone to the surface ( $\tau_D \sim \delta^2/D$ ) and the time scale  $\tau_f$  for molecules at the same distance from the surface to flow a certain distance  $l$  over the sensor surface with a flow speed  $v$  ( $\tau_f = l/v(\delta)$ ). This gives:

$$\delta \sim \sqrt{\frac{Dl}{v(\delta)}} \quad (1.6)$$

For a pressure driven flow, the velocity profile within a microfluidic channel is parabolic with the highest speed in the middle and with no flow at the surfaces. Close to the sensor surface the velocity can be approximated as linearly dependent on the distance  $z$  from the surface:<sup>36</sup>

$$v(z) \approx \frac{6Q}{wh^2} z \quad (1.7)$$

where  $Q$  is the volumetric flow rate and  $w$  and  $h$  are the channel width and height, respectively. Inserting Eq. 1.7 into Eq. 1.6 with  $z=\delta$  gives the depletion length as:

$$\delta \sim \left( \frac{Dwh^2l}{Q} \right)^{1/3} \quad (1.8)$$

For a typical microfluidic channel of 100  $\mu\text{m}$  width and height, a flow rate of 10  $\mu\text{L}/\text{min}$  and  $D=6 \times 10^{-11} \text{ m}^2/\text{s}$  as before, Eq. 1.8 gives an estimated depletion length of less than 10  $\mu\text{m}$  for all positions within 1 mm from the start of the sensor surface (see Fig. 1.7a). In comparison, a depletion length of 10  $\mu\text{m}$  is obtained already after tens of milliseconds under stagnant conditions. One might therefore suspect also an improvement in the transport of molecules to the surface when this kind of flow is applied. The binding rate allowed by mass transport will be equal to the flux of molecules to the sensor surface (number of molecules reaching the surface per unit area and per unit time). Further, because the transport rate at steady state is constant with time, the surface coverage is obtained by simply multiplying the binding rate by  $t$ .<sup>\*</sup> By estimating the concentration gradient as the difference in concentration from that of the bulk to zero over the depletion length ( $-c/\delta$ ), the uptake can be described by:

$$\Gamma(t) = -Dt\nabla c \approx \frac{Dc}{\delta} t \sim cD^{2/3} \left( \frac{Q}{wh^2l} \right)^{1/3} t \quad (1.9)$$

This gives the uptake at different positions along the sensor and the average uptake over a sensor with length  $L$  is then:

$$\Gamma_{\text{average}}(t) = \frac{1}{L} \int_0^L \Gamma(t) dl \sim cD^{2/3} \left( \frac{Q}{wh^2L} \right)^{1/3} t \quad (1.10)$$

---

<sup>\*</sup> The time to reach steady state is neglected. Also note that the expression is not valid for slow flows or when the depletion length becomes comparable to the channel dimensions. This is, for example, clear from the fact that Eq. 1.9 suggests that  $\Gamma(t)=0$  for all  $t$  when  $Q=0$ .

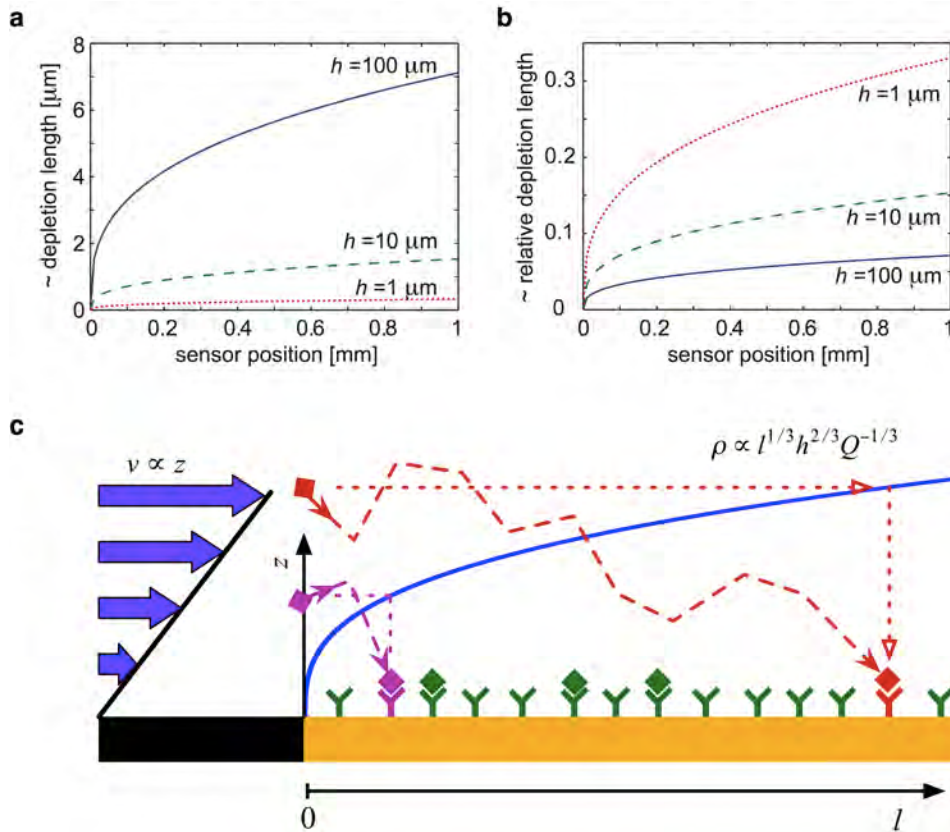


**Figure 1.7.** (a) Estimations of the depletion zone at steady state along a sensor for three different channel heights and with  $Q=10 \mu\text{L}/\text{min}$ ,  $D=6 \times 10^{-11} \text{m}^2/\text{s}$  and  $w=100 \mu\text{m}$ . (b) Identical to (a), but showing the depletion lengths relative to the channel height. (c) This schematic illustration is intended to illustrate the meaning of the depletion zone. A molecule entering ( $l=0$ ) at a height  $z'$  will on average reach the sensor surface at a position  $l'$  at which the depletion length is  $z'$ .

Using the same figures as above and with a  $100 \mu\text{m}$  long sensor, a detectable coverage ( $0.1 \text{ng}/\text{cm}^2$ ) at picomolar concentrations is obtained after around 10 min. This is much faster than under stagnant conditions (as previously mentioned, it would take around a month), yet still far from the reaction limit conditions, which gave values in the order of seconds. Hence, there is room for further improvement. Note also that 10 min at  $10 \mu\text{L}/\text{min}$  indicates that the sample volume needed for detection in this situation is in the order of  $100 \mu\text{L}$ . By comparing this value with the volume that contains the number of molecules needed on the surface for detection ( $<1 \mu\text{L}$ ) it is clear that only a small fraction of all molecules that flow past the sensor will actually be detected in this situation. This is discussed further below.

For a given sample solution (fixed  $c$  and  $D$ ) the parameters one can play with are those in the parentheses in Eq. 1.10. However, the  $1/3$ -exponent renders most changes rather undramatic. For example, an increase in the volumetric

flow rate by a factor 10 only doubles the binding rate.\* However, it does help somewhat to decrease the channel height. For a fixed volumetric flow rate (fixed  $Q$ ) a decrease in the channel height from 100  $\mu\text{m}$  to 10  $\mu\text{m}$ , increases the binding rate around 5 times. This is a first indication that a shift from micro- to nanofluidics could be useful for these types of applications. However, it may not be possible to use the same volumetric flow rate when decreasing the channel height. It is therefore important to note that the binding rate will increase with decreasing channel height also when the average flow speed in the channel,  $v_0$ , is kept fixed ( $v_0=Q/wh$ , giving  $d\Gamma/dt \propto h^{-1/3}$ ). This means that both the sensor response time and the sample consumption can be improved simultaneously by scaling down the fluidics. It should be noted that, due to rapidly increasing flow resistance with decreasing channel height, it may be challenging also to keep the flow speed fixed. This potential problem may be addressed, for example, by decreasing also the channel length. A concept for nanoscale fluidics combined with sensing that takes these aspects into account was reported in Paper III and is discussed in greater detail in Chapter 6.

Finally, for situations where the total number of molecules is limited, the capture efficiency may be a relevant parameter. The capture efficiency is here defined as the fraction of all molecules in the convective flow that reach the sensor surface and bind. As indicated in the example above, only a few percent or less of all molecules flowing past the sensor will actually arrive at the surface for a typical microfluidic system. The rest will end up as waste. Interestingly, even though the depletion length decreases with decreasing channel height (Eq. 1.10), the depletion length relative to the height of the channel exhibits the opposite behavior ( $\delta/h \propto h^{-1/3}$  for fixed  $Q$  [see Fig. 1.7b],  $\delta/h \propto h^{-2/3}$  for fixed  $v_0$ ). A comparison between the flux to the surface and the total flux through the channel reveals that decreasing the channel height can be employed to improve the capture efficiency. Even though the discussion here is under the assumption that  $\delta \ll h$  and hence not valid when  $\delta$  becomes comparable to  $h$ , one can imagine situations where the channel dimensions and depletion lengths coincide and that essentially all molecules will be captured (until reaction limitations sets in).

---

\* This works also the other way around, which can be used to decrease the sample volume consumption. A decrease in  $Q$  by a factor 10 only decreases the binding rate by around a factor 2.

---

**Other ways of improving mass transport.** Many nanosensor concepts have in common that small nanoscale regions are sensitive to binding (e.g. nanowires,<sup>21</sup> nanocantilevers<sup>23</sup> or nanoparticles<sup>41</sup>), while binding to areas that surround these regions does not result in a sensor response. This gives a unique possibility to improve the response time for purely diffusive binding, as shown in Paper IV and discussed in Chapter 6. In brief, the concept is based on selective binding of the analyte to high-sensitivity regions only. While the total number of bound molecules at a given time will be the same whether molecules bind on sensitive nanoscale regions or everywhere, the local surface coverage on the sensitive regions will be higher in the first case. This concept may be particularly valuable in situations where the sample volume is limited. Another interesting possibility is to attract biomolecules to the surface or preconcentrate them, for example, using electrokinetic effects.<sup>42, 43</sup> These principles are fundamentally different from the ones discussed above, because the local concentration next to the surface is increased and can even exceed that of the bulk solution. Hence, such systems may improve the detection limit in terms of lowest bulk concentration also for reaction limited situations.

## 1.6 Summary

The most important points of this chapter on bioanalytical sensing are, first of all, that biosensors have direct and important applications and that there is significant room for improvement. Focus of the chapter was put on some of the key concepts in biosensing:

- *Label-free sensing* – simple sample preparation, no interference with labels, generic sensors, etc.
- *Real-time sensing* – kinetic information, rapid detection, etc.
- *Simplicity* – point-of-care diagnostics, hand-held devices, etc.
- *Fluidics* – improvement of mass transport, rapid detection, etc.

Other important aspects of sensing, such as sensitivity maximization and noise minimization are discussed in Chapters 3 and 5 in connection with the type of sensors used in this work. Apart from addressing these general issues in bioanalytical sensing, this work has focused on specific applications and sensing compatible with artificial cell membranes in particular, as discussed in the next chapter.

## Chapter 2      **Lipid membranes**

Artificially made mimics of the cell membrane were investigated in Papers I and II and deserve some closer attention. After an introduction to the natural cell membrane and a discussion of the importance of being able to study reactions associated with cell membranes, artificial cell membrane mimics are introduced, with focus on lipid vesicles and supported lipid bilayers.

### **2.1      The cell membrane**

The core structural element of the cell membrane, also called the plasma membrane, is a 5 nm thick lipid bilayer shell that surrounds the living cell. It is a vital part of life as it makes it possible to maintain (and protect) molecules and functioning organelles (which themselves are surrounded by lipid bilayer membranes) inside confined compartments. The main constituents of the cell membrane are amphiphilic lipid molecules. While the hydrophilic head group of a lipid prefers to be exposed to water, its hydrophobic tails avoid such contact. In aqueous solution, the lipids therefore spontaneously self-assemble into a bilayer-like structure. The tails are shielded from the aqueous solution by pointing towards each other and the polar head groups are facing the two liquid environments inside and outside the cell, as depicted schematically in Fig. 2.1. The resulting lipid bilayer structure acts as a hydrophobic barrier, which limits the membrane permeability with respect to large, charged and polar molecules as well as atomic ions.

Still, the cell membrane can enable selective transport of molecules in and out of the cell, and it is also responsible for signaling between cells, adhesion of cells to surfaces and to other cells, etc. These important properties are mainly controlled by different kinds of proteins and protein complexes that are embedded in the cell membrane (signaling receptors, ion channels, aquaporins, etc.).<sup>44</sup> In fact, around 30% of the approximately 20,000-25,000 human genes<sup>45</sup> code for proteins that are embedded in the cell membrane or in other ways associated with membrane-related processes.<sup>46</sup> The restricted permeability ensured by the lipid bilayer combined with selective membrane transport makes it possible for cells to generate and sustain essential molecular gradients.

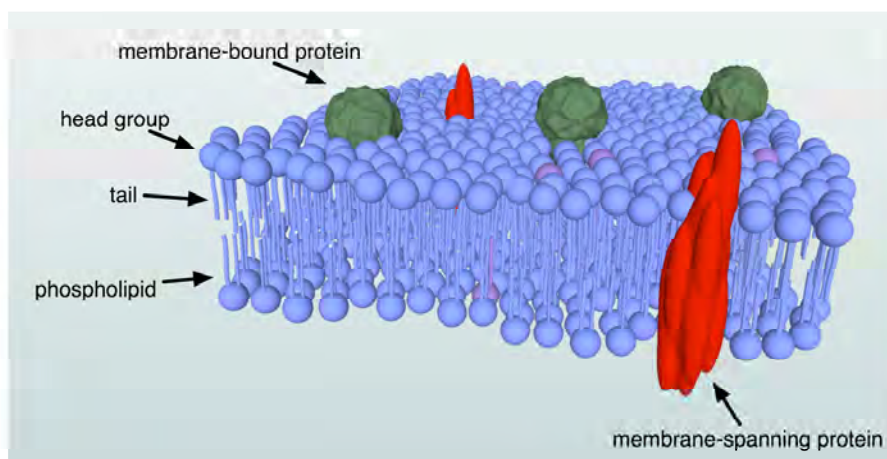


**Figure 2.1.** A simplified schematic illustration of the cell membrane.

It should be emphasized that the complexity of the cell membrane is not restricted to its composition. The cell membrane is constantly undergoing changes, both in shape and by lateral movement of membrane components within the lipid bilayer. The lateral fluidity is important as it makes the membrane self healing, but also because it allows embedded proteins to form complexes and lipids to organize into domains (often referred to as rafts).<sup>47</sup> Such organized structures, in turn, play essential functional roles in, for example, membrane-fusion processes as well as in the pathogenesis of various diseases.<sup>47-50</sup>

The important role of the cell membrane is manifested by the fact that around half of the most common drugs are directed towards membrane receptors.<sup>46</sup> However, despite their vital importance, the knowledge about the structure and function of membrane proteins is still very limited. This is, to a large extent, due to their low natural abundance and the difficulty to produce and purify them.<sup>51</sup> Furthermore, to preserve their function, membrane proteins should be maintained in a native-like environment, that is, in a lipid bilayer. Biosensors that are compatible with studies of lipid bilayer assemblies are therefore particularly suitable for functional investigations of membrane proteins, not only from a fundamental perspective, but also with respect to applications for medical diagnostics and drug development.

## 2.2 Supported cell membrane mimics

In order to study processes associated with the cell membrane in a controllable way, it is valuable to use model membranes that are less complex than the native cell membrane. The lipid vesicle and the supported lipid bilayer (SLB) are two artificial membrane concepts commonly used in combination with surface-based sensors and also the structures that were used in this work (Fig. 2.2).

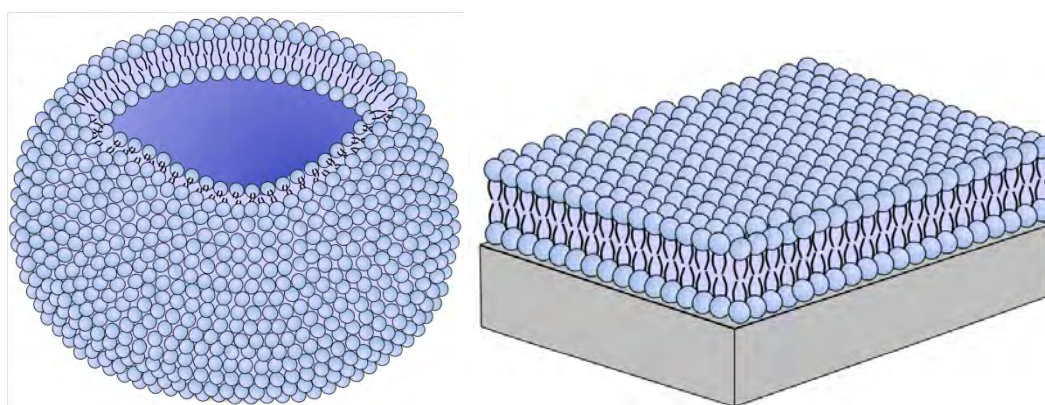


**Figure 2.2.** Schematic illustrations of a lipid vesicle (left) and a SLB on a surface (right).

### 2.2.1 Lipid vesicles

One popular artificial cell membrane mimic is the lipid vesicle, also known as liposome (see Fig. 2.2 left). It is a spherical lipid bilayer shell filled with aqueous solution. Depending on preparation method, lipid vesicles may have multiple shells (multilamellar vesicles) or single shells (unilamellar vesicles). In this work, unilamellar lipid vesicles were used. They were prepared by the extrusion method<sup>52, 53</sup> in which an essentially unordered lipid suspension is forced through a polymer membrane containing multiple nanopores. This results in lipid vesicles being formed in a process similar to that of blowing soap bubbles. The method enables the preparation of vesicles with different lipid compositions and with diameters ranging from tens to hundreds of nanometers.<sup>53</sup>

The possibility to tether lipid vesicles to a surface<sup>54</sup> is highly valuable for bioanalytical sensing applications, because the transduction mechanisms of many sensors are, as described above, based on biomolecule-induced optical, electrical or mechanical changes at or close to a sensor surface. One popular means of attaching vesicles to a surface is to prepare the vesicles with a small fraction of biotin-modified lipids. These vesicles can then be bound to a surface modified with avidin (or streptavidin or NeutrAvidin).<sup>55</sup> An increasingly popular approach is to use DNA as surface tethers. A lipid vesicle modified

---

with single-stranded DNA can be site-selectively bound to a surface modified with complimentary DNA strands.<sup>56, 57</sup> Because the hybridization process is highly specific, this strategy has the potential for multiplexed automatic sorting of vesicles, which may be of particular value for array-based membrane proteomics.<sup>58</sup> DNA tethers can be attached to lipid vesicles by, for example, covalently attaching DNA to lipids modified with reactive head groups.<sup>59</sup> One can also use cholesterol-tagged DNA, which spontaneously incorporates into lipid bilayers.<sup>60, 61</sup> In this case, the hydrophobic cholesterol part self-incorporate into the hydrophobic part of the lipid bilayer, making the concept highly attractive in combination with, for example, lipid vesicles derived directly from native cell membranes.<sup>62</sup>

### **2.2.2 The supported lipid bilayer (SLB)**

An alternative to immobilized lipid vesicles is the concept of supported lipid bilayers (SLBs).<sup>7, 63, 64</sup> A SLB is a planar lipid bilayer that rests on a support, which may be part of a surface-based sensor system (see Fig. 2.2 right). Silica-based supports (i.e. glass) are by far the most popular, mainly because of the simple SLB preparation procedure. On silica, mica and some metal oxides, such as titanium dioxide, SLBs can be formed spontaneously by adsorption and spontaneous rupture of lipid vesicles, without the need for pre-functionalization of the surface apart from normal cleaning procedures.<sup>65-67</sup> In contrast, under normal conditions, vesicles do not rupture on most other materials. These include metals (e.g. gold) that are commonly used in electrical, mechanical as well as optical surface based sensors.<sup>12, 14, 68, 69</sup> Instead, vesicles adsorb and remain non-ruptured on such surfaces. A simplified schematic illustration of the SLB formation process on silicon dioxide (SiO<sub>2</sub>) is presented in Fig. 2.3. The vesicles first adsorb and remain non-ruptured and after a critical surface coverage they rupture to form a SLB on the surface. Analogous to the lateral fluidity of a real cell membrane, the lipids in a SLB have a high lateral diffusivity, although somewhat reduced compared with that of lipid vesicles.<sup>70</sup> Similar to lipid vesicles, SLBs can be modified with different components, including membrane proteins.<sup>71</sup> Moreover, SLBs have been proven successful in studies of crystallization of water-soluble proteins,<sup>66, 72-75</sup> multivalent interactions<sup>76</sup> and cell adhesion,<sup>7</sup> to mention a few important examples.

By forming a SLB from vesicles that contain a small fraction of fluorescently labelled lipids (typically 0.1-1%), the final SLB also becomes fluorescent. Except from traditional fluorescence-based imaging, this enables the characterization of the lateral mobility in the artificial cell membrane using, for example, fluorescence recovery after photobleaching (FRAP).<sup>6, 9</sup> In FRAP, fluorescent molecules in a small region (typically around 10  $\mu\text{m}$  in diameter) of the microscope's field of view are photobleached. For a fluid SLB that is considerably larger than the bleached region, non-bleached lipids will diffuse into the bleached area and the fluorescence will recover over time. In contrast, if the mobility is low or limited to regions smaller than the bleached area, as in

the case of a layer of vesicles, there is essentially no fluorescence recovery. This makes FRAP a powerful tool in the characterization of cell membrane mimics.

Other variants of supported cell membrane mimics include tethered and polymer-supported lipid bilayers.<sup>77, 78</sup> For certain applications, these are promising alternatives to conventional SLBs, because they can also be formed on materials that do not promote spontaneous SLB formation from vesicles and because they provide a liquid reservoir under the lipid bilayer. The latter property may be particularly beneficial when working with membrane-protruding proteins. Another concept is that of free-hanging membranes<sup>79</sup> (SLBs that span apertures), which also provides space under the membrane and liquid reservoirs on both sides of the lipid bilayer.

Note that it is possible to produce patterns of both SLBs and vesicles. In the case of vesicles, the DNA-controlled immobilization strategies discussed above are promising for multiplexed sorting of vesicles on the sensor surface.<sup>58</sup> DNA-controlled binding, combined with materials-specific surface modifications, can also be used to specifically attach vesicles to the most sensitive regions of a nanosensor.<sup>80</sup> Several techniques have been developed to create patterns or patches of SLBs. For example, barriers on a SiO<sub>2</sub> surface can be used to hinder lipids from diffusing between two adjacent fluid SLB patches.<sup>81</sup> Microcontact printing with patterned stamps is another attractive approach to create SLB patches<sup>82</sup> and more serial techniques include dip-pen nanolithography,<sup>83</sup> and nanoshaving.<sup>84</sup>

In this work, SLB formation from lipid vesicles was investigated with nanoplasmonic sensing. The concepts of plasmonic and nanoplasmonic sensing are discussed in the following two chapters.

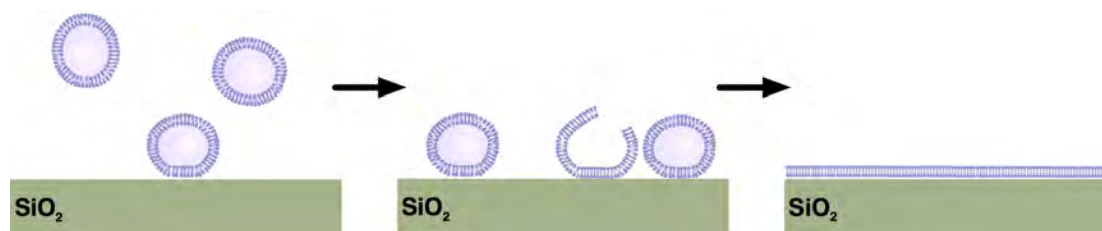


**Figure 2.3.** Simplified schematic illustration of supported lipid bilayer formation from vesicles on SiO<sub>2</sub>. The vesicles first adsorb and stay non-ruptured on the surface and after a critical surface coverage they rupture to form a SLB.



## Chapter 3 Plasmonics – basics and sensing

This chapter is aimed at providing a general introduction to the field of plasmonics as a basis for the next chapter that focuses on plasmonic holes. In particular, the use of plasmonics for refractive index-based sensing will be discussed.

In plasmonics, the interaction of electromagnetic radiation (light) and metallic interfaces is explored. The research field is exceptionally broad, with promising applications ranging from cheap light emitting diodes,<sup>85-87</sup> data storage systems<sup>88</sup> and more efficient solar cells<sup>89</sup> to the recently developed SPACER,<sup>90, 91</sup> which is a plasmon-based laser and even more exotic phenomena, such as negative refractive index materials and invisibility cloaks.<sup>85, 92</sup> Plasmonic applications within biology and medicine include both diagnostics and treatment of cancer<sup>93, 94</sup> and, as explored in this work, bioanalytical sensors.<sup>32, 95</sup>

The two main plasmonic components relevant for sensing applications are *surface plasmon polaritons* (SPPs) and *localized surface plasmons* (LSPs, also referred to as nanoplasmons). While SPPs are associated with flat metal films, LSPs are associated with metal nanostructures. Plasmonic excitations associated with metal films perforated with nanoholes are discussed in Chapter 4.

### 3.1 Short introduction to the optics of metals

The optical properties of a bulk material, such as its color, can be described by the material's relative permittivity or dielectric function  $\epsilon$ . In the simplest approximation, a metal can be described as a free electron gas with the metal dielectric function  $\epsilon_m$  given by:

$$\epsilon_m(\omega) = 1 - \frac{\omega_p^2}{\omega^2} \quad (3.1)$$

where  $\omega$  is the angular frequency of light and  $\omega_p$  the plasma frequency of the metal ( $\omega_p \approx 1.4 \times 10^{16}$  Hz for gold)<sup>96</sup>. Note that the dielectric function of the metal is frequency dependent and that  $\epsilon_m < 0$  and  $\epsilon_m > 0$  for frequencies below and above the plasma frequency, respectively. This means that the refractive index, which is the square root of the dielectric function ( $n = \epsilon^{1/2}$ ), is imaginary and real for frequencies below and above  $\omega_p$ , respectively. For metals such as gold and

---

silver, the frequency of visible light falls below  $\omega_p$ , resulting in an imaginary refractive index and highly reflective and mirror-like surfaces.

Damping of the electron motion due to inelastic processes such as collisions in the material can be taken into account by introducing a damping frequency  $\gamma$  according to:

$$\varepsilon_m(\omega) = 1 - \frac{\omega_p^2}{\omega^2 + i\gamma\omega} \quad (3.2)$$

The dielectric function in this so-called Drude model is thus complex ( $\varepsilon_m = \varepsilon_m' + i\varepsilon_m''$ ) with the two components being:<sup>97</sup>

$$\varepsilon_m'(\omega) = 1 - \frac{\omega_p^2}{\omega^2 - \gamma^2} \quad (3.3)$$

$$\varepsilon_m''(\omega) = \frac{\omega_p^2\gamma}{\omega^3 - \omega\gamma^2} \quad (3.4)$$

For UV-visible-NIR frequencies,  $\omega$  is in the order of  $1-10 \times 10^{15}$  Hz. Hence, for a typical noble metal like gold ( $\gamma_{\text{gold}} \approx 4 \times 10^{13}$  Hz)<sup>96</sup>  $\gamma$  is much smaller than  $\omega$ . This implies both that  $\varepsilon_m''$  is small in this frequency range and that  $\varepsilon_m'$  is close to that described without the damping factor (Eq. 3.1).

According to the discussion above, the metal dielectric function approaches 1 at high frequencies (when  $\omega \gg \omega_p$ ). This is typically not the case for a real metal such as gold due to, for example, the influence of the positive background of the metal ion cores.<sup>97</sup> This can be taken into account by replacing the first term in Eq. 3.2 with  $\varepsilon_\infty$  (typically between 1 and 10),<sup>97</sup> which is the value that  $\varepsilon_m$  approaches when  $\omega \rightarrow \infty$ :<sup>98</sup>

$$\varepsilon_m(\omega) = \varepsilon_\infty - \frac{\omega_p^2}{\omega^2 + i\gamma\omega} \quad (3.5)$$

The simplest free electron gas approximation or the Drude model will mainly be used in the discussions below, but it is worth mentioning that the complete picture for a real metal is not described unless interband transitions in the metal are also considered. This is typically done by adding one or several Lorentz-oscillator terms to the dielectric function.<sup>98</sup>

### 3.2 Surface plasmon polaritons

A surface plasmon polariton (SPP), first predicted by Ritchie in 1957,<sup>99</sup> is an electromagnetic excitation of collective oscillations of the conduction electrons near a metal surface. The SPP propagates as a wave at the interface between the metal and a dielectric medium, such as air or water. The magnetic field oscillates in the plane of the interface (SPPs are transverse magnetic waves). The accompanying electric fields of the SPP have both a longitudinal component in the direction of the propagation and components perpendicular to the interface that decay exponentially into both the metal and the dielectric medium (see Fig. 3.1a).<sup>97</sup> The penetration depth (decay length)\* of the field into the dielectric medium depends on the wavelength of the incident light and on the dielectric functions of both materials and is typically hundreds of nanometers.<sup>100</sup> In sensing applications, the response is generated by changes in the refractive index induced by biomolecular binding within the evanescent field in the dielectric medium. Hence, the decay length is an important parameter when comparing different plasmonic materials for sensing applications, as discussed below.

SPPs carry momentum, described by the wave vector  $k_{\text{SPP}}$ . The magnitude of the wave vector, or the wave number  $k_{\text{SPP}}$ , is given by the dispersion relation:

$$k_{\text{SPP}} = \frac{\omega}{c} \sqrt{\frac{\epsilon_m(\omega) \cdot n^2}{\epsilon_m(\omega) + n^2}} \quad (3.6)$$

where  $n$  is the refractive index of the dielectric medium and  $c$  the speed of light in vacuum.\*\* From the derivation of Eq. 3.6 (see for example the review by Zayatz et al.<sup>101</sup>) it is clear that SPPs only are supported if the real components of the dielectric functions of the two interface materials have opposite signs. Hence, the condition for SPPs may be fulfilled at the interface between a metal (below its plasma frequency such that  $\epsilon_m' < 0$ ) and a dielectric medium, whose dielectric function  $\epsilon = n^2$  is both real and positive. Note that with a complex metal dielectric function, Eq. 3.6 gives a complex wave vector. The imaginary part corresponds to losses in the system and determines, for example, how far the SPP will propagate on the surface. When the imaginary component of the metal dielectric function is small ( $\epsilon_m'' \ll |\epsilon_m'|$ , as for gold in the visible region),

---

\* The decay length is defined as the distance from the surface at which the field amplitude has decreased by a factor  $e$ , where  $e$  is the base of the natural logarithm.

\*\* Note that, for thin metal films, the SPP fields in the metal of the two opposite metal interfaces overlap and a coupled system is formed. This results in symmetric and antisymmetric SPP modes, corresponding to the two SPP fields oscillating in phase or out of phase, respectively.

---

the real part of the wave vector can be approximated from Eq. 3.6 by simply neglecting the imaginary component of  $\epsilon_m$ . This approximation is used in the following discussion.

Because  $\epsilon_m' < 0$  (and  $|\epsilon_m'| > n^2$ ) for all allowed frequencies, we have from Eq. 3.6 that:

$$k_{\text{SPP}} > \frac{\omega}{c} n \quad (3.7)$$

Interestingly, the right hand side in Eq. 3.7 is equal to the wave number for light at frequency  $\omega$  traveling in the same dielectric medium. Because the momentum of a SPP is parallel to the surface, it is the momentum component of the photon parallel to the surface that is relevant for the excitation of SPPs. For light travelling in the dielectric towards the metal surface at an angle  $\theta$ , the wave number component parallel to the surface is:

$$k_{\text{photon}} = \frac{\omega}{c} n \cdot \sin \theta < \frac{\omega}{c} n \quad (3.8)$$

From Eqs. 3.7 and 3.8, the following relation is obtained for any given frequency regardless of incidence angle:

$$k_{\text{photon}} < k_{\text{SPP}} \quad (3.9)$$

This is central, because it means that SPPs will not radiate into the dielectric medium and also that light (incident on the surface in this particular way) cannot excite SPPs. The reason is that both the frequency (energy) and the wave vector (momentum) must be conserved in the conversion of photons to SPPs or vice versa. Figure 3.1b illustrates graphically that the dispersion relations for light in air and SPPs at a metal/air interface do not coincide. The straight solid line shows the dispersion relation for light parallel to the metal surface and the shaded grey area represents all possible incidence angles (the light cone). It is clear that the photons have too small wave vectors in order to excite SPPs. Further, while the dispersion relation for light is linear, the dispersion curve for the SPP is not, but instead approaches  $\omega_p(1 + n^2)^{-1/2}$  for large values of  $k_{\text{SPP}}$ .

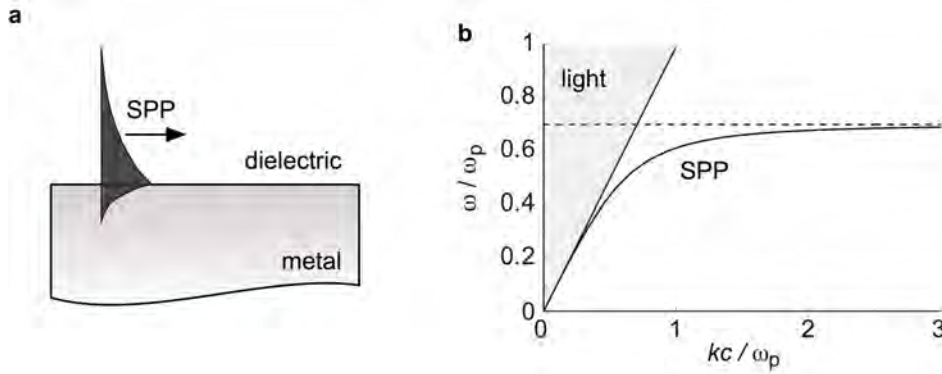


**Figure 3.1.** (a) Schematic illustration of a SPP propagating at the interface between a metal and a dielectric material. The filled regions illustrate the exponentially decaying fields in both materials. (b) Dispersion relations for SPPs at a gold/air interface and light in air ( $n=1$ ). For the latter, the wave vector parallel to the surface is used and the filled area represents all possible angles of incidence (the light cone). The dashed line indicates that the frequency of the SPP approaches  $\omega_p(1+n^2)^{-1/2}$  for large wave vectors.

**Optical excitation of SPPs.** In 1968, Kretschmann and Raether<sup>102</sup> and Otto<sup>103</sup> presented methods that enable the excitation of SPPs on a flat metal film using light. The two methods are similar in that they circumvent the phase mismatch (or momentum mismatch) using attenuated light that is totally reflected at an interface close to, but different from, the interface where the SPPs are excited. The Kretschmann configuration, illustrated schematically in Fig. 3.2a, is based on guiding light in a glass prism towards a thin metal film. From the discussion above it is clear that this light cannot excite SPPs at the gold/glass interface (see the solid curves in Fig. 3.2b). However, at a given frequency, it can provide the extra momentum needed to match the wave vector of SPPs propagating on the next (metal/air) interface, as shown in Fig. 3.2b. Hence, for a sufficiently thin metal film, the evanescent field from light totally reflected at the glass/metal interface can excite SPPs at the metal/air interface ( $n=1$ ) when the following condition is met:

$$k_{\text{photon}} = k_{\text{SPP}} \Rightarrow \quad (3.10)$$

$$n_{\text{prism}} \cdot \sin(\theta) = \sqrt{\frac{\epsilon_m(\omega) \cdot n^2}{\epsilon_m(\omega) + n^2}} \quad (3.11)$$

Either the frequency (wavelength) or the angle of incidence (or both) can be tuned to find solutions to Eq 3.11. It should also be noted that the process works the other way around; SPPs excited in this way are inherently leaky and can couple out as electromagnetic radiation into the prism.<sup>97</sup> In both the

angular and frequency spectra, a dip corresponding to SPP excitation appears due to absorption in the metal combined with destructive interference between directly reflected light and light that is reemitted from SPPs.<sup>97</sup>

Apart from using the Kretschmann or the Otto configurations, the momentum mismatch between SPPs and light at a metal/dielectric interface can be circumvented using diffraction effects.<sup>101, 104-106</sup> This was in fact also shown in 1968 when Ritchie et al.<sup>105</sup> explored optical anomalies\* in gratings. These anomalies had previously been reported by Wood in 1902 and were later studied by, for example, Rayleigh and Fano.<sup>104, 106, 107</sup> The grating-coupling principle is based on the fact that light that is diffracted by a grating will provide an additional component to the wave vector compared with that of the incident light. The principle also holds for two-dimensional arrays of scattering features on the metal surface, such as a periodic array of nanoholes. This and similar systems will be treated separately in Chapter 4. Recently, Renger et al.<sup>108</sup> showed that SPPs can be excited by free-space photons also on flat metal films using nonlinear effects. The principle is called four wave mixing and is based on three photons (from two different laser beams) that interact to excite a single SPP. Interestingly, in contrast to SPPs excited using the Kretschmann configuration, these SPPs are not necessarily leaky, because this nonlinear excitation process cannot simply be reversed into a radiative emission process.

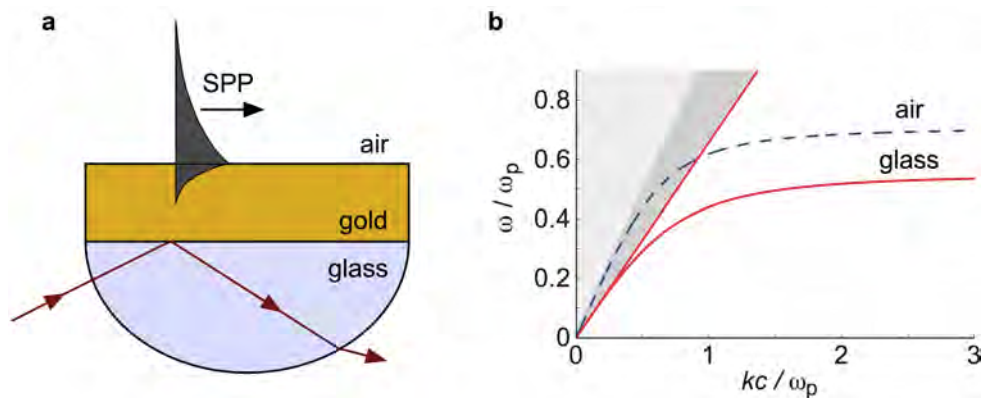


**Figure 3.2.** (a) Schematic of the Kretschmann configuration illustrating how SPPs at the metal/air interface can be excited using light incident through a glass prism from the back of the thin metal film. (b) Dispersion relations for SPPs at a gold/air (dashed trace) and a gold/glass (solid trace) interface. Also shown is the dispersion of light in glass (straight curve) where the shaded grey areas represent all angles of incidence and the darker shaded area represents angles of incidence that can excite SPPs at the metal/air interface.

\* These so-called Wood's anomalies are light waves that are diffracted to move in the plane of the surface.

### 3.2.1 Surface plasmon resonance sensing

A closer inspection of Eq. 3.11 shows that the resonance condition is sensitive to RI changes in the dielectric medium close to the metal/dielectric interface. This means that a change in RI, for example induced by biomolecular binding, will result in shifts in position of the dips in both the angular and frequency spectra, as illustrated in Fig 3.3. This forms the base for using SPPs for RI-based bioanalytical sensing. These sensors are called surface plasmon resonance (SPR) sensors. It is important to note that the glass prism used in the Kretschmann configuration has a dielectric constant not only larger than that of air, but also larger than that of water or typical biologically relevant solutions. This enables the concept also to be used in liquid environments to investigate biomolecular reactions in real-time. Liedberg and coworkers developed the first refractometric biosensor based on SPR in 1983.<sup>14</sup> In their pioneering work, they were able to probe antigen-antibody binding in real-time on a silver surface. After the report of the first SPR biosensor, commercial systems, such as those from the Swedish-based company Biacore (now GE Healthcare Biosciences AB), have been developed and are now widely used around the world. There are also several extensions of the concept including surface plasmon enhanced fluorescence spectroscopy and imaging SPR.<sup>109, 110</sup>

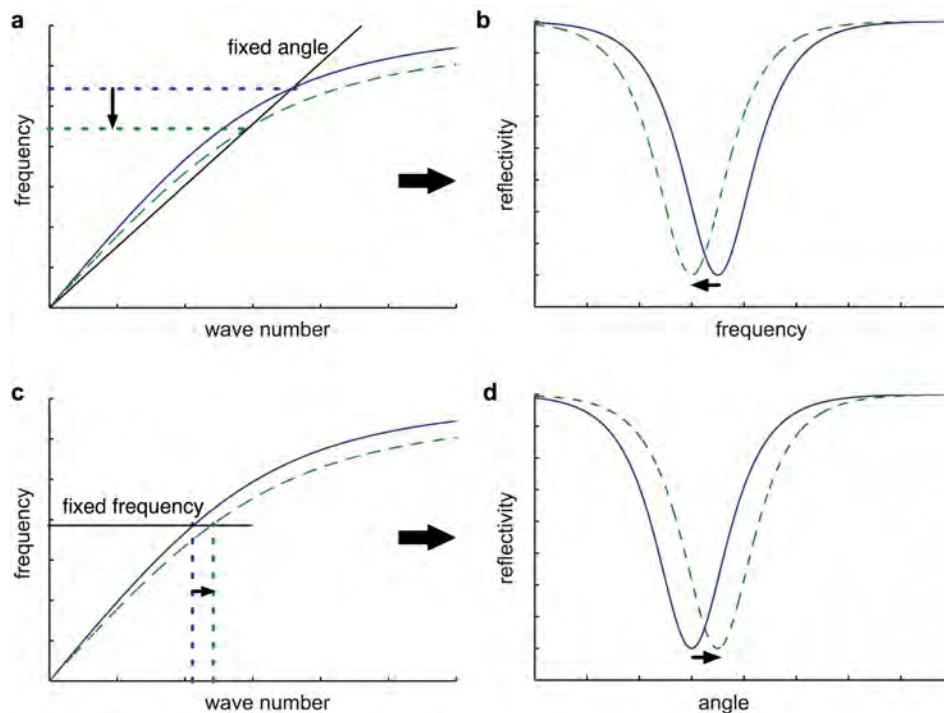


**Figure 3.3.** The SPR sensing concept illustrated for an RI increase (solid curves to dashed curves). **(a, b)** At a fixed angle (the light dispersion is shown as a solid straight line) an increase in RI results in a decrease in the SPR frequency and a corresponding shift in the position of the dip in the frequency spectrum (red-shift of the wavelength). **(c, d)** At a fixed frequency, there will be an increase in the position of the dip in the angle spectrum. Note that the spectra are only schematics used to illustrate the concept.

### 3.3 Localized surface plasmons

Metal nanoparticles cannot sustain SPPs, because there is simply no space for them to propagate. Instead, light can couple to local collective oscillations of the free electrons of the metal particle, as depicted schematically in Fig. 3.4a. These excitations are called localized surface plasmons (LSPs) or nanoplasmons. They are fundamentally different from SPPs as they do not propagate and thereby do not carry momentum. As a result and in contrast to the excitation of SPPs, there is no phase matching condition that has to be considered and LSPs can be excited by free-space photons.

LSPs are excited at certain resonance frequencies (or resonance wavelengths, typically in the visible region), resulting in scattering and absorption at these frequencies. This explains why metal nanoparticles have bright colors, as was used already by the Romans to color glass. The oldest and probably most famous example is the Lycurgus cup, a Roman glass beaker made in the 4<sup>th</sup> century.<sup>111</sup> Metal nanoparticles (gold/silver alloy) were embedded in the glass, which explains the cup's beautiful dichroic optical properties. The plasmonic particles scatter green light strongly, which makes the cup appear green when it is illuminated (with white light) from the side or the front. For the same reason, the cup appears red when it is illuminated from within or from behind, because the green light is removed from the transmitted light by scattering and absorption by the particles (see Fig. 3.4b).

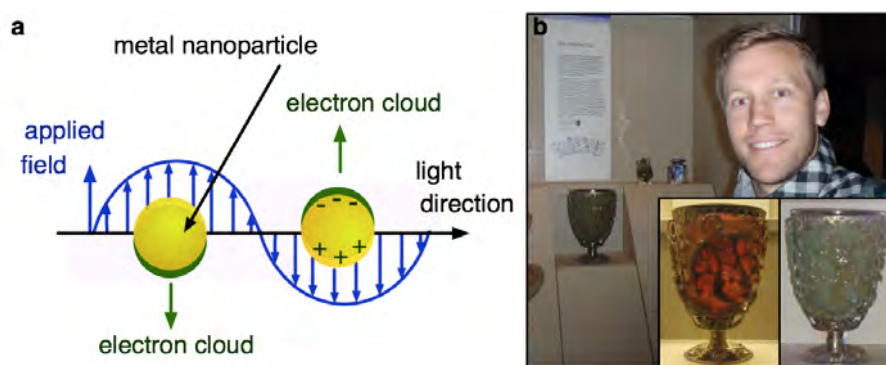


**Figure 3.4.** (a) Illustration of light interacting with metal nanoparticles. (b) The author next to the Lycurgus cup on display at the British Museum in London. The left and right insets show the cup imaged with illumination from behind and using the camera flash, respectively.

When light interacts with a particle it will induce a dipole moment that is proportional to the applied electric field via the polarizability  $\alpha$ . For a sphere that is much smaller than the wavelength, the applied electric field can be assumed to be constant over the whole particle. In this electrostatic approximation the polarizability is given by:

$$\alpha = 4\pi a^3 \frac{\varepsilon_m(\omega) - n^2}{\varepsilon_m(\omega) + 2n^2} \quad (3.12)$$

where  $a$  is the radius of the particle and  $n$  is the refractive index of the dielectric surrounding. It is clear that the polarizability will obtain its maximum value when the denominator is minimized. Because  $\varepsilon_m'' \ll |\varepsilon_m'|$  in the visible for metals like gold (see above), this occurs to a first approximation when:

$$\varepsilon_m'(\omega) = -2n^2 \quad (3.13)$$

This is the so-called Fröhlich condition, corresponding to the resonance condition for excitation of LSPs, or the localized surface plasmon resonance (LSPR), for small metal nanospheres in the electrostatic approximation.<sup>97</sup> By analogy with the discussion on SPPs above,  $\varepsilon_m'$  must be negative in order to fulfill Eq. 3.13, restricting the excitation of LSPs to particles made of metal (or dielectric particles surrounded by metal as discussed in Chapter 4). A real metal has a non-zero imaginary component of the dielectric function, which hinders the polarizability from approaching infinite values at resonance. Note that the resonance condition (Eq. 3.13) is directly related to the refractive index of the surrounding medium. This forms the base for using nanoplasmonic structures for RI-based sensing, as discussed in detail below.

In this context, it is important to note that the excitation of LSPs results in both scattering and absorption, with corresponding scattering and extinction peaks that can be observed in the far-field (extinction = absorption + scattering) by dark-field and transmission-mode optical spectroscopy, respectively. Hence, in contrast to the excitation of SPPs on a flat metal surface, no prism coupling is needed to excite LSPs. In turn, this opens up for relatively simple instrumentation. The optical extinction cross section  $\sigma_{\text{ext}}$  of a metal particle was derived already in 1908 by Gustav Mie.<sup>112</sup> For particles much smaller than the wavelength of light (in the electrostatic dipole limit) the Mie theory is reduced to:<sup>31</sup>

$$\sigma_{\text{ext}}(\omega) = \frac{12\pi a^3 \omega}{c} n^3 \frac{\varepsilon_m''(\omega)}{[\varepsilon_m'(\omega) + 2n^2] + \varepsilon_m''(\omega)^2} \quad (3.14)$$

It is clear that the extinction will be highest at the resonance condition (at the LSPR, Eq. 3.13). It should also be noted that  $\varepsilon_m''$  determines the width of the extinction peak. This can explain why noble metals such as gold and silver, which have small imaginary components (small damping), provide relatively sharp peaks and bright colours.

Apart from spheres, the optical properties can be solved analytically for only a few other types of structures, such as ellipsoids. The optical properties of structures that are similar to ellipsoids, such as nanodisks (used in Paper V) or

nanorods, can be well described by approximating them as prolate (“cigar-shaped”) and oblate (“pancake-like”) spheroids, respectively. Note that, such non-spherical structures are asymmetric and that the LSPR will depend on the polarization of the incident field. For high-aspect ratio structures, two plasmon peaks may even be resolved, corresponding to resonances at different polarizations.<sup>113</sup> The longitudinal resonance (e.g. excitation along a gold nanorod or along the surface of a disk) red-shifts approximately linearly with the aspect ratio of the structure.<sup>113, 114</sup> This makes it possible to tune the extinction peak position (i.e. the colour) of these structures over a wide range of wavelengths.

Note that the electrostatic approximation used above describes the optical properties fairly well for structures in the order of tens of nanometers. For larger particles, with sizes approaching the wavelength of the incident light, the applied electric field can no longer be considered constant over the particle. This results in retardation of the depolarization field inside the particle and a red-shift of the LSPR.<sup>115</sup> Moreover, an increase in radiative losses for growing particle sizes weakens the resonance, resulting in a broadening of the peak.<sup>97, 116</sup>

The approximations used above for small particles also fail to correctly explain the optical properties of particles that are comparable to or smaller than the effective mean free path of the electrons in the metal (below  $\approx 10$  nm), because elastic damping at the particle surface becomes significant.<sup>116</sup> For even smaller particles (radius around 1 nm), one needs to start considering quantum mechanical effects.<sup>97</sup>

### 3.3.1 Localized surface plasmons resonance sensing

It is clear that the resonance condition for excitation of LSPs (Eq 3.13) is sensitive to changes in the refractive index  $n$  of the surrounding environment. Hence, not only SPPs, but also LSPs can be used for RI-based label-free biosensing. However, despite the use of colloidal gold in decorations for centuries, the LSPR sensor was developed many years after Liedberg’s first SPR sensor based on SPPs. The first report on LSPR sensing (also referred to as nanoplasmonic sensing) was presented by Englebienne in 1998, who monitored changes in the plasmon resonance of gold particles suspended in solution as a means of probing antigen-antibody binding.<sup>30</sup> More common nowadays are surface-based nanoplasmonic sensing platforms using all sorts of differently shaped structures depending on the specific application of interest.<sup>41, 117-121</sup>

The optical behavior of most structures can be qualitatively described by replacing the factor 2 in Eq. 3.13 with a shape factor  $\chi$ :<sup>31</sup>

$$\varepsilon_m'(\omega) = -\chi n^2 \quad (3.15)$$

Using the free electron gas model (Eq. 3.1) for the metal dielectric function and shifting from frequencies to wavelengths, an approximate resonance peak position wavelength  $\lambda_{\text{peak}}$  is obtained as:

$$1 - \frac{\lambda_{\text{peak}}^2}{\lambda_{\text{p}}^2} = -\chi n^2 \Rightarrow$$

$$\lambda_{\text{peak}} = \lambda_{\text{p}} \sqrt{\chi n^2 + 1} \quad (3.16)$$

where  $\lambda_{\text{p}}$  is the plasma wavelength related to  $\omega_{\text{p}}$  as  $\lambda_{\text{p}}=2\pi c/\omega_{\text{p}}$ . Note that while the free electron model does not provide accurate estimations of the particle plasmon resonance wavelength, it is here used as a first means to understand the qualitative behavior resulting from small changes in different parameters. The derivative of Eq. 3.16 with respect to  $n$  gives the sensitivity  $S$  of the plasmon resonance peak position to small changes in the RI of the medium that surrounds the structure (bulk RI sensitivity):

$$S = \frac{d\lambda_{\text{peak}}}{dn} = \lambda_{\text{p}} \frac{\chi^{1/2}}{\sqrt{1 + 1/\chi n^2}} \quad (3.17)$$

Equations 3.16 and 3.17 suggest that both the bulk RI sensitivity and the absolute peak position increase with the shape factor, which is 2 for a sphere, but can be tailored to values above 20 for high-aspect ratio structures.<sup>95</sup> This is in agreement with the above discussion on shape effects on the LSPR. Further, Eq. 3.17 predicts that the sensitivity will only weakly increase with the refractive index. However, note that the free electron gas model is a simplified approximation of the dielectric function of a real metal. In fact, due to contributions from interband transitions in the metal, the real part of the dielectric function for gold can be better approximated as being linearly dependent on the wavelength in the visible wavelength range (500-800 nm,  $\epsilon_{\text{m}}' = a - b\lambda$  with  $a=34.66$  and  $b=0.07$ ),<sup>122</sup> which inserted into Eq. 3.15 gives:

$$a - b\lambda_{\text{peak}} = -\chi n^2 \Rightarrow$$

$$\lambda_{\text{peak}} = \frac{\chi n^2}{b} + \frac{a}{b} \quad (3.18)$$

Hence, this gives that the bulk sensitivity is instead linearly dependent on RI:

$$S = \frac{d\lambda_{\text{peak}}}{dn} = 2 \frac{\chi n}{b} \quad (3.19)$$

---

Indeed, calculated absorption spectra for gold nanorods confirmed that the sensitivity increases linearly with the refractive index.<sup>123</sup> In Paper I, we experimentally verified that the bulk RI sensitivity increases with RI for plasmonic holes in a thin gold film. The results for gold holes were compared with those of a silver structure with the same geometry, which was found to possess approximately constant bulk RI sensitivity for increasing RI. However, when narrow RI intervals are used, as in most practical situations, one can still assume that the bulk RI sensitivity is constant also for gold structures. This, in turn, simplifies the analysis of the LSPR data.

### 3.3.2 LSPR versus SPR sensing

Note that the bulk RI sensitivity of LSPR sensors is generally lower than that of SPR sensors. However, the decay length of the plasmonic field associated with LSPs is also considerably shorter (tens of nanometers or less) compared with that of typical SPPs on flat metal surfaces (hundreds of nanometers).<sup>124, 125</sup> As a result, a thin (<10 nm) adsorbed film will occupy a larger fraction of the total sensing volume for a LSPR sensor compared with a SPR sensor. In turn, responses induced by changes in the *interfacial* refractive index due to, for example, binding of biomolecules to the surface, are comparable for the two sensor concepts.<sup>126</sup> This also makes the concepts similar in terms of signal-to-noise ratios (see also Section 3.3.3), which ultimately determines the detection limit of the sensor. Further, as explored in Papers I and II and discussed in Chapter 6, plasmonic sensors with short decay lengths provide a unique means to probe structural changes on a surface without the introduction of external labels. It should also be noted that there are ways of utilizing the whole plasmonic field for sensors with long sensing depths, for example using dextran matrices.<sup>127</sup>

Apart from the competitive performance of LSPR sensors compared with existing state of the art commercial instruments, they have other interesting potentials. One is that the instrumentation can be made relatively simple and inexpensive. This is mainly due to the fact that there is no restriction on the angle of excitation, which enables transmission-mode measurements. With a future point-of-care diagnostic application or hand held device in mind we simplified the LSPR sensing concept further by converting the optical signal into an electrical output directly on the sensor chip (Paper V). Another interesting feature of LSPR sensors is that the sensitive field is, in contrast to the field of propagating plasmons, spatially confined in three dimensions.<sup>35</sup> This, together with the possibility to measure on single plasmonic particles,<sup>128, 129</sup> allows for the development of dense array-based sensing<sup>20</sup> and multiplex screening of, for example, drug candidates. Finally, the potential of LSPR structures for bioanalytical sensing is directly reflected by the many interesting and relevant applications that have been developed since the first LSPR sensor report in 1998. These include the analysis of recombinant protein expression,<sup>130</sup> the detection of biomarkers for Alzheimer's disease<sup>131</sup> and the investigation of DNA hybridization<sup>132</sup> to mention only a few examples.

### 3.3.3 Performance of LSPR sensors

Although the magnitude of the plasmon resonance wavelength shifts induced by bulk or local RI changes is important and of fundamental interest, there are additional parameters that will affect the performance of the sensor. The “figure of merit” (FOM) defined as the bulk RI sensitivity divided by the full width at half maximum (FWHM) was introduced as a means to consider that a peak with small width can be tracked with better precision than a wide peak.<sup>133</sup> Narrow peaks can, in turn, be obtained using metals with low values of the imaginary part of the dielectric function (see Eq. 3.14), such as gold and silver. These are also the two plasmonic materials most commonly used for biosensing. Gold has the additional advantage of being less prone to oxidation than silver. Further, there are established surface modification schemes available for gold (see also Section 1.4). Gold was therefore used as the plasmonic material in all the work presented in this thesis apart from in Paper I, where the sensing capabilities of gold and silver hole structures with the same geometry were compared. In that study, layers of silicon oxide protected both metals from oxidation.

The main underlying reason for the benefit of a narrow peak is that a spectrometer does not provide direct values of peak positions, but information on changes in intensity at different wavelengths around the peak. The signal-to-noise ratio is directly related to the magnitude of these intensity changes (see also Section 5.2). In turn, for a given peak shift, the highest intensity changes are provided by the peak with the highest slopes (on both sides). In this respect it is important to note that the peak slopes are not only determined by the peak width, but also by the magnitude of the peak, which is therefore an additional parameter that is important for the performance of a nanoplasmonic sensor. The importance of these three parameters (RI sensitivity, peak width and peak magnitude) has recently begun to be acknowledged by the community when comparing the potential of different nanoplasmonic structures for sensing applications (see Paper V).<sup>134, 135</sup> Note also that the parameter monitored during a biosensing experiment is not necessarily the peak position. For example, in Paper V we monitored changes in the extinction of gold nanodisks at a single wavelength where the slope of the peak was high.



## Chapter 4 Plasmonic nanoholes

Two main types of plasmon resonances have been discussed so far, SPPs and LSPs. It has also been described how these concepts can be used for bioanalytical sensing. While SPPs can be excited on flat metal films, LSPs are associated with metal nanostructures. This section extends the concept of plasmonics to the fascinating world of metal nanoholes. Interestingly, a flat metal film that is perforated with nanosized apertures can support both SPPs and LSPs, because such a structure provides both flat metal/dielectric interfaces for the propagation of SPPs and nanosized features that can sustain localized resonances. It will be discussed that both the size and the shape of individual holes as well as their arrangement are important for the optical properties of perforated metal films. In particular, focus is on short-range ordered (non-periodic) nanoholes in thin (tens of nanometers) gold films, which is the type of structure that was used in most of the work of this thesis. In the last section, a number of unique possibilities provided by perforated metal films are highlighted.

### 4.1 Spherical metallic voids

LSPs are not restricted to discrete particles, but can also be sustained by dielectric nanostructures surrounded by metal. For example, the polarizability of a dielectric void inside a bulk metal (the inverse structure of a metal particle) can be found by simply switching the position of  $n^2$  and  $\epsilon_m$  in Eq. 3.12:<sup>97</sup>

$$\alpha = 4\pi a^3 \frac{n^2 - \epsilon_m(\omega)}{n^2 + 2\epsilon_m(\omega)} \quad (4.1)$$

The modified Fröhlich LSP resonance condition for such a void system is then:

$$\epsilon_m'(\omega) = -\frac{1}{2}n^2 \quad (4.2)$$

Note that the induced electric fields ( $E_{\text{induced}} \propto -\alpha E_{\text{applied}}$ ) of a void and a particle have opposite directions with respect to the applied field, as illustrated schematically in Fig. 4.1.<sup>136</sup> It is evident from Eq. 3.12 that the induced electric field for a particle is antiparallel to the applied field (remember that  $\epsilon_m' < 0$ ). In contrast, the induced field of a void will be parallel to the applied driving field.



**Figure 4.1.** Schematic illustration of the dipolar plasmon resonances of a particle (left) and a void (right). The left arrow indicates the direction of the applied field (at a certain point in time) and the other arrows indicate the directions of the induced electric fields.

## 4.2 Single nanoholes in thin metal films

Similar to a spherical void embedded in a metal, single holes in a metal film can also sustain dipolar optical resonances.<sup>97, 137, 138</sup> These resonances, here denoted hole plasmons (HPs), have been found to behave similarly to those of discrete metal structures, such as nanodisks (the inverse of a nanohole).<sup>137, 138</sup> One of the main differences between holes and disks is that the HP has an additional decay channel into SPPs, as verified experimentally using near-field optical techniques.<sup>137</sup> In fact, the optical properties of a hole in a thin metal film on a glass substrate, including the influence of hole diameter and film thickness on the plasmon resonance, can be described from the resonance conditions for antisymmetric SPPs using the hole as the excitation source.<sup>139</sup> Conceptually, one can picture the HPs of a single hole as LSP-like resonances that decay into SPPs.

Single holes in a thin metal film provide similar sensing capabilities with respect to both sensitivity and decay length to those of typical LSPR structures.<sup>35</sup> Moreover, theoretical studies show that the sensitive HP field is, at least partly, localized to the void of the hole.<sup>137</sup> From a sensing perspective, this resembles the localized fields associated with plasmonic particles, as discussed in Chapter 3.

### 4.3 Periodic arrays of nanoholes in metal films

We now move from the case of a single hole in a metal film to metal films that are perforated with many holes. If the holes are arranged in a periodic square array, the structure can act as a two-dimensional grating (see also Section 3.2).<sup>140</sup> This means that light that is diffracted by the array will provide additional momentum components,  $u\mathbf{G}_x$  and  $v\mathbf{G}_y$ , to that of the incident photons, where  $x$  and  $y$  denotes the orientation of the hole array and  $u$  and  $v$  are integers representing the scattering orders of the array. For light incident on a square-array of apertures in a metal film, the phase matching condition for excitation of SPPs becomes:<sup>141</sup>

$$k_{\text{SPP}} = \left| \mathbf{k}_{\text{photon}} \cdot \sin(\theta) + u\mathbf{G}_x + v\mathbf{G}_y \right| \quad (4.3)$$

In contrast to the situation of a flat metal film without holes (see Chapter 3), the additional momentum provided by the grating makes it possible to excite SPPs at an interface using photons incident from the same side. In fact, SPPs can even be excited at normal incidence, to a first approximation at wavelengths ( $\lambda_{\text{SPP}}$ ) that satisfy:<sup>142</sup>

$$\lambda_{\text{SPP}} = \frac{P}{\sqrt{u^2 + v^2}} \sqrt{\frac{\epsilon_m n^2}{\epsilon_m + n^2}} \quad (4.4)$$

where it was used that  $\omega=2\pi c/\lambda$  and that  $|\mathbf{G}_{x,y}|=2\pi/P$ , with  $P$  being the lattice spacing.<sup>141</sup> It was also assumed that  $k_{\text{SPP}}$  can be described by Eq. 3.6 and hence, that the metal film is sufficiently thick so that effects from coupling between SPPs on the opposite interfaces can be neglected (above around 100 nm for gold films)<sup>143</sup>. The resulting SPPs of a periodic hole array can be described as SPP Bloch waves, or standing waves between the holes.<sup>144</sup>

It is clear from Eq. 4.4 that the plasmon resonance wavelengths are sensitive to changes in RI, as verified experimentally and utilized for sensing by Brolo et al.<sup>145</sup> Considering that a periodic array of metal nanoholes can act as a grating, it may not be surprising that the optical properties and sensing capabilities of these structures are similar to those of conventional grating-coupled SPR. The bulk sensitivity is typically in the order of hundreds of nanometers per refractive index units (nm/RIU) and the decay length hundreds of nanometers.<sup>145</sup> For example, Im et al.<sup>146</sup> used atomic layer deposition to show that there is essentially no decrease in the sensitivity to changes in RI within 50 nm from the surface for 200 nm thick gold and silver nanohole arrays. This should be compared with the field having decayed almost completely after 50 nm in the case of thin metal films perforated with nanoholes that are instead arranged in a short-range order,<sup>125</sup> as discussed in the next section.

## 4.4 Short-range ordered nanoholes in thin metal films

Figure 4.2a shows a scanning electron microscopy (SEM) image of a thin (30 nm) gold film perforated with 130 nm in diameter nanoholes that are arranged in a short-range order. The short-range order refers to a distribution with a characteristic separation between the nearest neighbor holes, but without long-range order (no periodicity, see also Section 5.1.1). Qualitatively, the optical properties of such plasmonic hole films are similar to the properties of discrete LSPR structures, as demonstrated in a direct comparison between short-range ordered metal nanodisks and nanoholes with the same dimensions.<sup>147</sup> For example, the bulk RI sensitivity of short-range ordered holes in thin metal films has values similar to those of LSPR sensors.<sup>147</sup> This is in contrast to periodic plasmonic hole arrays, whose sensitivity better resembles that of grating-coupled SPR sensors, as discussed above. We (Paper II) and others<sup>125, 148</sup> have shown that the average decay length of the plasmonic field is in the order of tens of nanometers for short-range ordered holes in thin gold films supported on glass. This is again closer to that of typical LSPR structures<sup>124, 125</sup> and single holes in thin metal films<sup>35</sup> rather than that of typical SPR structures, including reported values for periodic plasmonic holes.<sup>145, 149, 150</sup> On the other hand, the optical properties of short-range ordered holes have been demonstrated to be highly sensitive to the characteristic separation between holes,<sup>147</sup> which highlights the role of SPPs in the system, enabling holes to interact at significantly longer distances (hundreds of nanometers) compared with discrete plasmonic particles.<sup>114, 147</sup> In this respect it is also interesting to note that thin (tens of nanometers) metal films on glass substrates support antisymmetric SPPs and that the fields of those SPPs are more tightly confined to the surface compared with those of non-coupled SPPs associated with thicker films.<sup>97, 137</sup> This field confinement is in agreement with the short decay lengths reported for short-range ordered holes in thin metal films. To the best of my knowledge, the decay length of short-range ordered holes in optically thick metal films has not yet been reported.

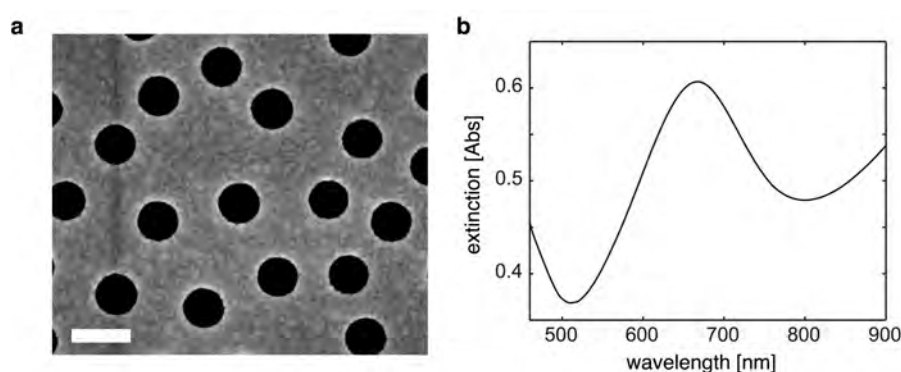


**Figure 4.2.** (a) Scanning electron microscopy image of a typical sample with short-range ordered nanoholes (diameter around 130 nm) in a 30 nm thick gold film supported on glass. The scale bar is 200 nm. (b) Extinction spectra acquired in air of the same sample.

Dahlin et al.<sup>151</sup> demonstrated that short-range ordered holes in a thin metal film can be used for bioanalytical sensing based on the plasmon resonance being sensitive to changes in RI within the void of the holes. The structure can be produced using simple and scalable nanofabrication methods (see Chapter 5) and provides excellent sensing capabilities. This work has to a large extent been focused on exploring and utilizing the characteristic features of short-range ordered nanoplasmonic hole systems (see Section 4.7 and Chapter 6).

## 4.5 Effect of film thickness

A thin gold film (tens of nanometers) is semi-transparent to light in the visible wavelength range and therefore optically thin. For such structures, the excitation of plasmons is typically associated with extinction peaks, as reported for short-range ordered holes by Prikulis et al.<sup>147</sup> and as recently presented for periodic nanohole arrays.<sup>152, 153</sup> For a thick and opaque metal film (around 200 nm thick)<sup>140</sup> perforated with nanoholes, the excitation of plasmons can instead result in an enhanced transmission, with corresponding peaks in the transmission spectrum (dips in the extinction spectrum).<sup>140, 154</sup> In fact, considering only the area of the holes, certain hole structures can even exhibit extraordinary transmission, with transmission efficiencies above unity in certain wavelength regions.<sup>140</sup> Moreover, corrugations around a nanohole can act as an antenna to further enhance the transmission.<sup>155</sup> Although the discussion in this thesis is mainly focused on properties that are important for RI-based sensing, it is worth noting that the full picture of the optical properties of plasmonic hole systems is complex. It includes considerations of interference effects between light that is directly transmitted through the holes and scattered light originating from the excitation of plasmons as well as contributions from Wood's anomalies.<sup>144, 152, 156-158</sup> However, regardless of whether a plasmonic system provides peaks or dips or both in the extinction spectrum, it can be used for sensing as long as its plasmonic resonances are sensitive to changes in the RI of the surrounding environment. Different structures can then provide different sensing capabilities in terms of, for example, bulk RI sensitivity, decay length, peak shape (magnitude, FWHM, etc.) and field localization to the holes. Interestingly, studies on short-range ordered holes have so far primarily been based on relatively thin metal films (15-60 nm),<sup>80, 125, 147, 148, 151, 159, 160</sup> while periodic arrays of holes are typically based on enhanced transmission through optically thick (>100 nm) metal films. Recently, there have been reports on the sensing capabilities of periodic nanohole arrays also in relatively thin metal films.<sup>153, 161, 162</sup> A direct comparison of the sensing properties (bulk RI sensitivity, decay length, field localization etc.) of identical arrays of holes in thin and thick metal films could help to reveal the individual influences of hole arrangement and film thickness, respectively.

---

## 4.6 Effect of hole shape

The optical properties of plasmonic void structures are highly related to the hole geometry. Apart from the possibility to vary the hole diameter<sup>139, 147</sup> and the film thickness<sup>139, 160</sup>, the shape of a hole can be modified in different ways. For example, the optical properties of both single<sup>136</sup> and periodic arrays<sup>163</sup> of elliptical holes have been investigated. Lesuffluer et al.<sup>164</sup> used a periodic double-hole structure to obtain high bulk RI sensitivity ( $\approx 600$  nm/RIU) combined with sharper resonances than for comparable circular hole arrays. In that study, finite-difference time domain simulations revealed a short decay length close to the apexes (20 nm, similar to the decay lengths measured for short-range ordered plasmonic holes in thin metal films). Localized plasmon modes have also been reported for periodic arrays of truncated spherical voids embedded in a metal surface (like spherical voids, but not completely embedded), for which the field localization was highly influenced by the degree of truncation.<sup>165, 166</sup> Moreover, the variation of the geometry of nanobottles (two holes of different diameters stacked on top of each other) could be used to control the field localization in the voids.<sup>167, 168</sup> Other void-like systems suitable for sensing applications include nanoslit arrays<sup>169</sup> and metal multilayer structures, which, for example, have been used for spatially resolved biosensing.<sup>170-172</sup>

## 4.7 Comparing particles and holes

From the above sections it is clear that the optical properties of plasmonic nanoholes can be varied significantly by different design parameters. In particular, it was reasoned that short-range ordered nanoholes in thin metal films provide similar sensing capabilities to sensors that are based on discrete LSPR structures. The work of this thesis has to a large extent focused on utilizing certain unique features of such holes. For example, in contrast to discrete nanoparticles, a perforated metal film is a continuous and conductive film, which can be used as an electrode (Fig. 4.3a and b). This enabled the optical nanoplasmonic sensing method to be combined with techniques based on electrical read-out. In Paper II this was utilized for simultaneous QCM-D and nanoplasmonic measurements on the same surface. Furthermore, holes are unique in the sense that they can be designed to penetrate through the whole substrate (Fig. 4.3c). In this way they can, for example, act as nanofluidic channels with integrated nanoplasmonic elements (Paper III). In contrast, discrete plasmonic particles can be employed as mobile probes (Fig. 4.3d). For example, their strong scattering properties can be used for *in vivo* imaging, which, combined with controlled accumulation, has great potential for improved cancer diagnostics.<sup>173</sup> Moreover, the absorbing components of the plasmonic excitations in particles permit local plasmonic heating and photothermal treatment of cancer.<sup>94, 174-176</sup>

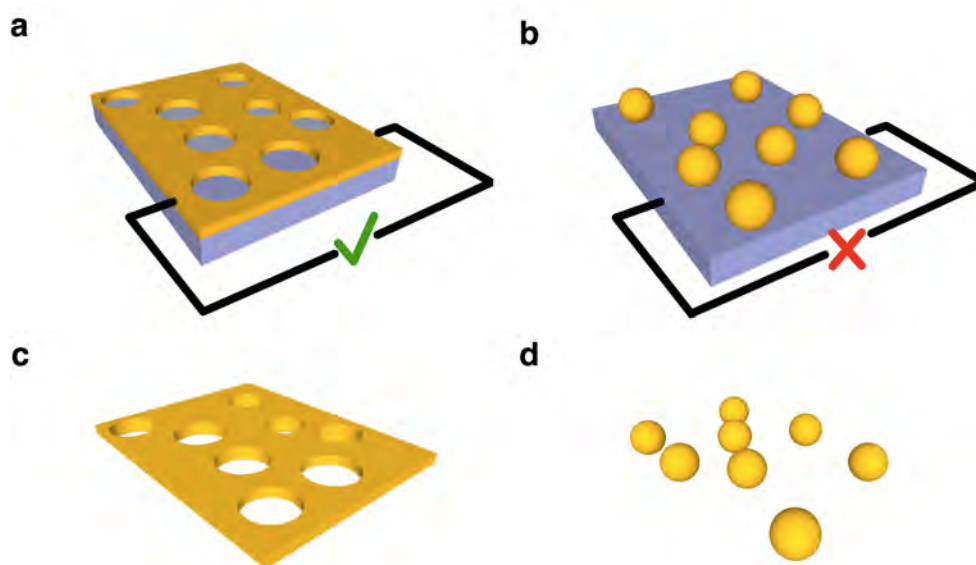


**Figure 4.3.** Schematic illustrations of fundamental differences between nanoholes in a metal film and nanoparticles. **(a)** A metal film perforated with nanoholes is conductive and can enable an electric current to flow. **(b)** Nanoparticles supported on a substrate will not support an electric current. **(c)** Nanoholes without substrate (or that penetrate through the whole substrate) are open on both sides and can be used as nanofluidic channels. **(d)** Nanoparticles without substrate can be used in solution, for example as mobile probes.



## Chapter 5      **Experimental procedures and methods**

This chapter starts with a presentation of various methods of fabricating nanoplasmonic structures, with focus on the techniques used in this work. Next, optical extinction measurements are discussed. This includes important factors to consider when acquiring extinction spectra from either large or small areas as well as the importance of suitable data analysis. Finally, the quartz crystal microbalance with dissipation monitoring (QCM-D) technique is presented. The QCM-D was used in a combined nanoplasmonic and QCM-D setup in Paper II and as a complementary label-free sensing technique in Papers III and IV.

### **5.1      Fabrication of nanoplasmonic structures**

A wide range of nanoplasmonic particles can be fabricated using wet-chemical synthesis, including spheres,<sup>41</sup> rods,<sup>177</sup> cubes,<sup>178</sup> shells,<sup>179</sup> rice<sup>180</sup> and stars.<sup>181</sup> Although surface-based sensing can be enabled by immobilizing these particles on a substrate,<sup>41</sup> it is more common to fabricate surface-based sensors using lithography methods by which the nanostructure is produced directly on the substrate. Electron beam lithography (EBL) and focused ion beam (FIB) lithography are two techniques that can be used to produce surface-supported nanoplasmonic structures with more or less full control of both shape and distribution and with a spatial resolution in the order of tens of nanometers.<sup>182, 183</sup> In EBL, a nanopattern is first defined in a resist by scanning a highly focused electron beam over the surface followed by development in an organic solution. Subsequent etching, metal deposition and/or lift-off processes can then be used to transfer the pattern into a plasmonic metal nanostructure on the substrate. FIB milling is also based on scanning a beam over the surface, but instead of “writing” in a resist, a focused ion beam is used to mill nanopatterns directly in, for example, a thin gold film.<sup>183</sup>

**Parallel nanofabrication.** EBL and FIB lithography are particularly useful for the investigation of complex structures and specific particle arrangements. However, they are not suitable for the production of multiple samples and/or nanostructures over large areas ( $> \text{cm}^2$ ). The reason is that both EBL and FIB lithography are serial in nature and thereby slow and expensive. A number of parallel fabrication techniques have been developed that allow nanostructures to be produced simultaneously instead of one by one. Some of these methods are based on the use of nanopatterned masters, from which several sensor substrates with the same or inverse nanopattern can be fabricated. For

---

example, several elastomeric molds (usually in poly(dimethylsiloxane) [PDMS]) can be produced from one single Si master using soft lithography (molding).<sup>184</sup> Such elastomeric molds can, in turn, be used to produce plasmonic nanostructures using nanoimprint lithography followed by metal deposition<sup>171, 172, 185</sup> or by a combined process called PEEL (phase-shifting photolithography, etching, electron-beam deposition and lift-off).<sup>186</sup> Nagpal et al.<sup>187</sup> developed another method based on deposition of metal and epoxy directly on an ultrasMOOTH Si master followed by template stripping. These methods are all highly versatile in the sense that the type of nanostructures that can be produced is (more or less) only restricted to the patterns provided by the master.

There are also parallel nanofabrication methods that are not dependent on a master. Instead, the nanostructure is defined directly on each sensor substrate. For example, interference lithography can be used to directly define periodic arrays of both plasmonic holes<sup>163</sup> and nanobottles<sup>168</sup> without first making a master. Another concept is based on the use of thin substrate-supported nanoporous alumina as a template for electrodeposition of metals.<sup>188</sup> With this technique, arrays of aligned plasmonic rods can be produced, including segmented and core/shell structures.<sup>189, 190</sup> Furthermore, free-standing arrays of nanotubes can be fabricated by using a sacrificial core made of polypyrrole.<sup>191</sup> We recently contributed by investigating the biosensing capabilities of such nanotubes.<sup>192</sup>

Nanoplasmonic structures can also be fabricated by metal deposition directly onto a planar substrate. The evaporation of sufficiently thin gold films (nominal thickness typically below 10 nm) results in the formation of plasmonic nanoislands on the surface that can be used for sensing applications.<sup>118, 193</sup> Glancing angle deposition (GLAD) is another interesting concept. It utilizes self-shadowing effects obtained when metal is evaporated at high angles with respect to the substrate normal.<sup>194</sup> Combined with controlled sample rotation, GLAD can be used to create structures such as freestanding zig-zag and spiral-like nanorods<sup>194</sup> as well as plasmonic structures for sensing applications.<sup>195</sup>

In this thesis, different versions of colloidal lithography (CL)<sup>196</sup> were employed to fabricate nanostructured surfaces. CL is fast, simple and can be used to fabricate nanostructures over large areas. The concept is based on the self-assembly of nanospheres onto a surface. The pattern created by the colloids (typically hexagonal close-packed or short-range ordered) can be used as a mask to create a wide range of plasmonic structures, including disks,<sup>114</sup> holes,<sup>134, 147, 197</sup> triangles,<sup>198</sup> crescents<sup>199</sup> and nanorings.<sup>200</sup> The variations of CL used in this work are presented in more detail below.

### 5.1.1 Sparse colloidal lithography

Short-range ordered apertures in a metal film can be fabricated by means of sparse colloidal lithography (SCL),<sup>201, 202</sup> as was done in most of the appended papers. The method, often known as colloidal lithography, is rapid, inexpensive and can produce large and high-quality areas of nanostructures. The SCL principle is illustrated schematically in Fig. 5.1. In brief, a clean substrate is functionalized with electrolytes to render the surface positively charged. Negatively charged polystyrene colloids suspended in water (with or without salt) are then let to adsorb onto the surface. While attracted electrostatically to the surface, the charged colloids repel each other and spontaneously arrange themselves into a short-range order, yet without long-range periodicity. The characteristic distance between neighboring particles can be controlled by varying the salt concentration of the colloidal solution.<sup>202</sup> In the next step the colloidal layer acts as a mask during evaporation of metal (gold or silver in this work). This means that the metal is deposited everywhere on the substrate with the exception of under the particles. Subsequent removal of the colloids by tape stripping (admittedly, this sounds too easy, but works excellently) or sonication in, e.g. chloroform, produces a metal film with short-range ordered apertures.

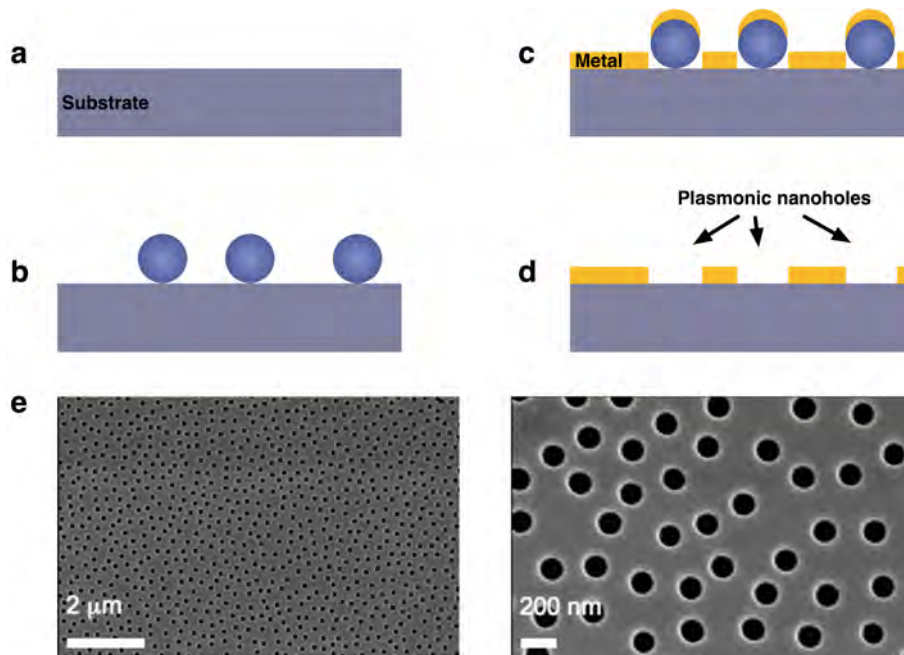


**Figure 5.1.** (a-d) Schematic illustration of the fabrication of short-range ordered apertures in a thin metal film using SCL. The clean substrate (a) is modified with electrolytes before deposition of colloids (b). Metal is evaporated (c) followed by removal of the colloids (d). (e) Two top view scanning electron microscopy (SEM) images at different magnifications of a typical sample produced with SCL. The structure consists of 140 nm diameter short-range ordered nanoholes in a 30 nm thick gold film supported on glass.

### 5.1.2 Hole-mask colloidal lithography

In an extension of SCL, named hole-mask colloidal lithography (HCL), Fredriksson et al. used a sacrificial polymer layer to enable the production of surface-supported nanodisks, oriented elliptical nanodisks, arrays of nanoparticle pairs and nanocones.<sup>201</sup> HCL was used in Paper V and is illustrated schematically in Fig. 5.2. In a first step, SCL is performed on top of a substrate coated with PMMA (poly(methyl methacrylate)) to create a metal mask (for example in chromium). The holes in the metal film are then transferred into the PMMA by oxygen plasma. Subsequent metal deposition and PMMA lift off finally result in plasmonic disks on the substrate.

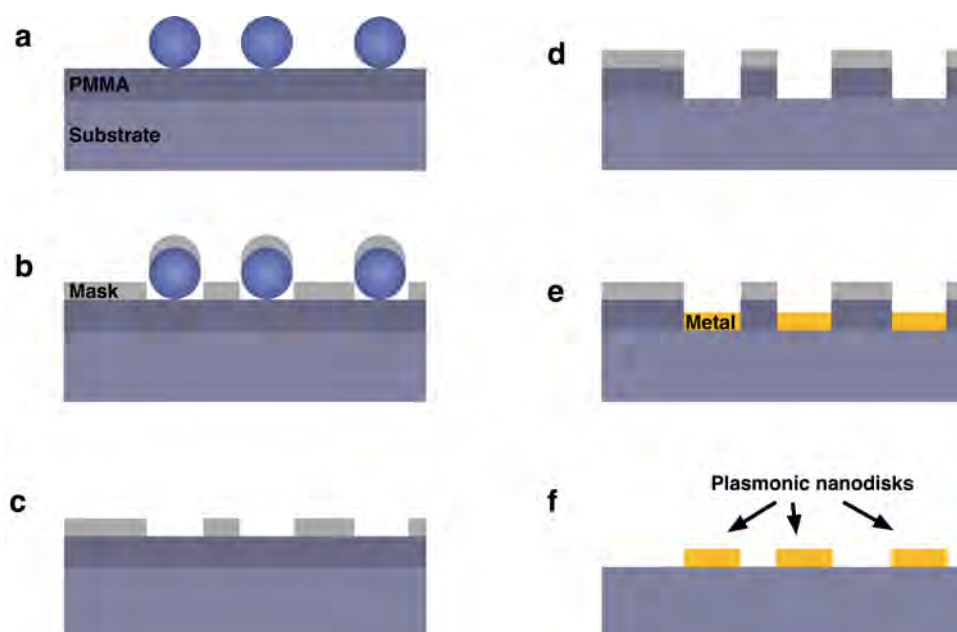


**Figure 5.2.** Schematic illustration of the fabrication of plasmonic nanodisks on a surface using HCL. **(a)** Colloidal deposition on a substrate coated with a thin layer of PMMA. **(b)** Deposition of a hole-mask, typically in chromium. **(c)** Colloidal lift off. **(d)** Oxygen plasma treatment to transfer the nanohole pattern into the PMMA layer. **(e)** Metal evaporation, gold was used in this work (a thin (~1 nm) layer of chromium or titanium is typically used to improve the adhesion between the substrate and the gold disks). **(f)** Metal nanodisks are finally realized by PMMA lift off in, for example, acetone.

### 5.1.3 Nanosphere lithography

Both methods described above (SCL and HCL) provide short-range ordered arrays of nanostructures. Alternatively, a close-packed hexagonal array of colloids can be formed on the surface. Evaporation of metal through such a mask and subsequent removal of the colloids results in arrays of triangular nanoparticles (see Fig. 5.3a and b).<sup>203</sup> This version of CL is usually referred to as nanosphere lithography (NSL).<sup>204</sup> The colloids can also be shrunk before metal evaporation by, for example, plasma etching, which creates a hexagonal array of nanoholes in the metal film (see Fig. 5.3c and d).<sup>153, 196</sup> In a variant of NSL, Coyle et al.<sup>166</sup> combined colloidal masks and electroplating to create truncated spherical nanovoids on a metal surface, as mentioned in Chapter 4.

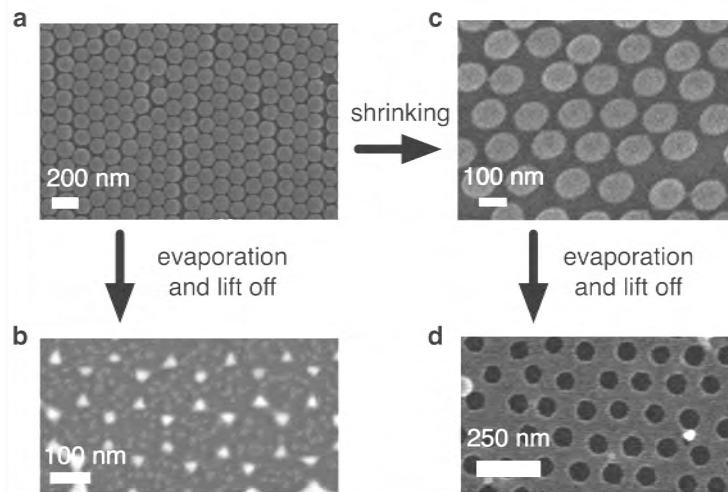


**Figure 5.3.** SEM images illustrating NSL. **(a)** Close-packed array of polystyrene colloids (obtained by spin coating). **(b)** Triangular nanoparticles can be created by metal evaporation followed by removal of the colloids. **(c)** Alternatively, the colloids can be shrunk before evaporation. **(d)** Hexagonal array of nanoholes obtained using a structure like the one in (c) as an evaporation mask.

---

## 5.2 Extinction spectroscopy

There are many different ways of performing biosensing with plasmonic structures. These include transmission-based extinction spectroscopy,<sup>151</sup> reflection spectroscopy<sup>20, 205</sup> and dark-field or scattering spectroscopy.<sup>206, 207</sup> We recently showed that in most cases, with the exception of measurements on single plasmonic particles or holes, extinction spectroscopy will outperform dark-field mode spectroscopy in terms of sensing performance.<sup>208</sup> Extinction spectroscopy was used for biosensing experiments in most of the work presented in this thesis, except in Paper V, in which opto-electrical conversion was directly achieved on the sensor chip.

Excitation of nanoplasmons typically results in both absorption and scattering. There will be a corresponding decrease in the light that is transmitted through the nanoplasmonic structure in the same wavelength range. In extinction spectroscopy, scattering and absorption are measured together as the fraction of light not transmitted through the sample. The extinction  $E_{\text{Abs}}(\lambda)$  can be defined as:

$$E_{\text{Abs}}(\lambda) = \log \frac{I_{\text{reference}}(\lambda)}{I_{\text{sample}}(\lambda)} \quad (5.1)$$

where  $I_{\text{reference}}(\lambda)$  is the incident light (reference) and  $I_{\text{sample}}(\lambda)$  is the light transmitted through the sample. This gives extinction values in absorption units (Abs). An alternative definition of the extinction that instead gives the fraction of light not transmitted, with values from 0 (no extinction) to 1 (no transmission) is:

$$E_{\text{fraction}}(\lambda) = 1 - \frac{I_{\text{sample}}(\lambda)}{I_{\text{reference}}(\lambda)} \quad (5.2)$$

This definition was used in Paper III, while the previous definition was employed in most of the other papers.

### 5.2.1 Extinction measurements on large areas

A schematic illustration of the extinction setup used to probe large areas (around 5 mm in diameter) in this work is presented in Fig. 5.4. The sample is exposed to light from a white light source (tungsten-halogen) via an optical fiber and a collimating lens. The forward transmitted light is then collected by another lens and a fiber connected to a spectrometer. To obtain short integration times, and thus high temporal resolution, a spectrometer with fixed grating was chosen. A spectrum can then be acquired in a few milliseconds compared to minutes for conventional spectrometers based on moveable gratings.

In nanoplasmonic sensing one typically monitors temporal changes in the wavelength at maximum extinction (the peak position). As discussed in Chapter 3, the nanoplasmonic structure should have a high RI sensitivity combined with a narrow peak and a large peak height in order to provide large changes in extinction at specific wavelengths. The optical components should then be chosen so that these changes can be measured with as high precision as possible. First, the largest source of noise is typically shot noise, which is proportional to the square root of the intensity ( $I^{1/2}$ ). The signal is instead proportional to  $I$ , which means that the signal-to-noise ratio increases approximately as  $I^{1/2}$ . Hence, when the aim is to probe small changes in the detected signal one should strive for high intensities in terms of the number of photoelectrons generated in the detector per time unit. For measurements on large areas, as in the setup described here (spot size around 5 mm in diameter), the intensity of the collected light can easily be high. Therefore, despite its lower sensitivity compared with typical CCD-based detectors, a photo diode array (PDA) spectrometer was chosen, because of its higher well depth (high dynamic range).

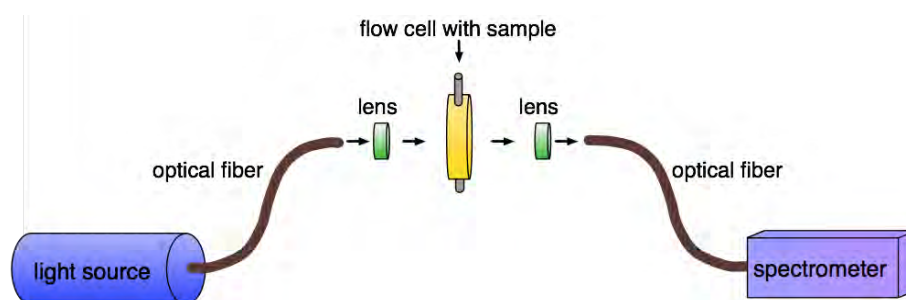


**Figure 5.4.** Schematic illustration of an extinction setup as used in this work. The sample is illuminated with collimated light from a white light source via an optical fiber and a collimating lens. The transmitted light is then coupled into a second fiber via another lens. A diode array spectrometer with a fixed grating collects the spectral information, which is sent to a computer for analysis.

---

### 5.2.2 Extinction spectroscopy on small areas

The possibility to perform experiments on small ( $\sim 10 \times 10 \mu\text{m}^2$ ) areas is valuable in many respects, not least for the development of multiplexed array-based sensing. In this work, extinction spectroscopy on small areas (microextinction spectroscopy) was used in the investigation of free-standing membranes with nanoplasmonic pores (Paper III).

Extinction measurements on small areas can be achieved by connecting a spectrometer to a conventional microscope. With respect to noise minimization, the same principles apply as for measurements on larger areas. However, for short acquisition times ( $\sim 10$  ms), the intensity (even when using high-intensity light sources) collected from a micrometer-sized spot is typically lower than what is required in order to work close to saturation (and hence utilize the full dynamic range) of a PDA detector. In this situation, a spectrometer based on a CCD array is preferable, because it has higher sensitivity and can generate more photoelectrons per time unit.

### 5.2.3 Data analysis – The centroid method

After choosing optical components to measure changes in optical extinction with as high precision as possible, it is time to discuss proper treatment of the data. Note that the spectrometer will not provide direct peak position values. The spectra merely provide information on the extinction at specific wavelengths. In order to find and track the peak position one can fit these values to a polynomial function. Peak maxima (and dip minima) are then found at wavelengths at which the derivative of this polynomial function is zero. An alternative to probe changes in the peak maximum is to monitor changes in the wavelength at the centre of mass of the peak (the centroid).<sup>160, 209</sup> Compared with the peak maximum, the centroid is often more stable and less susceptible to, for example, fluctuations in the light source. In turn, this results in a significant reduction in the temporal noise. Furthermore, if the peak shape does not change during measurement and if the area used to calculate the centroid is kept constant, shifts in peak and centroid positions are identical for a given shift in the plasmon resonance. As depicted in Fig. 5.5, the centroid  $\lambda_c$  of the area above  $E(\lambda_a)$  and between  $\lambda_a$  and  $\lambda_b$  can be calculated according to:<sup>160</sup>

$$\lambda_c = \frac{\int_{\lambda_a}^{\lambda_b} \lambda [E(\lambda) - E(\lambda_a)] d\lambda}{\int_{\lambda_a}^{\lambda_b} E(\lambda) - E(\lambda_a) d\lambda} \quad (5.3)$$

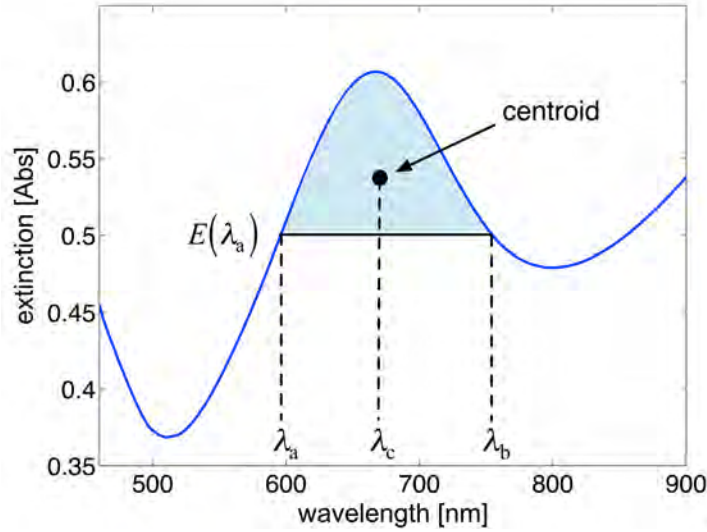


**Figure 5.5.** Illustration of the centroid method. The graph is an extinction spectrum of short-range ordered holes in a thin gold film.  $\lambda_c$  corresponds to the centroid of the shaded area.

The spectrometer collects information in every pixel, each of which corresponds to a small, yet discrete wavelength range. The integrals in Eq. 5.3 must therefore be converted to sums. This, in turn, may create step-like noise during temporal measurements whenever  $\lambda_a$  or  $\lambda_b$  changes value (in order to keep the area corresponding to the centroid constant). This can be circumvented by fitting the peak to a polynomial function ( $E(\lambda)=p_0+p_1\lambda+\dots+p_n\lambda^n$ ) at every time step. The integration can now be performed directly from the polynomial coefficients as:

$$\lambda_c = \frac{\int_{\lambda_a}^{\lambda_b} \lambda \sum_{i=0}^n [p_i \lambda^i - p_i \lambda_a^i] d\lambda}{\int_{\lambda_a}^{\lambda_b} \sum_{i=0}^n [p_i \lambda^i - p_i \lambda_a^i] d\lambda} \Rightarrow \quad (5.4)$$

$$\lambda_c = \frac{\sum_{i=0}^n \left[ \frac{p_i}{i+2} (\lambda_b^{i+2} - \lambda_a^{i+2}) - \frac{p_i}{2} \lambda_a^i (\lambda_b^2 - \lambda_a^2) \right]}{\sum_{i=0}^n \left[ \frac{p_i}{i+1} (\lambda_b^{i+1} - \lambda_a^{i+1}) - p_i \lambda_a^i (\lambda_b - \lambda_a) \right]} \quad (5.5)$$

In this work, changes in the peak position and in the centroid were typically monitored, calculated and plotted at the same time using custom-designed Matlab (The Mathworks) or LabView (National Instruments) programs.

---

### 5.3 The quartz crystal microbalance

The quartz crystal microbalance with dissipation (QCM-D) monitoring technique is a mechanical weighting device that is widely used for label-free biosensing.<sup>210</sup> In this work it was employed both as a complementary method to investigate and optimize surface modification protocols and in a combined nanoplasmonic and QCM-D setup (Paper II). Quartz is a piezoelectric material, which means that a quartz crystal will deform when exposed to an electric field. A thin AT-cut crystal will deform in shear mode and by applying an alternating potential over the crystal, for example, by the use of evaporated gold electrodes on both sides of the crystal, it can be forced into oscillation. At certain frequencies the crystal can oscillate more easily, resulting in an enhancement of the oscillation amplitude. These resonance frequencies are determined by the thickness of the crystal and therefore shift upon mass adsorption. The resonance frequencies can be measured in real-time, which has been employed for decades to monitor the film thickness increase during, for example, thermal evaporation or chemical vapor deposition.<sup>68</sup>

The extension of the QCM to measurements in fluids was enabled by new electric circuitry,<sup>211</sup> and the QCM is now one of the most commonly used weighting devices used for monitoring biomolecular surface reactions in real-time and in a label-free fashion. In contrast to optical techniques that are sensitive to changes in the refractive index, such as the SPR method or the nanoplasmonic sensors developed in this work, the QCM measures the mass that is coupled to the oscillation of the crystal. This means that, apart from the mass of adsorbed molecules, the liquid inside and hydrodynamically coupled between bound molecules is also sensed. Keller et al. utilized this to monitor the structural change during the formation of a lipid bilayer from adsorption and rupture of vesicles on a SiO<sub>2</sub> surface.<sup>212</sup> The difference in the temporal response compared with that of adsorption of vesicles that did not rupture was dramatic (see also Chapter 6). In addition to the resonance frequencies, the damping of the crystal oscillation provides information on the visco-elastic properties of bound molecules.<sup>13</sup> The damping is quantified as the dissipation, which also is useful in the investigation of structural changes, such as vesicle rupture on the sensor surface.<sup>212</sup> This is described in more detail in Chapter 6 for a combined nanoplasmonic and QCM-D setup developed in this work.

### 5.3.1 Theoretical description of the QCM

The resonance frequencies  $f_n$  at which a QCM crystal is easily excited into oscillation can be determined from (see Fig. 5.6):<sup>68</sup>

$$f_n = \frac{nv_q}{2t_q}, \quad n = 1, 3, 5 \dots \quad (5.6)$$

where  $t_q$  is the thickness of the crystal and  $v_q$  the speed of sound in the quartz material. There are resonance frequencies for every odd number of the overtone number  $n$ . For a 334  $\mu\text{m}$  thick crystal and using  $v_q=3340$  m/s, the fundamental frequency is 5 MHz. By introducing the density of the crystal  $\rho_q$ , the mass dependency becomes more apparent:\*

$$f_n = \frac{nv_q\rho_q}{2t_q\rho_q} = \frac{nv_q\rho_q}{2m_q} \quad (5.7)$$

Differentiation of Eq. 5.7 with respect to mass then yields:

$$df_n = -\frac{nv_q\rho_q}{2m_q^2} dm_q = -\frac{f_n}{m_q} dm_q \quad (5.8)$$

A small change in mass (per area),  $\Delta m$ , will thus result in a frequency shift  $\Delta f_n$  according to:

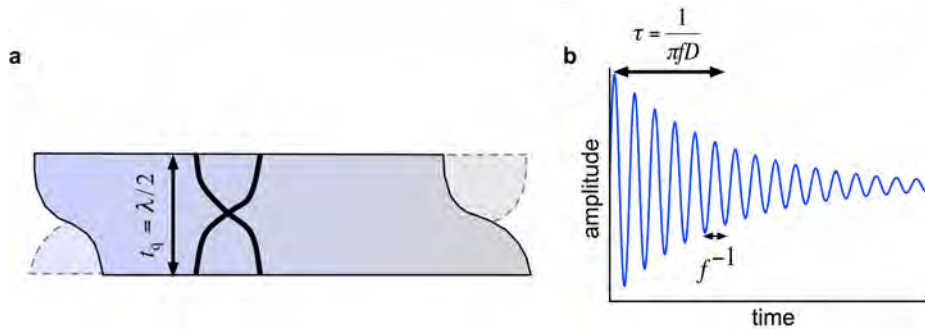


**Figure 5.6. (a)** Schematic illustration of a quartz crystal with thickness  $t_q$  and fundamental resonance wavelength  $\lambda$ . **(b)** Illustration of a decaying crystal oscillation from which both  $f$  and  $D$  are obtained.

\* Note that the term mass is in this discussion used to describe the mass of the crystal per unit area and hence, it is independent on the crystal diameter.

(5.9)

$$\Delta f_n = -\frac{f_n}{m_q} \Delta m = -Cn\Delta m$$

This relation is known as the Sauerbrey equation.<sup>213</sup> For 5 MHz crystals (as used in this work), the sensitivity constant  $C$  is  $17.7 \text{ ngcm}^{-2}\text{Hz}^{-1}$ .<sup>214</sup> Note that  $C$  is dependent on the mass of the crystal and, hence, the linearity between the frequency shift and mass adsorption is only a good approximation in the case of adsorbed masses that are much smaller than the total mass of the crystal. This is however normally not an issue in biosensing applications.

As mentioned above, the damping, or the dissipation  $D$  of the crystal provides information on the visco-elastic properties of the adsorbed biomolecular layer. One way of measuring the resonance frequency and the energy dissipation simultaneously is by exciting the crystal close to the resonance frequency and by monitoring the free oscillation decay after disconnection of the driving voltage (see Fig. 5.6b). The dissipation is then determined from:<sup>215</sup>

$$D = \frac{1}{\pi f \tau} \quad (5.10)$$

where  $\tau$  is the decay time constant, corresponding to the time it takes for the free oscillation amplitude to decrease by a factor  $e$ , where  $e$  is the base of the natural logarithm.

Note that the Sauerbrey equation considers a change in the mass of the crystal, which means that the adsorbed mass is treated as a rigid film that perfectly follows the oscillation of the crystal. This is not true, for example, for a crystal in contact with a viscous fluid. Instead  $\Delta f$  and  $\Delta D$  induced by a viscous fluid can be described by:<sup>216</sup>

$$\Delta f = -\frac{1}{2\pi t_q \rho_q} \sqrt{\pi f \rho_f \eta_f} \quad (5.11a)$$

$$\Delta D = \frac{1}{t_q \rho_q} \sqrt{\frac{\rho_f \eta_f}{\pi f}} \quad (5.11b)$$

where  $\rho_f$  and  $\eta_f$  are the density and the viscosity of the fluid, respectively. Furthermore, neither Eq. 5.9 (a rigid film) nor Eq. 5.11 (a viscous fluid) describes the situation of a non-rigid film that is adsorbed on a QCM crystal (e.g. a layer of lipid vesicles). In such situations, the adsorbed film must be represented by a visco-elastic description, where a Voigt-based representation has been found capable of reproducing the measured changes in  $f$  and  $D$  at multiple harmonics.<sup>73, 217</sup>

## **Chapter 6      Results and discussion**

The main results obtained during the work presented in this thesis are summarized in this chapter. The focus is put on discussing certain unique possibilities provided by nanoplasmonic sensors, in particular those based on short-range ordered nanoplasmonic holes.

### **6.1      Nanoplasmonic structural sensing – Papers I and II**

The plasmonic field of both conventional plasmonic sensors and nanoplasmonic sensors is strongest at the surface and decays rapidly away from the surface. However, one of the main differences between the two types of sensors is the difference in decay length. While the field of a typical conventional plasmonic sensor extends several hundred nanometers from the sensor surface, the decay length of nanoplasmonic sensors is often in the order of tens of nanometers or less. In Papers I and II we utilized the short decay length of short-range ordered nanoholes in thin metal films to study biomolecular structural changes on the sensor surface.

A molecule, with a refractive index that differs from the surrounding solution, that enters the plasmonic field will induce a shift in the plasmon resonance. This forms the base for using nanoplasmonics for RI-based sensing, as discussed in Chapters 3 and 4. The magnitude of the shift induced by the molecule is related to the square of the plasmonic field strength (i.e. the field intensity). A molecule that binds directly onto the surface will therefore induce a larger plasmonic shift compared with a molecule that binds or in other ways becomes located at a certain distance from the surface (e.g. a tethered molecule, see Fig. 6.1). As a result, not only the binding of molecules, but also the movement of molecules closer to or further away from the surface should result in shifts in the plasmon resonance. This suggests that it would in principle be possible to study structural changes that result in alterations in the RI distribution in the vicinity of the metal surface.

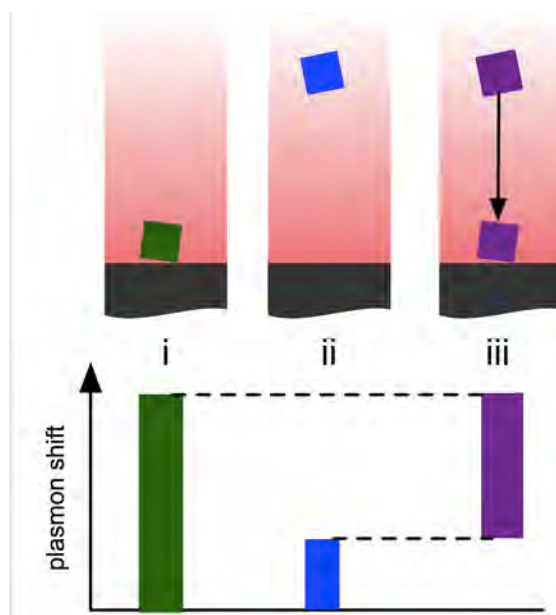


**Figure 6.1.** Schematic illustration of the principle behind nanoplasmonic structural sensing. The shaded areas depict the rapidly decaying plasmonic field. The left molecule (i) is close to the sensor surface and induces a larger shift in the plasmon resonance than the middle molecule (ii) that is further away from the surface. The movement between these two positions results in a plasmon shift corresponding to the difference between the two shifts, as illustrated for the molecule on the right (iii).

The concept of nanoplasmonic structural sensing was described in Paper I and further investigated in Paper II, by monitoring the formation of a SLB from adsorption and rupture of lipid vesicles on short-range ordered nanoplasmonic hole sensors (see Fig. 6.2). Rupture of lipid vesicles into SLBs could be achieved by coating the structure with a thin layer of  $\text{SiO}_x$ , due to the fact that rupture takes place on glass and  $\text{SiO}_x$ , but not on gold (see Chapter 2). The SLB formation was investigated in real-time by monitoring the temporal variation in the plasmon resonance, as shown in Fig. 6.3. The nanoplasmonic sensor structure was mounted in a flow cell that was filled with buffer. Lipid vesicles were injected into the flow cell at 0 min and subsequent adsorption to the surface induced local changes in RI resulting in a corresponding increase in the plasmon resonance (the plasmon resonance shift is denoted  $\Delta\lambda$  in Fig. 6.3). At around 5 min, the sensor response accelerated before it was finally saturated after around 10 min. The acceleration and corresponding kink in the curve is attributed to the rupture of vesicles, which results in the average lipid distribution moving closer to the sensor surface and into a stronger plasmonic field. The kink in the response is marked with a dashed circle in Fig. 6.3.

Note that, by using a small fraction of labeled lipids in the vesicles, the successful formation of a macroscopic SLB on the sensor surface could be verified separately by fluorescence-based microscopy, including FRAP. The SLB was shown to be fluid with a high lateral mobility. It was also concluded that the SLB followed the contour of the substrate in a similar manner to that depicted in Fig. 6.2. As expected, no kink in the sensor response curve was observed in situations when vesicle rupture did not occur. In subsequent work by the Van Duyne group, the concept of nanoplasmonic structural sensing also proved promising in a the study of reversible protein conformations.<sup>218</sup>

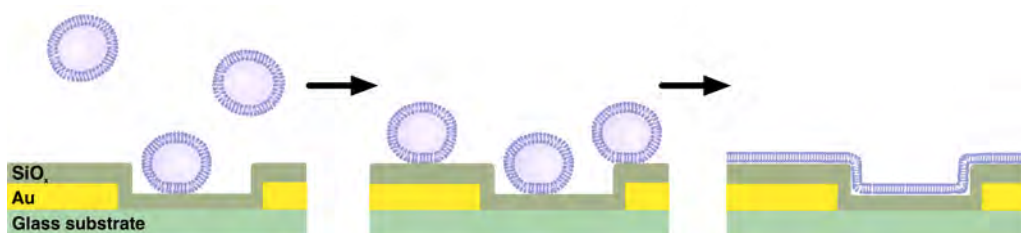


**Figure 6.2.** Schematic illustration of SLB formation from vesicles on a SiO<sub>x</sub>-coated nanoplasmonic hole surface.

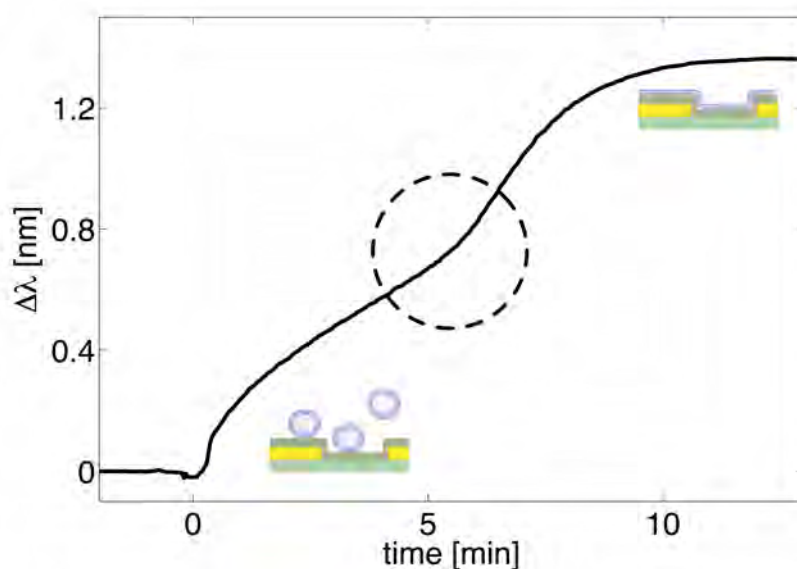


**Figure 6.3.** Temporal variation in the plasmon resonance during SLB formation on SiO<sub>x</sub>-coated short-range ordered nanoholes in a thin (30 nm) metal film. The kink at around 5 min (marked with the dashed circle) is attributed to vesicle rupture. An initial (at around 0 min) drop in peak shift due to a wavelength dependence on the light scattering of vesicles has been removed.

## 6.2 Combined nanoplasmonic and QCM-D sensing – Paper II

Short-range ordered nanoplasmonic holes and nanoplasmonic particles provide similar sensing capabilities. A fundamental difference between the two structures is that while particles are discrete entities, a perforated metal film is continuous and electrically conductive. This enables the latter to be used as a *nanoplasmonic electrode*. In Paper II this was utilized for combined nanoplasmonic and QCM-D measurements. A perforated nanoplasmonic hole film was used as the sensing electrode of a QCM crystal. By making a hole in the backside electrode, the nanoplasmonic response could be measured using conventional transmission spectroscopy as depicted schematically in Fig. 6.4.

The potential of the combined setup was investigated by the formation of a SLB from adsorption and rupture of lipid vesicles. As in the study presented in Paper I, the sensor surface was coated with a thin layer of  $\text{SiO}_x$  to facilitate SLB formation. In 1998, the Kasemo group showed that both the frequency and the dissipation of the QCM-D setup provide clear signatures for the rupture of lipid vesicles into a planar SLB,<sup>212</sup> as presented for the combined setup in Fig. 6.5a. The reason for the signature in the frequency response is that the crystal oscillation is affected not only by the mass of the lipids of the adsorbed and intact vesicles, but also by the liquid inside these vesicles. This leads to a relatively large decrease in the frequency upon initial vesicle adsorption. However, when the vesicles rupture (at around 5-6 min in Fig. 6.5a), the liquid inside them is released and no longer sensed by the QCM-D. The rupture

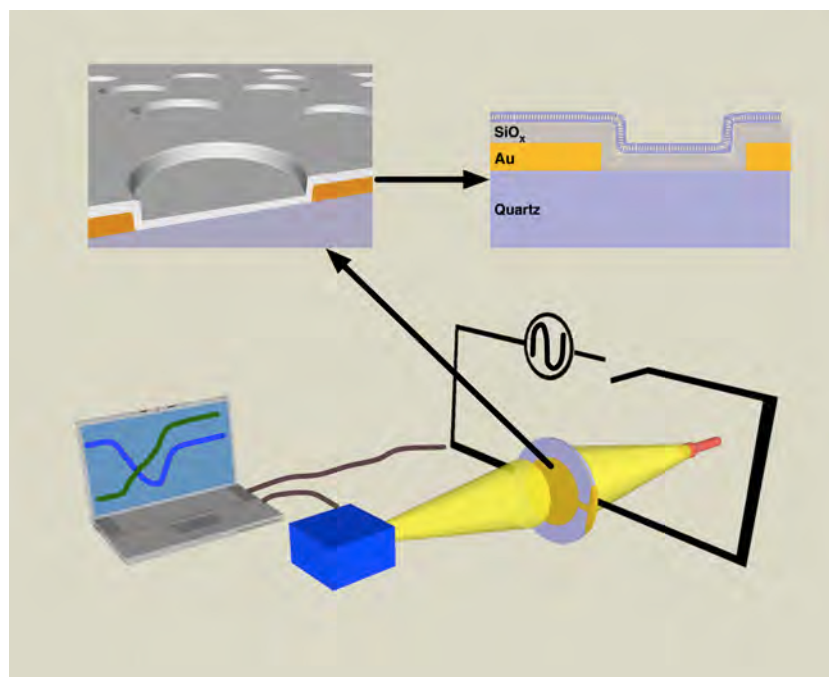


**Figure 6.4.** Schematic illustration of the combined sensor principle for simultaneous nanoplasmonic and QCM-D measurements on the same surface.

process therefore results in a decrease in the effective mass on the sensor and a corresponding increase in the frequency until saturation at around -25 Hz for a SLB on a crystal with resonance close to 5 MHz (normalized with the overtone number). The energy dissipation signal reflects the visco-elastic properties of the system. There is an increase in dissipation as bulky vesicles adsorb on the surface. During rupture, a more rigid layer is formed and the dissipation decreases to a relatively small value of around  $1 \times 10^{-6}$  for the final SLB.

In Figure 6.5b, the change in dissipation of the QCM crystal is plotted together with the nanoplasmonic response. A clear correlation in time can be observed between the two signatures for SLB formation. This verifies that the nanoplasmonic kinks observed in Paper I originated from vesicle rupture. Note also, that the nanoplasmonic response provides an estimate of the start of the vesicle rupture process as the time at which the curve starts to deviate from a typical binding curve (marked with a dashed arrow in Fig. 6.5b).

Apart from being suitable for studies of structural changes, the combined sensor setup was also shown to provide improved means to quantify the bound mass on the sensor surface. This exemplifies that the combination of two different sensor techniques, such as the one presented here, often provide more information about a reaction than the two techniques separately. The reason is mainly that the responses of different sensor methods have different origins. In this example, the nanoplasmonic response is due to local changes in the refractive index, while the QCM-D response corresponds to mass coupled to the oscillating crystal. Apart from nanoplasmonic sensing, the QCM-D technique has been combined with, for example, reflectometry<sup>219</sup> and SPR.<sup>214</sup>

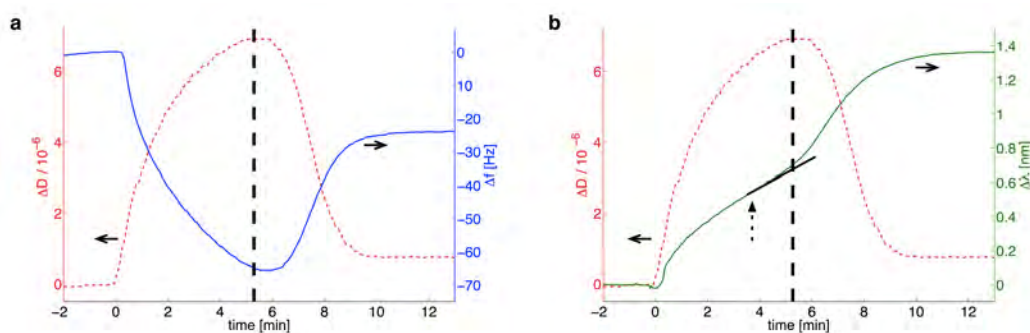


**Figure 6.5.** (a) Temporal variation of the dissipation  $\Delta D$  (dashed curve) and the frequency  $\Delta f/3$  (solid curve) at the 3rd overtone during SLB formation on the nanostructured surface. (b) Same as in (a), but instead showing the dissipation (dashed curve) and the plasmonic peak shift  $\Delta\lambda$  (solid curve). An initial (at around 0 min) drop in peak shift due to a wavelength dependence on the light scattering of vesicles has been removed. The vertical dashed lines in (a) and (b) are provided as visual aids and to demonstrate the temporal correlation between the turnover in the dissipation and the nanoplasmonic kink. The short black line and corresponding dashed arrow demonstrate the possibility of investigating the initiation of vesicle rupture from the kinky nanoplasmonic response.

### 6.3 Flow-through nanoplasmonic sensing – Paper III

The previous section described how a metallic hole film can be used as a nanoplasmonic electrode. In Paper III, the continuity of a perforated metal film was instead used to create *nanoplasmonic pores*, designed to penetrate the whole substrate (see Fig. 6.6). Such a system may find numerous interesting applications as reflected on in Chapter 7. This study was focused on investigating the possibility of using the structure to improve mass transport in biosensing applications.

Note that even if a biosensor could provide single-molecule resolution, the molecules would only be detected if they interact with the surface. As discussed in detail in Chapter 1, the mass transport is typically slow under stagnant conditions, but can be improved by letting the sample solution flow parallel to the sensor surface. In particular, it was reasoned that the channel dimensions could be decreased in order to simultaneously decrease the sensor response time and the amount of sample needed for detection.

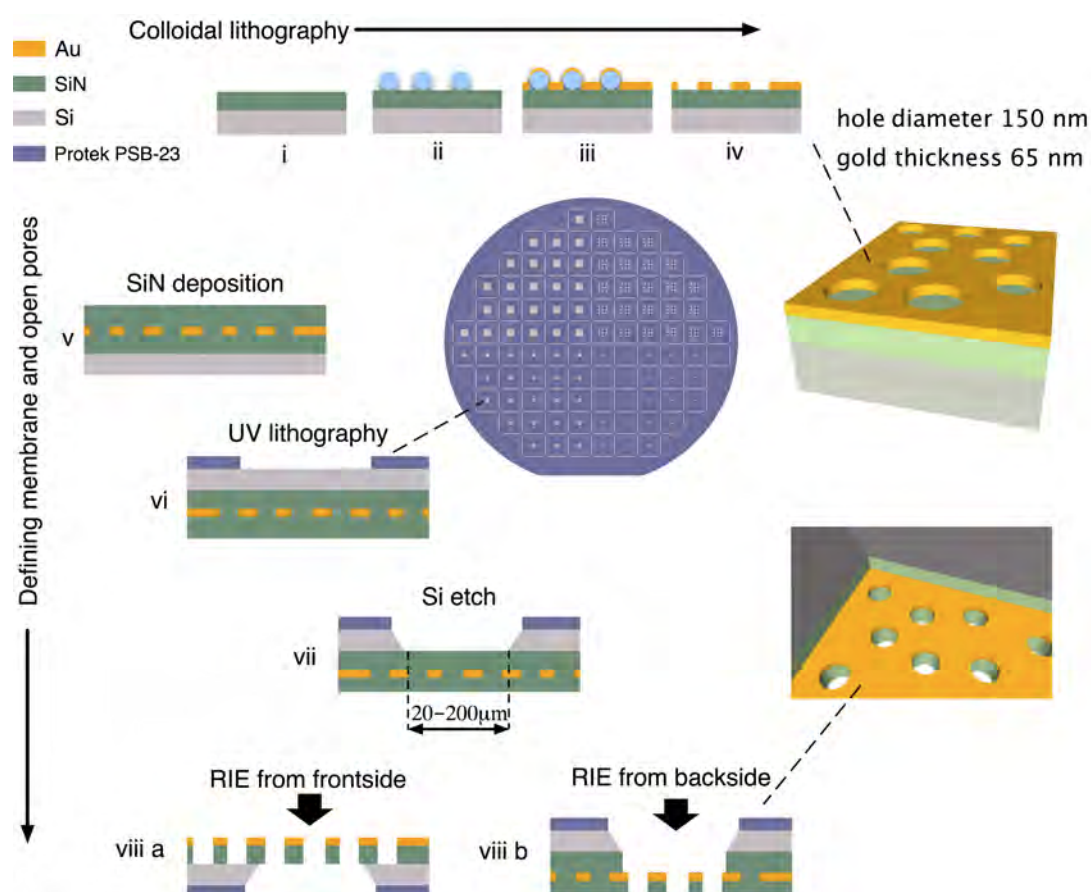


**Figure 6.6.** Schematic illustration of the protocol for the fabrication of short-range ordered nanoplasmonic pores. A detailed description can be found in Paper III.

Periodic arrays of plasmonic pores were investigated by Eftekhari et al.<sup>220</sup> and Yanik et al.<sup>221</sup> In Paper III, the concept of plasmonic pores was for the first time explored for short-range ordered arrays of nanopores. As illustrated in Fig. 6.6, a fully parallel fabrication scheme was developed that allowed the simultaneous production of around 100 sensor chips with one or more nanoplasmonic membranes or alternatively, over 1000 membranes on a single wafer. The method is based on colloidal lithography and standard microfabrication steps, such as photolithography and reactive ion etching (RIE), as indicated in Fig. 6.6 and described in detail in Paper III.

The fabrication protocol was successfully used to fabricate membranes in gold and SiN perforated with pores possessing nanoplasmonic properties (Fig. 6.7a and b). A materials-specific surface modification scheme, first established using the QCM-D technique, was used to enable specific binding of NeutrAvidin to the gold regions, while efficiently suppressing non-specific adsorption to the SiN (see Fig. 6.7c). NeutrAvidin was then allowed to flow through the pores (from the SiN side) and bind to the gold, resulting in the solid trace in Fig. 6.7d. A comparison with the same reaction under stagnant conditions (for non-through-going nanoplasmonic holes, dashed curve in Fig. 6.7d) shows that the binding rate was more than one order of magnitude higher for the flow-through case. This shows that the concept can provide efficient transport of molecules to the sensor surface.

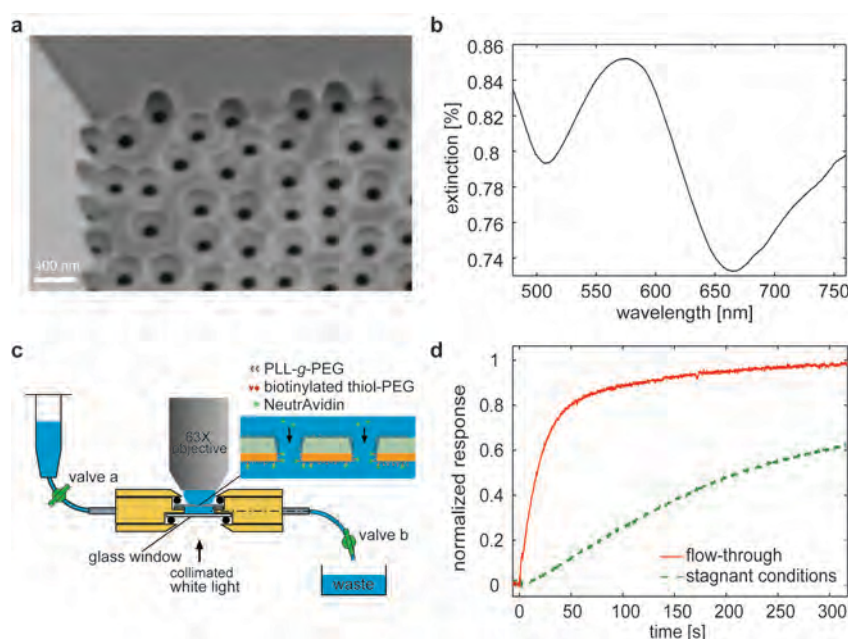


**Figure 6.7.** Nanoplasmonic flow-through sensing. **(a)** SEM image of the backside of a corner of a nanoplasmonic membrane fabricated by RIE from the frontside. **(b)** Extinction spectrum in air of a sample similar to the one in (a). **(c)** Schematic illustration of the relatively simple experimental setup and of the materials-specific surface modification used. **(d)** The solid trace shows the specific binding of NeutrAvidin, flowing through the pores and binding specifically to the gold. The dashed curve shows the same reaction, but under stagnant conditions for a sample with nanoplasmonic wells. Both curves are normalized to the respective final saturated values.

## 6.4 Improving performance by directed binding – Paper IV

In Papers I and II, the tight confinement of the plasmonic field (and corresponding sensitivity) to the sensor surface enabled the realization of nanoplasmonic structural sensing. The sensitivity of nanosensors is often also confined laterally on the sensor surface. This provides a means of improving the binding rate for mass transport limited reactions.

The concept is illustrated in Fig. 6.8. For mass transport limited binding, a certain number of molecules per surface area will have reached the sensor surface after a given time. In a conventional situation, these molecules bind in a uniform way over the sensor surface (Fig. 6.8a and c). Alternatively, the molecules that reach the surface can be directed to bind preferentially on small bioactive areas (Fig. 6.8b and d), while adsorption on surrounding areas is suppressed. In the latter case, the *local* coverage on areas that promote binding will (at a given time) be higher than for uniform binding.

For a macroscopic sensor, such as a conventional SPR system, uniform and directed binding (Fig. 6.8a and b) will provide similar sensor signals. The reason is that the sensor response will in this case reflect the average surface coverage, which, in turn, will be approximately the same for the two situations.

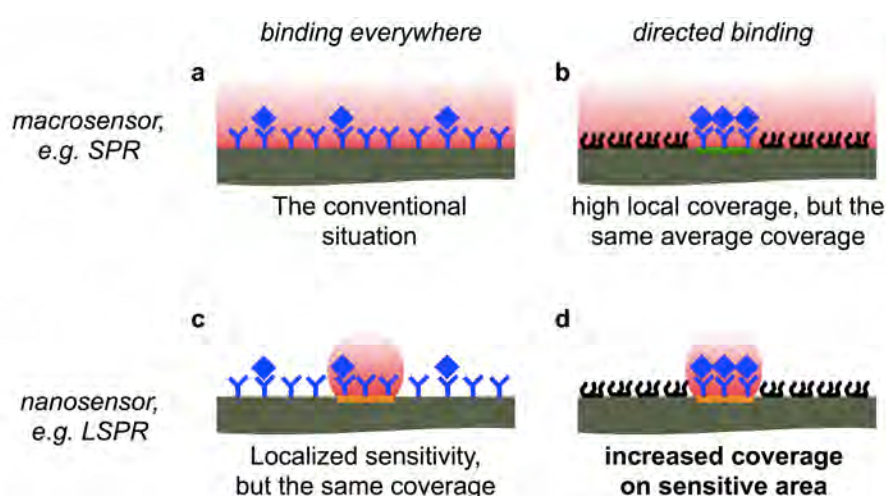


**Figure 6.8.** The concept of improving the uptake rate by directed binding to high-sensitivity regions (the shaded regions depicts the sensitivity). **(a)** The conventional situation of binding everywhere on a macroscale sensor surface. **(b)** Directed binding to nanoscale regions on a macroscale sensor will increase the local concentration of bound mass, but the average coverage on the sensor surface will be the same as in (a). **(c)** Binding everywhere on a nanoscale sensor will result in the same coverage in the sensitive region as for uniform binding on a macroscale sensor (a). **(d)** This is the most interesting situation. By directing the binding to the sensitive part of a nanosensor, the local coverage can be increased. In contrast to (b), the average coverage in the sensitive region is improved.

The situation is different if the sensitivity is localized to small regions, as in the case of typical nanosensors (see Fig. 6.8c and d). If binding is controlled to occur only in the high-sensitivity regions (Fig. 6.8d), a larger fraction of all molecules that reach the sensor surface will contribute to the sensor signal compared with the situation of uniform binding (Fig. 6.8c). This leads to a more rapid increase in the *effective* surface coverage.

In Paper IV, a short-range ordered nanoplasmonic hole sensor (see Fig. 6.9) was used to investigate whether directed binding to high-sensitivity regions can decrease the sensor response time for mass transport limited binding reactions. Both the bottom of and regions between the holes consisted of  $\text{TiO}_2$ , while gold was exposed on the sidewalls of the holes. Using materials-specific surface modifications based on PLL-g-PEG and thiolPEG with or without bioactive end groups, NeutrAvidin molecules could be controlled to bind (i) everywhere, (ii) nowhere or (iii) preferentially to any of the two materials. Results from a typical experiment are shown in Fig 6.9. The bottom curve corresponds to binding everywhere while the upper curve shows the situation when binding is directed to the walls of the holes only (both curves were normalized using the bulk RI sensitivity of the individual samples). It is clear that directed binding to the highly sensitive gold walls provides a significantly faster increase in the sensor response. This indicates that the local surface coverage in the sensitive plasmonic field increases faster in this situation compared with the case when binding is allowed everywhere. Furthermore, finite element simulations revealed that the binding process is not uniform, but can, for example, be significantly faster close to borders between binding and non-binding regions. This is particularly interesting since the plasmonic field is also non-uniform and typically highest close to metal edges. Insights into how to control the detailed binding rate and the plasmonic field distribution are likely to lead to further improvements of this concept.

It is important to note that binding reactions at low concentrations are often mass transport limited and slow (see Chapter 1). In fact, the binding rate can be the limiting parameter with respect to the lowest concentration that can be detected. This manifests the promise of the concept (as well as the previous concept of flow-through sensing) and highlights another unique possibility with nanoscale sensors.

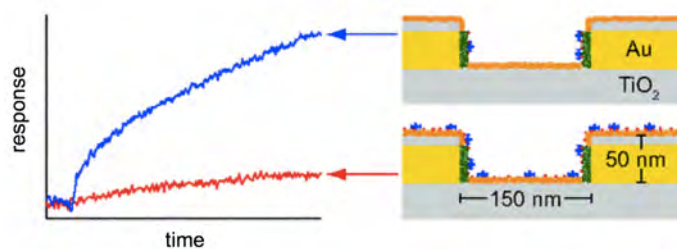


**Figure 6.9.** The upper curve corresponds to directed binding to the sidewalls of the holes (top schematic illustration) and the lower curve to binding everywhere (lower schematic illustration). 2 nM concentration of NeutrAvidin was used in both cases. More details on the results can be found in Paper IV.

## 6.5 Nanoplasmonic sensing with on-chip detection – Paper V

Simplicity has been a keyword in many aspects of this work. Perhaps surprisingly to some, this was not to make it easier for me and my colleagues to do the work, but with future applications in mind. The nanoplasmonic structures have been fabricated with simple, scalable and low-cost methods. Moreover, the reason for the choice of nanoplasmonics as the biosensing concept was partly to eliminate the need for complicated optics. The basic components of a typical nanoplasmonic sensor setup (see Chapter 5) are a light source and a spectrometer. In the work presented in Paper V, we eliminated the need for the relatively bulky and costly spectrometer by working at one wavelength only and directly converting the optical signal into an electrical signal on the sensor chip.

The concept is based on nanoplasmonic gold disks fabricated on a chip with an array of photosensitive p-n junctions (see Fig. 6.10a). These photovoltaic diodes convert light transmitted by the LSPR structure into an electrical signal that will be proportional to the intensity of the transmitted light. In turn, by working at a wavelength where the slope of the peak is high (Fig. 6.10b), the transmitted intensity (and hence, also the photocurrent) will be highly sensitive to changes in the plasmon resonance. A biomolecular binding reaction could then be monitored through changes in the photocurrent (Fig. 6.10c).

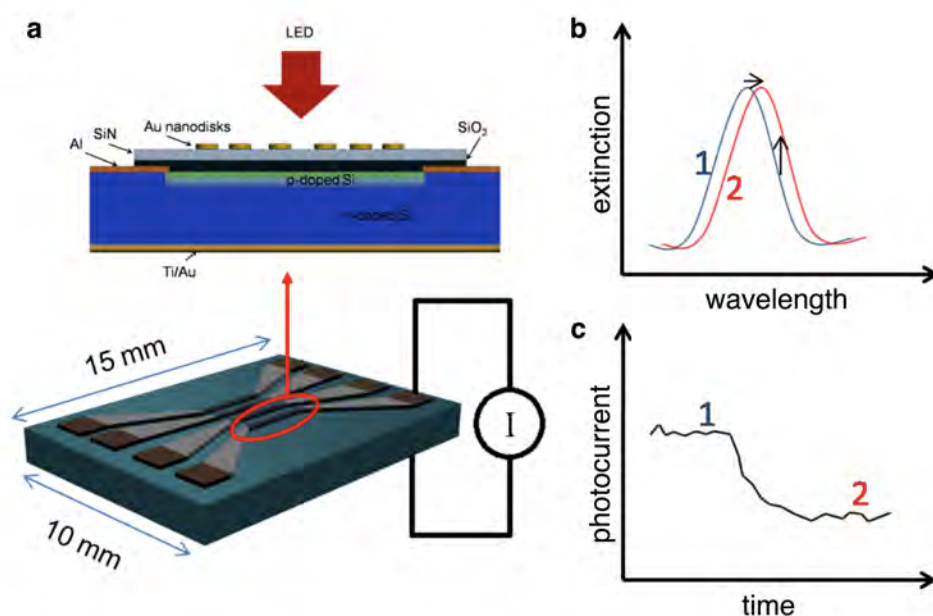


**Figure 6.10.** Illustration of the concept of on-chip detection. **(a)** The sensor design. Gold disks were fabricated using hole-mask colloidal lithography on an array of photoactive diodes. **(b)** Changes in peak position result in changes in the extinction (and transmission) at wavelengths where the slope of the peak is high. **(c)** Changes in the plasmon resonance, as induced by a biomolecular binding reaction, result in changes in the transmission, which in turn, modulates the photocurrent output. Note that the curves in (b) and (c) are only illustrations.

The gold disk dimensions were optimized on test samples with respect to the largest absolute change in transmission upon a small change in the surrounding RI. For the same peak RI sensitivity, a narrow peak with high magnitude will provide larger changes in the transmission than a broad peak with low magnitude (see also Section 3.3.3). Disks with a diameter of 110 nm and a height of 20 nm were chosen as the optimum structure for use on the photodiode chips. The plasmonic peak could be observed in the electrically acquired spectra by measuring the photocurrent at different wavelengths using the signals from a non-patterned photodiode as reference (see Paper V). The photocurrent was measured at a small wavelength interval around 780 nm using a light emitting diode (LED) and found to vary linearly with small changes in RI (Fig. 6.11a). Finally, specific binding of protein to the gold disks was successfully monitored through changes in the photocurrent output (Fig. 6.11b). To eliminate noise and drift, a built-in diode without plasmonic particles was used as reference.

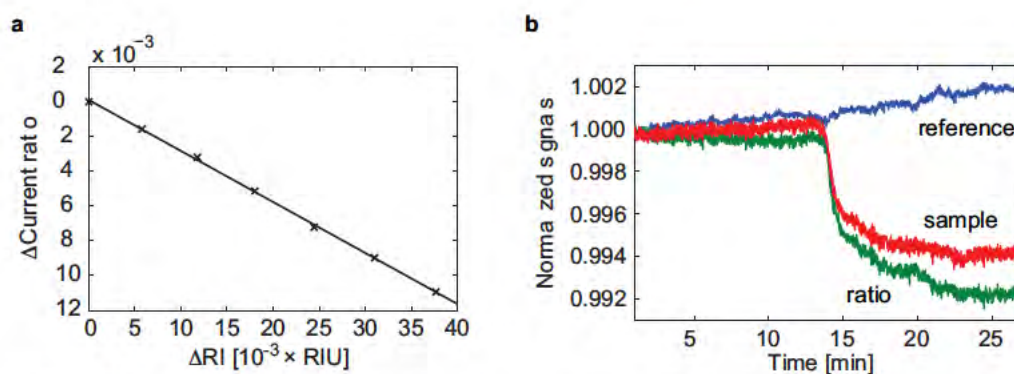


**Figure 6.11.** (a) Changes in the photocurrent ratio (sample/reference) versus changes in bulk RI (using different concentrations of glycerol in water). (b) Temporal variation in the normalized photocurrent outputs during specific binding of protein to the gold nanodisks for a non-patterned diode (reference), a diode with plasmonic particles (sample), and the ratio between these signals. The protein was added at around 13 min.



## Chapter 7      Conclusions, reflections and outlook

Finally, I will summarize and reflect on possible extensions of the concepts presented in this thesis. The focus has been to investigate various plasmonic sensor systems and to utilize features specific to certain structures to address challenges in bioanalytical sensing. In particular, unique possibilities provided by short-range ordered nanoholes in thin gold films have been explored. Apart from providing excellent nanoplasmonic sensing capabilities, this structure is continuous and electrically conductive. It could therefore be used as one of the electrodes in a QCM sensor, enabling combined nanoplasmonic and QCM measurements. I would like to stress that (i) other continuous structures (e.g. periodic hole arrays, nanoslit arrays, etc.) could potentially also be used as plasmonic electrodes in a similar manner and (ii) the use of nanoplasmonic electrodes is not restricted to the excitation and read-out of QCM crystals, but could also be used in other contexts, such as to enable combined nanoplasmonic and electrochemical sensing.

Sensors based on discrete LSPR structures and short-range ordered holes in thin metal films possess relatively short sensing depths (typically tens of nanometers). In this work, it was shown that a short decay length provides a unique means to probe structural changes on the sensor surface, exemplified by the formation of a supported lipid bilayer from the adsorption and subsequent rupture of lipid vesicles. Structural changes, in turn, are common in many biomolecular processes. For example, the binding between an analyte and a receptor is often accompanied by a conformational change of the combined system. The possibility to study such changes with nanoplasmonics may be particularly valuable in the investigation of drug molecules binding to drug targets on a sensor surface. While drug molecules are small (typically below 500 Da) and hard to detect directly, the binding often induces concurrent conformational changes in the drug target that may be used as an indirect measure of the binding reaction.<sup>16, 218, 222</sup>

The fact that the majority of drugs target cell membrane receptors makes sensor methods compatible with lipid bilayer membranes particularly valuable. In fact, the decision to study vesicle rupture on nanoplasmonic structures was not only based on the structural change that is involved in that process, but also with the aim to develop a nanoplasmonic sensor suitable for the investigation of reactions associated with cell membranes. Using SLBs modified with lipid-anchored membrane receptors, specific protein binding could be monitored through the nanoplasmonic response with a competitive signal-to-noise ratio (Papers I and II). One of our current objectives is to extend the concept of nanoplasmonic sensing of artificial cell membranes to the investigation of not

---

only binding to, but also transport through lipid bilayers. An interesting platform in this respect could be single lipid vesicles immobilized at the bottom of nanoplasmonic holes.<sup>80</sup> Molecular transport in and out of the vesicles may potentially be probed by monitoring changes in RI inside the vesicles, as recently performed successfully using conventional SPR.<sup>223, 224</sup>

Another potential concept for the investigation of membrane transport is lipid bilayers that span nanoplasmonic holes or pores. In a recent report by us,<sup>225</sup> we presented steps towards this goal by demonstrating that SLBs can be made to span SiO<sub>2</sub> nanowells if driven over a hole surface using the shear forces of a bulk flow in a microfluidic channel. Current efforts focus on combining this method with nanoplasmonic platforms similar to those presented in this thesis. In particular, it would be valuable to form membranes over nanoplasmonic through-going pores. While solid-state nanopores are commonly used for electrical measurements of transport through lipid bilayers,<sup>79, 226, 227</sup> the extension to solid-state nanoplasmonic pores could enable combined nanoplasmonic and electrical investigation of cell membrane transport. Note also that solid-state nanopores are not restricted to be used in combination with lipid bilayers, but are also commonly employed to measure translocation of DNA<sup>228</sup> and have, for example, been used to study unzipping of DNA molecules,<sup>229</sup> to perform force measurements of DNA<sup>230</sup> and to investigate DNA and protein complexes.<sup>231</sup> The combination of electrical and nanoplasmonic read-out may also be valuable for such applications.

The nanoplasmonic pores developed in this work were used primarily for flow-through sensing, which was found to be promising for (i) improvement of sensor response times, (ii) decrease in required sample volumes and (iii) increase in capture efficiency compared with typical microfluidic systems. In some applications, such as the detection of virus in drinking water, it may be valuable to be able to probe larger sample volumes. However, the volumetric throughput that is possible to achieve using a nanochannel is typically lower than that provided by a microfluidic channel. In this respect it is interesting that the concept presented in this work provides a two-dimensional array of nanochannels that can be used in parallel. In this way, the system could act as a filter with plasmonic sensor elements integrated in the pores. Furthermore, the concept of nanoplasmonic pores could potentially be combined with the use of electric fields to accumulate target molecules at the site of detection.<sup>43, 232, 233</sup>

Directed binding to high-sensitivity regions could also be used to decrease sensor response times, by enabling the local surface coverage in nanoscale regions to increase more rapidly compared with the situation when binding is also allowed on non-sensitive regions. The principle is generic and could be applied to other nanosensor methods, including plasmonic systems apart from short-range ordered nanoholes as well as nanowire field-effect devices<sup>21</sup> or nanocantilevers,<sup>26</sup> under the assumption that the binding can be controlled to occur locally in high-sensitivity regions for such systems.

The fact that the concept of directed binding is passive, in the sense that it does not rely on fluidic handling, makes it particularly promising with respect

to use in simple devices. In turn, one of the main strengths of nanoplasmonic sensing is that it can be made simple, both with respect to fabrication and instrumentation. Compared with conventional setups, nanoplasmonic sensing was in this work simplified by the integration of the opto-electrical conversion directly on the sensor chip. In future work, the performance can likely be improved by the use of multiple LEDs at different emission wavelengths together with photodiodes that are sensitive in different wavelength regions. This makes the combination of the concept with standard color CCD arrays highly interesting. I believe such systems have great potential to be used for simple sensing in an array-based format. Further, a spacer layer between the sensor structure and the detector array could enable the use of low-cost consumable sensor chips, while the detector and light sources could be reused.

The sensing concepts presented in this thesis are all based on the sensitivity of plasmon resonances to the refractive index of the surrounding environment. It should be mentioned that the strong electromagnetic fields associated with metal nanostructures can also be beneficial in other contexts. For example, the evanescent near-field inside a nanohole in an aluminum film (a zero-mode waveguide) can be used to excite fluorescent molecules locally inside the holes.<sup>234</sup> This platform has enabled fluorescence correlation spectroscopy<sup>11</sup> to be performed in extremely small observation volumes and was, for example, used to study lipid diffusion in cell membranes.<sup>235</sup> Moreover, the strong electromagnetic fields of nanoplasmonic structures can serve to enhance signals that correspond to intrinsic properties of the biomolecules themselves. Examples of promising concepts are surface-enhanced Raman spectroscopy (SERS)<sup>95</sup> and surface-enhanced infrared absorption (SEIRA) spectroscopy.<sup>236</sup> These methods have in common that they can provide chemical information and thereby molecular identification of bound species. I believe the concepts presented in this thesis, especially the nanoplasmonic electrodes and the nanoplasmonic pores, could be valuable also in combination with these methods.

In this outlook section I have reflected on some of the extensions of the work presented in this thesis that I think are particularly promising. Note that the potential applications that have been discussed are highly diverse, ranging from the investigation of molecular transport through artificial cell membranes, to the development of hand-held diagnostic devices. In turn, I think the diversity of potential applications directly reflects the large variation in the possibilities provided by different nanoplasmonic sensors. The large variety of nanoplasmonic systems provides the great opportunity to design and optimize a sensor for a given task. I think this is one of the main strengths of nanoplasmonic sensing and that this will result in numerous important applications in the future.



## Acknowledgements

The work presented in this thesis was realized thanks to a large number of people to whom I would like to express my gratitude. In particular I would like to acknowledge my:

- **supervisor:** Many thanks go to my supervisor Professor Fredrik Höök, who have taught me the most over these years, not least about the academic world, and who has always been available and happy to discuss ideas, results, papers, etc.
- **co-supervisors:** I would like to thank Professor Jonas Tegenfeldt, a never-ending source of ideas and inspiration and Professor Mikael Käll for valuable input on both scientific questions and future plans.
- **co-authors:** First a big thanks to all co-authors! Extra credits go to Andreas Dahlin, who first dragged me down into the world of plasmonic nanoholes, to Peter Jönsson, who has been involved in many of the projects presented in this thesis and, to Laurent Feuz and Francesco Mazzotta, my more recent companions in the search for the ultimate plasmonic sensor systems.
- **colleagues:** Many thanks to all office mates, coffee breakers and after workers, both at Lund University during the first years of this work, and at Chalmers the final years. You have made it very easy to enjoy work!
- **collaborators:** Special thanks to the crew at Queen's University in Belfast and to Stefan Löfås and Fredrik Mattinson at GE Healthcare Biosciences in Uppsala.
- **funding:** A large number of sources have enabled this work to be performed and presented at various conferences. Special thanks again to GE Healthcare Biosciences and to St Jude Medical for their contributions.
- **opponent:** I would like to thank Professor Harold Craighead for accepting to be the opponent of this thesis.
- **family and friends:** Special thanks to Malin for all your support and love.



## Populärvetenskaplig sammanfattning

Bioanalytiska sensorer är instrument som används för att studera interaktioner mellan olika biomolekyler, framför allt för detektion och/eller bestämning av koncentrationen av en specifik biomolekyl (protein, virus etc.) i en provlösning (till exempel i ett blodprov). Det gör biosensorer till oerhört viktiga hjälpmedel inom en rad olika områden, såsom läkemedelsutveckling, medicinsk diagnostik, analys av mat och dricksvatten mm.

Den här avhandlingen behandlar utveckling och användning av bioanalytiska sensorer baserade på nanostrukturerat guld, det vill säga guldstrukturer som är ungefär 1000 gånger mindre än vidden på ett hårstrå. Medan de flesta är vana vid att se guld som lätt gulaktigt (det vi menar med guldfärgat), skimrar nanoguld istället i specifika färger. Sedan urminnes tider har det här fenomenet använts för att färga glas, genom att bädda in nanopartiklar av guld och andra metaller i glaset. Användandet av fenomenet för bioanalytisk sensing är baserat på att en guldnanostrukturens färg är beroende av vad som finns i den närmsta omgivningen (omgivningens brytningsindex). En förändring i omgivningens brytningsindex, till exempel genom inbindning av biomolekyler till strukturen, resulterar i ett färgskift. Det gör det möjligt att studera den här typen av inbindningsprocesser genom att helt enkelt mäta förändringar i guldstrukturens färg. Sensorer som baseras på det här fenomenet kallas nanoplasmonsensorer och i det här arbetet har utmaningar inom området för biosensing adresserats genom att utveckla nya koncept och utforska unika möjligheter med sådana sensorer och framför allt med de som är baserade på tunna guldfilmer perforerade med nanohål.

De primära resultaten från arbetet inkluderar (i) demonstration av ett nytt sätt att mäta biomolekylära strukturella förändringar, (ii) användning av en guldnanohålfilm som elektrod för nanoplasmonsensing kombinerat med en annan sensorteknik baserad på en oscillerande piezoelektrisk kvartskristall (QCM), (iii) utveckling och användning av nanoplasmonsensorer som är kompatibla med studier av artificiella cellmembran, (iv) utveckling av två olika metoder att öka inbindningshastigheten till sensorytan och därmed en minskning av tiden för detektion och slutligen (v) integrering av elektrisk detektion direkt på sensorchipet som ett steg mot små, billiga och användarvänliga instrument för användning hemma hos patienten, på flygplatser, i utvecklingsländer osv.



## References

- (1) Clark, L. C.; Lyons, C. *Annals of the New York Academy of Sciences*. **1962**, *102*, 29-&. Electrode systems for continuous monitoring in cardiovascular surgery
- (2) Lockhart, D. J.; Winzeler, E. A. *Nature*. **2000**, *405*, 827-836. Genomics, gene expression and DNA arrays
- (3) Lequin, R. M. *Clinical Chemistry*. **2005**, *51*, 2415-2418. Enzyme Immunoassay (EIA)/Enzyme-Linked Immunosorbent Assay (ELISA)
- (4) Michalet, X.; Kapanidis, A. N.; Laurence, T.; Pinaud, F.; Doose, S.; Pflughoeft, M.; Weiss, S. *Annual Review of Biophysics and Biomolecular Structure*. **2003**, *32*, 161-182. The power and prospects of fluorescence microscopies and spectroscopies
- (5) Webb, S. E. D.; Roberts, S. K.; Needham, S. R.; Tynan, C. J.; Rolfe, D. J.; Winn, M. D.; Clarke, D. T.; Barraclough, R.; Martin-Fernandez, M. L. *Biophysical Journal*. **2008**, *94*, 803-819. Single-Molecule Imaging and Fluorescence Lifetime Imaging Microscopy Show Different Structures for High- and Low-Affinity Epidermal Growth Factor Receptors in A431 Cells
- (6) Axelrod, D.; Koppel, D. E.; Schlessinger, J.; Elson, E.; Webb, W. W. *Biophysical Journal*. **1976**, *16*, 1055-1069. Mobility measurement by analysis of fluorescence photobleaching recovery kinetics
- (7) Brian, A. A.; McConnell, H. M. *Proceedings of the National Academy of Sciences of the United States of America*. **1984**, *81*, 6159-6163. Allogeneic Stimulation of Cytotoxic T Cells by Supported Planar Membranes
- (8) Patel, A. R.; Frank, C. W. *Langmuir*. **2006**, *22*, 7587-7599. Quantitative analysis of tethered vesicle assemblies by quartz crystal microbalance with dissipation monitoring: Binding dynamics and bound water content
- (9) Jönsson, P.; Jonsson, M. P.; Tegenfeldt, J. O.; Höök, F. *Biophysical Journal*. **2008**, *95*, 5334-5348. A Method Improving the Accuracy of Fluorescence Recovery after Photobleaching Analysis
- (10) Bockmann, R. A.; Hac, A.; Heimbürg, T.; Grubmüller, H. *Biophysical Journal*. **2003**, *85*, 1647-1655. Effect of sodium chloride on a lipid bilayer
- (11) Magde, D.; Webb, W. W.; Elson, E. *Physical Review Letters*. **1972**, *29*, 705-708. Thermodynamic fluctuations in a reacting system - Measurement by fluorescence correlation spectroscopy
- (12) Grieshaber, D.; MacKenzie, R.; Vörös, J.; Reimhult, E. *Sensors*. **2008**, *8*, 1400-1458. Electrochemical Biosensors - Sensor Principles and Architectures

- 
- (13) Rodahl, M.; Hook, F.; Krozer, A.; Brzezinski, P.; Kasemo, B. *Review of Scientific Instruments*. **1995**, *66*, 3924-3930. Quartz crystal microbalance setup for frequency and Q-factor measurements in gaseous and liquid environments
- (14) Liedberg, B.; Nylander, C.; Lundstrom, I. *Sensors and Actuators*. **1983**, *4*, 299-304. Surface-Plasmon Resonance for Gas-Detection and Biosensing
- (15) Arwin, H. *Sensors and Actuators A: Physical*. **2001**, *92*, 43-51. Is ellipsometry suitable for sensor applications?
- (16) Swann, M. J.; Peel, L. L.; Carrington, S.; Freeman, N. J. *Analytical Biochemistry*. **2004**, *329*, 190-198. Dual-polarization interferometry: an analytical technique to measure changes in protein structure in real time, to determine the stoichiometry of binding events, and to differentiate between specific and nonspecific interactions
- (17) Voros, J.; Ramsden, J. J.; Csucs, G.; Szendro, I.; De Paul, S. M.; Textor, M.; Spencer, N. D. *Biomaterials*. **2002**, *23*, 3699-3710. Optical grating coupler biosensors
- (18) Armani, A. M.; Kulkarni, R. P.; Fraser, S. E.; Flagan, R. C.; Vahala, K. J. *Science*. **2007**, *317*, 783-787. Label-Free, Single-Molecule Detection with Optical Microcavities
- (19) Bornhop, D. J.; Latham, J. C.; Kussrow, A.; Markov, D. A.; Jones, R. D.; Sorensen, H. S. *Science*. **2007**, *317*, 1732-1736. Free-solution, label-free molecular interactions studied by back-scattering interferometry
- (20) Endo, T.; Kerman, K.; Nagatani, N.; Hiepa, H. M.; Kim, D.-K.; Yonezawa, Y.; Nakano, K.; Tamiya, E. *Analytical Chemistry*. **2006**, *78*, 6465-6475. Multiple Label-Free Detection of Antigen-Antibody Reaction Using Localized Surface Plasmon Resonance-Based Core-Shell Structured Nanoparticle Layer Nanochip
- (21) Zheng, G. F.; Patolsky, F.; Cui, Y.; Wang, W. U.; Lieber, C. M. *Nature Biotechnology*. **2005**, *23*, 1294-1301. Multiplexed electrical detection of cancer markers with nanowire sensor arrays
- (22) Cui, Y.; Wei, Q. Q.; Park, H. K.; Lieber, C. M. *Science*. **2001**, *293*, 1289-1292. Nanowire nanosensors for highly sensitive and selective detection of biological and chemical species
- (23) Ziegler, C. *Analytical and Bioanalytical Chemistry*. **2004**, *379*, 946-959. Cantilever-based biosensors
- (24) Waggoner, P. S.; Craighead, H. G. *Lab on a Chip*. **2007**, *7*, 1238-1255. Micro- and nanomechanical sensors for environmental, chemical, and biological detection
- (25) Alvarez, M.; Lechuga, L. M. *Analyst*. **2010**, *135*, 827-836. Microcantilever-based platforms as biosensing tools
- (26) Hwang, K. S.; Lee, S. M.; Kim, S. K.; Lee, J. H.; Kim, T. S. *Annual Review of Analytical Chemistry*. **2009**, *2*, 77-98. Micro- and Nanocantilever Devices and Systems for Biomolecule Detection

- (27) Barton, R. A.; Ilic, B.; Verbridge, S. S.; Cipriany, B. R.; Parpia, J. M.; Craighead, H. G. *Nano Letters*. **2010**, *10*, 2058-2063. Fabrication of a Nanomechanical Mass Sensor Containing a Nanofluidic Channel
- (28) Burg, T. P.; Manalis, S. R. *Applied Physics Letters*. **2003**, *83*, 2698-2700. Suspended microchannel resonators for biomolecular detection
- (29) Burg, T. P.; Godin, M.; Knudsen, S. M.; Shen, W.; Carlson, G.; Foster, J. S.; Babcock, K.; Manalis, S. R. *Nature*. **2007**, *446*, 1066-1069. Weighing of biomolecules, single cells and single nanoparticles in fluid
- (30) Englebienne, P. *Analyst*. **1998**, *123*, 1599-1603. Use of colloidal gold surface plasmon resonance peak shift to infer affinity constants from the interactions between protein antigens and antibodies specific for single or multiple epitopes
- (31) Haes, A. J.; Van Duyne, R. P. *Analytical and Bioanalytical Chemistry*. **2004**, *379*, 920-930. A unified view of propagating and localized surface plasmon resonance biosensors
- (32) Stewart, M. E.; Anderton, C. R.; Thompson, L. B.; Maria, J.; Gray, S. K.; Rogers, J. A.; Nuzzo, R. G. *Chemical Reviews*. **2008**, *108*, 494-521. Nanostructured plasmonic sensors
- (33) Kenausis, G. L.; Voros, J.; Elbert, D. L.; Huang, N. P.; Hofer, R.; Ruiz-Taylor, L.; Textor, M.; Hubbell, J. A.; Spencer, N. D. *Journal of Physical Chemistry B*. **2000**, *104*, 3298-3309. Poly(L-lysine)-g-poly(ethylene glycol) layers on metal oxide surfaces: Attachment mechanism and effects of polymer architecture on resistance to protein adsorption
- (34) Nahshol, O.; Bronner, V.; Notcovich, A.; Rubrecht, L.; Laune, D.; Bravman, T. *Analytical Biochemistry*. **2008**, *383*, 52-60. Parallel kinetic analysis and affinity determination of hundreds of monoclonal antibodies using the ProteOn XPR36
- (35) Rindzevicius, T.; Alaverdyan, Y.; Dahlin, A.; Höök, F.; Sutherland, D. S.; Käll, M. *Nano Letters*. **2005**, *5*, 2335-2339. Plasmonic sensing characteristics of single nanometric holes
- (36) Squires, T. M.; Messinger, R. J.; Manalis, S. R. *Nature Biotechnology*. **2008**, *26*, 417-426. Making it stick: convection, reaction and diffusion in surface-based biosensors
- (37) Wayment, J. R.; Harris, J. M. *Analytical Chemistry*. **2009**, *81*, 336-342. Biotin-Avidin Binding Kinetics Measured by Single-Molecule Imaging
- (38) Bravman, T.; Bronner, V.; Nahshol, O.; Schreiber, G. *Cellular and Molecular Bioengineering*. **2008**, *1*, 216-228. The ProteOn XPR36 (TM) Array System-High Throughput Kinetic Binding Analysis of Biomolecular Interactions
- (39) Jung, L. S.; Nelson, K. E.; Stayton, P. S.; Campbell, C. T. *Langmuir*. **2000**, *16*, 9421-9432. Binding and dissociation kinetics of wild-type and mutant streptavidins on mixed biotin-containing alkylthiolate monolayers

- 
- (40) Cussler, E. L., Cambridge University Press: Cambridge, 1997. *Diffusion: Mass Transfer in Fluid Systems*
- (41) Nath, N.; Chilkoti, A. *Analytical Chemistry*. **2002**, *74*, 504-509. A Colorimetric Gold Nanoparticle Sensor To Interrogate Biomolecular Interactions in Real Time on a Surface
- (42) Cheng, H.; Lei, K. F.; Choy, K. Y.; Chow, L. M. C. *Journal of Micro-Nanolithography Membranes and Moems*. **2009**, *8*. Single-stranded DNA concentration by electrokinetic forces
- (43) Wang, Y. C.; Stevens, A. L.; Han, J. Y. *Analytical Chemistry*. **2005**, *77*, 4293-4299. Million-fold preconcentration of proteins and peptides by nanofluidic filter
- (44) Gouaux, E.; MacKinnon, R. *Science*. **2005**, *310*, 1461-1465. Principles of selective ion transport in channels and pumps
- (45) International Human Genome Sequencing Consortium. *Nature*. **2004**, *431*, 931-945. Finishing the euchromatic sequence of the human genome
- (46) Cooper, M. A. *Journal of Molecular Recognition*. **2004**, *17*, 286-315. Advances in membrane receptor screening and analysis
- (47) Simons, K.; Ikonen, E. *Nature*. **1997**, *387*, 569-572. Functional rafts in cell membranes
- (48) Campbell, S. M.; Crowe, S. M.; Mak, J. *Journal of Clinical Virology*. **2001**, *22*, 217-227. Lipid rafts and HIV-1: from viral entry to assembly of progeny virions
- (49) Fortin, D. L.; Troyer, M. D.; Nakamura, K.; Kubo, S.; Anthony, M. D.; Edwards, R. H. *Journal of Neuroscience*. **2004**, *24*, 6715-6723. Lipid rafts mediate the synaptic localization of alpha-synuclein
- (50) Salaun, C.; James, D. J.; Chamberlain, L. H. *Traffic*. **2004**, *5*, 255-264. Lipid rafts and the regulation of exocytosis
- (51) Alves, I. D.; Park, C. K.; Hruby, V. J. *Current Protein & Peptide Science*. **2005**, *6*, 293-312. Plasmon resonance methods in GPCR signaling and other membrane events
- (52) Hope, M. J.; Bally, M. B.; Webb, G.; Cullis, P. R. *Biochimica et Biophysica Acta*. **1985**, *812*, 55-65. Production of Large Unilamellar Vesicles by a Rapid Extrusion Procedure - Characterization of Size Distribution, Trapped Volume and Ability to Maintain a Membrane-Potential
- (53) Patty, P. J.; Frisken, B. J. *Biophysical Journal*. **2003**, *85*, 996-1004. The Pressure-Dependence of the Size of Extruded Vesicles
- (54) Christensen, S. M.; Stamou, D. *Soft Matter*. **2007**, *3*, 828-836. Surface-based lipid vesicle reactor systems: fabrication and applications
- (55) Boukobza, E.; Sonnenfeld, A.; Haran, G. *The Journal of Physical Chemistry B*. **2001**, *105*, 12165-12170. Immobilization in Surface-Tethered Lipid Vesicles as a New Tool for Single Biomolecule Spectroscopy

- (56) Svedhem, S.; Pfeiffer, I.; Larsson, C.; Wingren, C.; Borrebaeck, C.; Hook, F. *ChemBioChem*. **2003**, *4*, 339-343. Patterns of DNA-labeled and scFv-antibody-carrying lipid vesicles directed by material-specific immobilization of DNA and supported lipid bilayer formation on an Au/SiO<sub>2</sub> template
- (57) Yoshina-Ishii, C.; Boxer, S. G. *Biophysical Journal*. **2003**, *84*, 379A-379A. Spatially encoded and mobile arrays of tethered lipid vesicles
- (58) Stadler, B.; Bally, M.; Grieshaber, D.; Voros, J.; Brisson, A.; Grandin, H. M. *Biointerphases*. **2006**, *1*, 142-145. Creation of a functional heterogeneous vesicle array via DNA controlled surface sorting onto a spotted microarray
- (59) Yoshina-Ishii, C.; Miller, G. P.; Kraft, M. L.; Kool, E. T.; Boxer, S. G. *Journal of the American Chemical Society*. **2005**, *127*, 1356-1357. General method for modification of liposomes for encoded assembly on supported bilayers
- (60) Pfeiffer, I.; Hook, F. *Journal of the American Chemical Society*. **2004**, *126*, 10224-10225. Bivalent cholesterol-based coupling of oligonucleotides to lipid membrane assemblies
- (61) Pfeiffer, I.; Hook, F. *Analytical Chemistry*. **2006**, *78*, 7493-7498. Quantification of oligonucleotide modifications of small unilamellar lipid vesicles
- (62) Bailey, K.; Bally, M.; Leifert, W.; V<sup>r</sup>s, J.; McMurchie, T. *Proteomics*. **2009**, *9*, 2052-2063. G-protein coupled receptor array technologies: Site directed immobilisation of liposomes containing the H1-histamine or M2-muscarinic receptors
- (63) Castellana, E. T.; Cremer, P. S. *Surface Science Reports*. **2006**, *61*, 429-444. Solid supported lipid bilayers: From biophysical studies to sensor design
- (64) Richter, R. P.; Berat, R.; Brisson, A. R. *Langmuir*. **2006**, *22*, 3497-3505. Formation of solid-supported lipid bilayers: An integrated view
- (65) McConnell, H. M.; Watts, T. H.; Weis, R. M.; Brian, A. A. *Biochimica et Biophysica Acta*. **1986**, *864*, 95-106. Supported planar membranes in studies of cell-cell recognition in the immune-system
- (66) Richter, R. P.; Him, J. L. K.; Tessier, B.; Tessier, C.; Brisson, A. R. *Biophysical Journal*. **2005**, *89*, 3372-3385. On the kinetics of adsorption and two-dimensional self-assembly of annexin A5 on supported lipid bilayers
- (67) Rossetti, F. F.; Bally, M.; Michel, R.; Textor, M.; Reviakine, I. *Langmuir*. **2005**, *21*, 6443-6450. Interactions between titanium dioxide and phosphatidyl serine-containing liposomes: Formation and patterning of supported phospholipid bilayers on the surface of a medically relevant material
- (68) Janshoff, A.; Galla, H. J.; Steinem, C. *Angewandte Chemie-International Edition*. **2000**, *39*, 4004-4032. Piezoelectric mass-sensing devices as biosensors - An alternative to optical biosensors?
- (69) Jonsson, M. P.; Dahlin, A. B.; Jönsson, P.; Höök, F. *Biointerphases*. **2008**, *3*, FD30-FD40. Nanoplasmonic Biosensing with Focus on Short-range Ordered Nanoholes in Thin Metal Films

- 
- (70) Przybylo, M.; Sykora, J.; Humpolickova, J.; Benda, A.; Zan, A.; Hof, M. *Langmuir*. **2006**, *22*, 9096-9099. Lipid diffusion in giant unilamellar vesicles is more than 2 times faster than in supported phospholipid bilayers under identical conditions
- (71) Salafsky, J.; Groves, J. T.; Boxer, S. G. *Biochemistry*. **1996**, *35*, 14773-14781. Architecture and function of membrane proteins in planar supported bilayers: A study with photosynthetic reaction centers
- (72) Horton, M. R.; Reich, C.; Gast, A. P.; Radler, J. O.; Nickel, B. *Langmuir*. **2007**, *23*, 6263-6269. Structure and dynamics of crystalline protein layers bound to supported lipid bilayers
- (73) Larsson, C.; Rodahl, M.; Hook, F. *Analytical Chemistry*. **2003**, *75*, 5080-5087. Characterization of DNA immobilization and subsequent hybridization on a 2D arrangement of streptavidin on a biotin-modified lipid bilayer supported on SiO<sub>2</sub>
- (74) Reviakine, I.; Bergsma-Schutter, W.; Morozov, A. N.; Brisson, A. *Langmuir*. **2001**, *17*, 1680-1686. Two-dimensional crystallization of annexin A5 on phospholipid bilayers and monolayers: A solid-solid phase transition between crystal forms
- (75) Reviakine, I.; Brisson, A. *Langmuir*. **2001**, *17*, 8293-8299. Streptavidin 2D crystals on supported phospholipid bilayers: Toward constructing anchored phospholipid bilayers
- (76) Shi, J.; Yang, T.; Kataoka, S.; Zhang, Y.; Diaz, A. J.; Cremer, P. S. *Journal of the American Chemical Society*. **2007**, *129*, 5954-5961. GM1 Clustering Inhibits Cholera Toxin Binding in Supported Phospholipid Membranes
- (77) Atanasov, V.; Atanasova, P. P.; Vockenroth, I. K.; Knorr, N.; Koper, I. *Bioconjugate Chemistry*. **2006**, *17*, 631-637. A molecular toolkit for highly insulating tethered bilayer lipid membranes on various substrates
- (78) Sackmann, E.; Tanaka, M. *Trends in Biotechnology*. **2000**, *18*, 58-64. Supported membranes on soft polymer cushions: fabrication, characterization and applications
- (79) Römer, W.; Steinem, C. *Biophysical Journal*. **2004**, *86*, 955-965. Impedance analysis and single-channel recordings on nano-black lipid membranes based on porous alumina
- (80) Dahlin, A. B.; Jonsson, M. P.; Höök, F. *Advanced Materials*. **2008**, *20*, 1436-1442. Specific Self Assembly of Single Lipid Vesicles in Nanoplasmonic Apertures in Gold
- (81) Groves, J. T.; Ulman, N.; Boxer, S. G. *Science*. **1997**, *275*, 651-653. Micropatterning fluid lipid bilayers on solid supports
- (82) Hovis, J. S.; Boxer, S. G. *Langmuir*. **2001**, *17*, 3400-3405. Patterning and Composition Arrays of Supported Lipid Bilayers by Microcontact Printing

- (83) Lenhert, S.; Sun, P.; Wang, Y. H.; Fuchs, H.; Mirkin, C. A. *Small*. **2007**, *3*, 71-75. Massively parallel dip-pen nanolithography of heterogeneous supported phospholipid multilayer patterns
- (84) Shi, J. J.; Chen, J. X.; Cremer, P. S. *Journal of the American Chemical Society*. **2008**, *130*, 2718-2719. Sub-100 nm Patterning of supported bilayers by nanoshaving lithography
- (85) Atwater, H. A. *Scientific American*. **2007**, *296*, 56-63. The promise of plasmonics
- (86) Vuckovic, J.; Loncar, M.; Scherer, A. *Ieee Journal of Quantum Electronics*. **2000**, *36*, 1131-1144. Surface plasmon enhanced light-emitting diode
- (87) Yeh, D. M.; Huang, C. F.; Chen, C. Y.; Lu, Y. C.; Yang, C. C. *Nanotechnology*. **2008**, *19*. Localized surface plasmon-induced emission enhancement of a green light-emitting diode
- (88) Stipe, B. C.; Strand, T. C.; Poon, C. C.; Balamane, H.; Boone, T. D.; Katine, J. A.; Li, J.-L.; Rawat, V.; Nemoto, H.; Hirotsune, A.; Hellwig, O.; Ruiz, R.; Dobisz, E.; Kercher, D. S.; Robertson, N.; Albrecht, T. R.; Terris, B. D. *Nat Photon*. **2010**, *4*, 484-488. Magnetic recording at 1.5 Pb m<sup>-2</sup> using an integrated plasmonic antenna
- (89) Hägglund, C.; Kasemo, B. *Opt. Express*. **2009**, *17*, 11944-11957. Nanoparticle Plasmonics for 2D-Photovoltaics: Mechanisms, Optimization, and Limits
- (90) Noginov, M. A.; Zhu, G.; Belgrave, A. M.; Bakker, R.; Shalaev, V. M.; Narimanov, E. E.; Stout, S.; Herz, E.; Suteewong, T.; Wiesner, U. *Nature*. **2009**, *460*, 1110-U68. Demonstration of a spaser-based nanolaser
- (91) Zheludev, N. I.; Prosvirnin, S. L.; Papasimakis, N.; Fedotov, V. A. *Nature Photonics*. **2008**, *2*, 351-354. Lasing spaser
- (92) Alu, A.; Engheta, N. *Optics Express*. **2007**, *15*, 3318-3332. Plasmonic materials in transparency and cloaking problems: mechanism, robustness, and physical insights
- (93) El-Sayed, I. H.; Huang, X.; El-Sayed, M. A. *Nano Letters*. **2005**, *5*, 829-834. Surface Plasmon Resonance Scattering and Absorption of anti-EGFR Antibody Conjugated Gold Nanoparticles in Cancer Diagnostics: Applications in Oral Cancer
- (94) Jain, P. K.; El-Sayed, I. H.; El-Sayed, M. A. *Nano Today*. **2007**, *2*, 18-29. Au nanoparticles target cancer
- (95) Willets, K. A.; Van Duyne, R. P. *Annual Review of Physical Chemistry*. **2007**, *58*, 267-297. Localized surface plasmon resonance spectroscopy and sensing
- (96) Linden, S.; Enkrich, C.; Wegener, M.; Zhou, J. F.; Koschny, T.; Soukoulis, C. M. *Science*. **2004**, *306*, 1351-1353. Magnetic response of metamaterials at 100 terahertz
- (97) Maier, S. A., Springer: New York, 2007. *Plasmonics: Fundamentals and Applications*

- 
- (98) Vial, A.; Grimault, A. S.; Macias, D.; Barchiesi, D.; de la Chapelle, M. L. *Physical Review B*. **2005**, *71*. Improved analytical fit of gold dispersion: Application to the modeling of extinction spectra with a finite-difference time-domain method
- (99) Ritchie, R. H. *Physical Review*. **1957**, *106*, 874-881. Plasma losses by fast electrons in thin films
- (100) Homola, J. *Chemical Reviews*. **2008**, *108*, 462-493. Surface plasmon resonance sensors for detection of chemical and biological species
- (101) Zayats, A. V.; Smolyaninov, II; Maradudin, A. A. *Physics Reports-Review Section of Physics Letters*. **2005**, *408*, 131-314. Nano-optics of surface plasmon polaritons
- (102) Kretschmann, E.; Raether, H. *Zeitschrift Fur Naturforschung Part a-Astrophysik Physik Und Physikalische Chemie*. **1968**, *A 23*, 2135-2136. Radiative decay of non radiative surface plasmons excited by light
- (103) Otto, A. *Zeitschrift Fur Physik*. **1968**, *216*, 398-&. Excitation of nonradiative surface plasma waves in silver by method of frustrated total reflection
- (104) Fano, U. *Journal of the optical Society of America*. **1941**, *31*, 213-222. The Theory of Anomalous Diffraction Gratings and of Quasi-Stationary Waves on Metallic Surfaces (Sommerfeld's Waves)
- (105) Ritchie, R. H.; Arakawa, E. T.; Cowan, J. J.; Hamm, R. N. *Physical Review Letters*. **1968**, *21*, 1530-1533. Surface-plasmon resonance effect in grating diffraction
- (106) Wood, R. W. *Phil. Mag*. **1902**, *4*, 396-402. On a remarkable case of uneven distribution of light in a diffraction grating spectrum
- (107) Lord Rayleigh. *Philosophical Magazine Series 6*. **1907**, *14*, 60-65. III. Note on the remarkable case of diffraction spectra described by Prof. Wood
- (108) Renger, J.; Quidant, R.; van Hulst, N.; Palomba, S.; Novotny, L. *Physical Review Letters*. **2009**, *103*. Free-Space Excitation of Propagating Surface Plasmon Polaritons by Nonlinear Four-Wave Mixing
- (109) Liebermann, T.; Knoll, W. *Colloids and Surfaces a-Physicochemical and Engineering Aspects*. **2000**, *171*, 115-130. Surface-plasmon field-enhanced fluorescence spectroscopy
- (110) Rothenhausler, B.; Knoll, W. *Nature*. **1988**, *332*, 615-617. Surface-plasmon microscopy
- (111) Freestone, I.; Meeks, N.; Sax, M.; Higgitt, C. *Gold Bulletin*. **2007**, *40*, 270-277. The Lycurgus Cup - A Roman Nanotechnology
- (112) Mie, G. *Annalen Der Physik*. **1908**, *25*, 377-445. Articles on the optical characteristics of turbid tubes, especially colloidal metal solutions
- (113) Huang, X. H.; Neretina, S.; El-Sayed, M. A. *Advanced Materials*. **2009**, *21*, 4880-4910. Gold Nanorods: From Synthesis and Properties to Biological and Biomedical Applications

- (114) Hanarp, P.; Kall, M.; Sutherland, D. S. *Journal of Physical Chemistry B*. **2003**, *107*, 5768-5772. Optical properties of short range ordered arrays of nanometer gold disks prepared by colloidal lithography
- (115) Meier, M.; Wokaun, A. *Optics Letters*. **1983**, *8*, 581-583. Enhanced fields on large metal particles - Dynamic depolarization
- (116) Myroshnychenko, V.; Rodriguez-Fernandez, J.; Pastoriza-Santos, I.; Funston, A. M.; Novo, C.; Mulvaney, P.; Liz-Marzan, L. M.; Garcia de Abajo, F. J. *Chemical Society Reviews*. **2008**, *37*, 1792-1805. Modelling the optical response of gold nanoparticles
- (117) Riboh, J. C.; Haes, A. J.; McFarland, A. D.; Yonzon, C. R.; Van Duyne, R. P. *Journal of Physical Chemistry B*. **2003**, *107*, 1772-1780. A nanoscale optical biosensor: Real-time immunoassay in physiological buffer enabled by improved nanoparticle adhesion
- (118) Kalyuzhny, G.; Vaskevich, A.; Schneeweiss, M. A.; Rubinstein, I. *Chemistry-a European Journal*. **2002**, *8*, 3849-3857. Transmission surface-plasmon resonance (T-SPR) measurements for monitoring adsorption on ultrathin gold island films
- (119) Chen, S.; et al. *Nanotechnology*. **2009**, *20*, 434015. Ultrahigh sensitivity made simple: nanoplasmonic label-free biosensing with an extremely low limit-of-detection for bacterial and cancer diagnostics
- (120) Dmitriev, A.; Hagglund, C.; Chen, S.; Fredriksson, H.; Pakizeh, T.; Kall, M.; Sutherland, D. S. *Nano Letters*. **2008**, *8*, 3893-3898. Enhanced Nanoplasmonic Optical Sensors with Reduced Substrate Effect
- (121) Larsson, E. M.; Alegret, J.; Kall, M.; Sutherland, D. S. *Nano Letters*. **2007**, *7*, 1256-1263. Sensing characteristics of NIR localized surface plasmon resonances in gold nanorings for application as ultrasensitive biosensors
- (122) Miller, M. M.; Lazarides, A. A. *Journal of Physical Chemistry B*. **2005**, *109*, 21556-21565. Sensitivity of Metal Nanoparticle Surface Plasmon Resonance to the Dielectric Environment
- (123) Link, S.; Mohamed, M. B.; El-Sayed, M. A. *Journal of Physical Chemistry B*. **1999**, *103*, 3073-3077. Simulation of the optical absorption spectra of gold nanorods as a function of their aspect ratio and the effect of the medium dielectric constant
- (124) Haes, A. J.; Zou, S. L.; Schatz, G. C.; Van Duyne, R. P. *Journal of Physical Chemistry B*. **2004**, *108*, 109-116. A nanoscale optical biosensor: The long range distance dependence of the localized surface plasmon resonance of noble metal nanoparticles
- (125) Rindzevicius, T.; Alaverdyan, Y.; Kall, M.; Murray, W. A.; Barnes, W. L. *J. Phys. Chem. C*. **2007**, *111*, 11806-11810. Long-Range Refractive Index Sensing Using Plasmonic Nanostructures
- (126) Svedendahl, M.; Chen, S.; Dmitriev, A.; Käll, M. *Nano Letters*. **2009**, *9*, 4428-4433. Refractometric Sensing Using Propagating versus Localized Surface Plasmons: A Direct Comparison

- 
- (127) Lofas, S.; Johnsson, B. *Journal of the Chemical Society-Chemical Communications*. **1990**, 1526-1528. A novel hydrogel matrix on gold surfaces in surface-plasmon resonance sensors for fast and efficient covalent immobilization of ligands
- (128) McFarland, A. D.; Van Duyne, R. P. *Nano Letters*. **2003**, *3*, 1057-1062. Single silver nanoparticles as real-time optical sensors with zeptomole sensitivity
- (129) Raschke, G.; Kowarik, S.; Franzl, T.; Sonnichsen, C.; Klar, T. A.; Feldmann, J.; Nichtl, A.; Kurzinger, K. *Nano Letters*. **2003**, *3*, 935-938. Biomolecular Recognition Based on Single Gold Nanoparticle Light Scattering
- (130) Shin, Y.-B.; Lee, J.-M.; Park, M.-R.; Kim, M.-G.; Chung, B. H.; Pyo, H.-B.; Maeng, S. *Biosensors and Bioelectronics*. **2007**, *22*, 2301-2307. Analysis of recombinant protein expression using localized surface plasmon resonance (LSPR)
- (131) Haes, A. J.; Chang, L.; Klein, W. L.; Van Duyne, R. P. *Journal of the American Chemical Society*. **2005**, *127*, 2264-2271. Detection of a biomarker for Alzheimer's disease from synthetic and clinical samples using a nanoscale optical biosensor
- (132) Olofsson, L.; Rindzevicius, T.; Pfeiffer, I.; Kall, M.; Hook, F. *Langmuir*. **2003**, *19*, 10414-10419. Surface-Based Gold-Nanoparticle Sensor for Specific and Quantitative DNA Hybridization Detection
- (133) Hicks, E. M.; Zhang, X.; Zou, S.; Lyandres, O.; Spears, K. G.; Schatz, G. C.; Van Duyne, R. P. *The Journal of Physical Chemistry B*. **2005**, *109*, 22351-22358. Plasmonic Properties of Film over Nanowell Surfaces Fabricated by Nanosphere Lithography
- (134) Murray-Méthot, M.-P.; Ratel, M.; Masson, J.-F. *The Journal of Physical Chemistry C*. **2010**, *114*, 8268-8275. Optical Properties of Au, Ag, and Bimetallic Au on Ag Nanohole Arrays
- (135) Becker, J.; Trugler, A.; Jakab, A.; Hohenester, U.; Sonnichsen, C. *Plasmonics*. **2010**, *5*, 161-167. The Optimal Aspect Ratio of Gold Nanorods for Plasmonic Bio-sensing
- (136) Sepulveda, B.; Alaverdyan, Y.; Alegret, J.; Kall, M.; Johansson, P. *Optics Express*. **2008**, *16*, 5609-5616. Shape effects in the localized surface plasmon resonance of single nanoholes in thin metal films
- (137) Rindzevicius, T.; Alaverdyan, Y.; Sepulveda, B.; Pakizeh, T.; Käll, M.; Hillenbrand, R.; Aizpurua, J.; de Abajo, F. J. G. *Journal of Physical Chemistry C*. **2007**, *111*, 1207-1212. Nanohole plasmons in optically thin gold films
- (138) Degiron, A.; Lezec, H. J.; Yamamoto, N.; Ebbesen, T. W. *Optics Communications*. **2004**, *239*, 61-66. Optical transmission properties of a single subwavelength aperture in a real metal
- (139) Park, T. H.; Mirin, N.; Lassiter, J. B.; Nehl, C. L.; Halas, N. J.; Nordlander, P. *Acs Nano*. **2008**, *2*, 25-32. Optical properties of a nanosized hole in a thin metallic film

- (140) Genet, C.; Ebbesen, T. W. *Nature*. **2007**, *445*, 39-46. Light in tiny holes
- (141) Gao, H.; McMahon, J. M.; Lee, M. H.; Henzie, J.; Gray, S. K.; Schatz, G. C.; Odom, T. W. *Opt. Express*. **2009**, *17*, 2334-2340. Rayleigh anomaly-surface plasmon polariton resonances in palladium and gold subwavelength hole arrays
- (142) Degiron, A.; Ebbesen, T. W. *Journal of Optics a-Pure and Applied Optics*. **2005**, *7*, S90-S96. The role of localized surface plasmon modes in the enhanced transmission of periodic subwavelength apertures
- (143) Homola, J., Springer: 2006; Vol. 4. *Surface Plasmon Resonance Based Sensors*
- (144) Chang, S. H.; Gray, S. K.; Schatz, G. C. *Optics Express*. **2005**, *13*, 3150-3165. Surface plasmon generation and light transmission by isolated nanoholes and arrays of nanoholes in thin metal films
- (145) Brolo, A. G.; Gordon, R.; Leathem, B.; Kavanagh, K. L. *Langmuir*. **2004**, *20*, 4813-4815. Surface plasmon sensor based on the enhanced light transmission through arrays of nanoholes in gold films
- (146) Im, H.; Lindquist, N. C.; Lesuffleur, A.; Oh, S. H. *Acs Nano*. **2010**, *4*, 947-954. Atomic Layer Deposition of Dielectric Overlayers for Enhancing the Optical Properties and Chemical Stability of Plasmonic Nanoholes
- (147) Prikulis, J.; Hanarp, P.; Olofsson, L.; Sutherland, D.; Kall, M. *Nano Letters*. **2004**, *4*, 1003-1007. Optical spectroscopy of nanometric holes in thin gold films
- (148) Brian, B.; Sepulveda, B.; Alaverdyan, Y.; Lechuga, L. M.; Kall, M. *Optics Express*. **2009**, *17*, 2015-2023. Sensitivity enhancement of nanoplasmonic sensors in low refractive index substrates
- (149) Jung, L. S.; Campbell, C. T.; Chinowsky, T. M.; Mar, M. N.; Yee, S. S. *Langmuir*. **1998**, *14*, 5636-5648. Quantitative interpretation of the response of surface plasmon resonance sensors to adsorbed films
- (150) Homola, J.; Yee, S. S.; Gauglitz, G. *Sensors and Actuators B-Chemical*. **1999**, *54*, 3-15. Surface plasmon resonance sensors: review
- (151) Dahlin, A.; Zäch, M.; Rindzevicius, T.; Käll, M.; Sutherland, D. S.; Höök, F. *Journal of the American Chemical Society*. **2005**, *127*, 5043-5048. Localized surface plasmon resonance sensing of lipid-membrane-mediated biorecognition events
- (152) Braun, J.; Gompf, B.; Kobiela, G.; Dressel, M. *Physical Review Letters*. **2009**, *103*, 203901. How Holes Can Obscure the View: Suppressed Transmission through an Ultrathin Metal Film by a Subwavelength Hole Array
- (153) Murray-Methot, M. P.; Menegazzo, N.; Masson, J. F. *Analyst*. **2008**, *133*, 1714-1721. Analytical and physical optimization of nanohole-array sensors prepared by modified nanosphere lithography
- (154) Ebbesen, T. W.; Lezec, H. J.; Ghaemi, H. F.; Thio, T.; Wolff, P. A. *Nature*. **1998**, *391*, 667-669. Extraordinary optical transmission through sub-wavelength hole arrays

- 
- (155) Degiron, A.; Ebbesen, T. W. *Optics Express*. **2004**, *12*, 3694-3700. Analysis of the transmission process through single apertures surrounded by periodic corrugations
- (156) Genet, C.; van Exter, M. P.; Woerdman, J. P. *Optics Communications*. **2003**, *225*, 331-336. Fano-type interpretation of red shifts and red tails in hole array transmission spectra
- (157) Gao, H.; Henzie, J.; Odom, T. W. *Nano Letters*. **2006**, *6*, 2104-2108. Direct Evidence for Surface Plasmon-Mediated Enhanced Light Transmission through Metallic Nanohole Arrays
- (158) Pacifici, D.; Lezec, H. J.; Sweatlock, L. A.; Walters, R. J.; Atwater, H. A. *Optics Express*. **2008**, *16*, 9222-9238. Universal optical transmission features in periodic and quasiperiodic hole arrays
- (159) Dahlin, A. B.; Jonsson, P.; Jonsson, M. P.; Schmid, E.; Hook, F. *Acs Nano*. **2008**, *2*, 2174-2182. Synchronized Quartz Crystal Microbalance and Nanoplasmonic Sensing of Biomolecular Recognition Reactions
- (160) Dahlin, A. B.; Tegenfeldt, J. O.; Höök, F. *Analytical Chemistry*. **2006**, *78*, 4416-4423. Improving the instrumental resolution of sensors based on localized surface plasmon resonance
- (161) Sharpe, J. C.; Mitchell, J. S.; Lin, L.; Sedoglavich, H.; Blaikie, R. J. *Analytical Chemistry*. **2008**, *80*, 2244-2249. Gold nanohole array substrates as immunobiosensors
- (162) McMahon, J. M.; Henzie, J.; Odom, T. W.; Schatz, G. C.; Gray, S. K. *Optics Express*. **2007**, *15*, 18119-18129. Tailoring the sensing capabilities of nanohole arrays in gold films with Rayleigh anomaly-surface plasmon polaritons
- (163) Li, J.; Iu, H.; Wan, J. T. K.; Ong, H. C. *Applied Physics Letters*. **2009**, *94*. The plasmonic properties of elliptical metallic hole arrays
- (164) Lesuffleur, A.; Im, H.; Lindquist, N. C.; Oh, S. H. *Applied Physics Letters*. **2007**, *90*. Periodic nanohole arrays with shape-enhanced plasmon resonance as real-time biosensors
- (165) Cole, R. M.; Baumberg, J. J.; Garcia de Abajo, F. J.; Mahajan, S.; Abdelsalam, M.; Bartlett, P. N. *Nano Letters*. **2007**, *7*, 2094-2100. Understanding plasmons in nanoscale voids
- (166) Coyle, S.; Netti, M. C.; Baumberg, J. J.; Ghanem, M. A.; Birkin, P. R.; Bartlett, P. N.; Whittaker, D. M. *Physical Review Letters*. **2001**, *87*. Confined plasmons in metallic nanocavities
- (167) Iu, H.; Li, J.; Ong, H. C.; Wan, J. T. K. *Optics Express*. **2008**, *16*, 10294-10302. Surface plasmon resonance in two-dimensional nanobottle arrays
- (168) Li, J.; Iu, H.; Luk, W. C.; Wan, J. T. K.; Ong, H. C. *Applied Physics Letters*. **2008**, *92*. Studies of the plasmonic properties of two-dimensional metallic nanobottle arrays
- (169) Lee, M. H.; Gao, H. W.; Odom, T. W. *Nano Letters*. **2009**, *9*, 2584-2588. Refractive Index Sensing Using Quasi One-Dimensional Nanoslit Arrays

- (170) Malyarchuk, V.; Stewart, M. E.; Nuzzo, R. G.; Rogers, J. A. *Applied Physics Letters*. **2007**, *90*. Spatially resolved biosensing with a molded plasmonic crystal
- (171) Stewart, M. E.; Mack, N. H.; Malyarchuk, V.; Soares, J.; Lee, T. W.; Gray, S. K.; Nuzzo, R. G.; Rogers, J. A. *Proceedings of the National Academy of Sciences of the United States of America*. **2006**, *103*, 17143-17148. Quantitative multispectral biosensing and 1D imaging using quasi-3D plasmonic crystals
- (172) Yao, J. M.; Stewart, M. E.; Maria, J.; Lee, T. W.; Gray, S. K.; Rogers, J. A.; Nuzzo, R. G. *Angewandte Chemie-International Edition*. **2008**, *47*, 5013-5017. Seeing molecules by eye: Surface plasmon resonance imaging at visible wavelengths with high spatial resolution and submonolayer sensitivity
- (173) Sokolov, K.; Follen, M.; Aaron, J.; Pavlova, I.; Malpica, A.; Lotan, R.; Richards-Kortum, R. *Cancer Research*. **2003**, *63*, 1999-2004. Real-time vital optical imaging of precancer using anti-epidermal growth factor receptor antibodies conjugated to gold nanoparticles
- (174) Hirsch, L. R.; Stafford, R. J.; Bankson, J. A.; Sershen, S. R.; Rivera, B.; Price, R. E.; Hazle, J. D.; Halas, N. J.; West, J. L. *Proceedings of the National Academy of Sciences of the United States of America*. **2003**, *100*, 13549-13554. Nanoshell-mediated near-infrared thermal therapy of tumors under magnetic resonance guidance
- (175) Loo, C.; Lowery, A.; Halas, N.; West, J.; Drezek, R. *Nano Letters*. **2005**, *5*, 709-711. Immunotargeted nanoshells for integrated cancer imaging and therapy
- (176) El-Sayed, I. H.; Huang, X.; El-Sayed, M. A. *Cancer Letters*. **2006**, *239*, 129-135. Selective laser photo-thermal therapy of epithelial carcinoma using anti-EGFR antibody conjugated gold nanoparticles
- (177) Nikoobakht, B.; El-Sayed, M. A. *Chemistry of Materials*. **2003**, *15*, 1957-1962. Preparation and growth mechanism of gold nanorods (NRs) using seed-mediated growth method
- (178) Sun, Y. G.; Xia, Y. N. *Science*. **2002**, *298*, 2176-2179. Shape-controlled synthesis of gold and silver nanoparticles
- (179) Averitt, R. D.; Sarkar, D.; Halas, N. J. *Physical Review Letters*. **1997**, *78*, 4217-4220. Plasmon Resonance Shifts of Au-Coated Au<sub>2</sub>S Nanoshells: Insight into Multicomponent Nanoparticle Growth
- (180) Wang, H.; Brandl, D. W.; Le, F.; Nordlander, P.; Halas, N. J. *Nano Letters*. **2006**, *6*, 827-832. Nanorice: A hybrid plasmonic nanostructure
- (181) Nehl, C. L.; Liao, H. W.; Hafner, J. H. *Nano Letters*. **2006**, *6*, 683-688. Optical properties of star-shaped gold nanoparticles
- (182) Rechberger, W.; Hohenau, A.; Leitner, A.; Krenn, J. R.; Lamprecht, B.; Aussenegg, F. R. *Optics Communications*. **2003**, *220*, 137-141. Optical properties of two interacting gold nanoparticles

- 
- (183) Ghaemi, H. F.; Thio, T.; Grupp, D. E.; Ebbesen, T. W.; Lezec, H. J. *Physical Review B*. **1998**, *58*, 6779. Surface plasmons enhance optical transmission through subwavelength holes
- (184) Chen, Y.; Pepin, A. *Electrophoresis*. **2001**, *22*, 187-207. Nanofabrication: Conventional and nonconventional methods
- (185) Malyarchuk, V.; Hua, F.; Mack, N. H.; Velasquez, V. T.; White, J. O.; Nuzzo, R. G.; Rogers, J. A. *Optics Express*. **2005**, *13*, 5669-5675. High performance plasmonic crystal sensor formed by soft nanoimprint lithography
- (186) Henzie, J.; Lee, M. H.; Odom, T. W. *Nature Nanotechnology*. **2007**, *2*, 549-554. Multiscale patterning of plasmonic metamaterials
- (187) Nagpal, P.; Lindquist, N. C.; Oh, S.-H.; Norris, D. J. *Science*. **2009**, *325*, 594-597. Ultrasoother Patterned Metals for Plasmonics and Metamaterials
- (188) Evans, P.; Hendren, W. R.; Atkinson, R.; Wurtz, G. A.; Dickson, W.; Zayats, A. V.; Pollard, R. J. *Nanotechnology*. **2006**, *17*, 5746-5753. Growth and properties of gold and nickel nanorods in thin film alumina
- (189) Evans, P. R.; Hendren, W. R.; Atkinson, R.; Pollard, R. J. *Nanotechnology*. **2008**, *19*. Optical transmission measurements of silver, silver-gold alloy and silver-gold segmented nanorods in thin film alumina
- (190) Evans, P. R.; Wurtz, G. A.; Atkinson, R.; Hendren, W.; O'Connor, D.; Dickson, W.; Pollard, R. J.; Zayats, A. V. *Journal of Physical Chemistry C*. **2007**, *111*, 12522-12527. Plasmonic Core/Shell nanorod arrays: Subattoliter controlled geometry and tunable optical properties
- (191) Hendren, W. R.; Murphy, A.; Evans, P.; O'Connor, D.; Wurtz, G. A.; Zayats, A. V.; Atkinson, R.; Pollard, R. J. *Journal of Physics-Condensed Matter*. **2008**, *20*. Fabrication and optical properties of gold nanotube arrays
- (192) McPhillips, J.; Murphy, A.; Jonsson, M. P.; Hendren, W. R.; Atkinson, R.; Höök, F.; Zayats, A. V.; Pollard, R. J. *Acs Nano*. **2010**, *4*, 2210-2216. High-Performance Biosensing Using Arrays of Plasmonic Nanotubes
- (193) Doron-Mor, I.; Cohen, H.; Barkay, Z.; Shanzer, A.; Vaskevich, A.; Rubinstein, I. *Chemistry-a European Journal*. **2005**, *11*, 5555-5562. Sensitivity of transmission surface plasmon resonance (T-SPR) spectroscopy: Self-assembled multilayers on evaporated gold island films
- (194) Robbie, K.; Brett, M. J. *Journal of Vacuum Science & Technology a-Vacuum Surfaces and Films*. **1997**, *15*, 1460-1465. Sculptured thin films and glancing angle deposition: Growth mechanics and applications
- (195) Gish, D. A.; Nsiah, F.; McDermott, M. T.; Brett, M. J. *Analytical Chemistry*. **2007**, *79*, 4228-4232. Localized surface plasmon resonance biosensor using silver nanostructures fabricated by glancing angle deposition
- (196) Yang, S. M.; Jang, S. G.; Choi, D. G.; Kim, S.; Yu, H. K. *Small*. **2006**, *2*, 458-475. Nanomachining by colloidal lithography
- (197) Lee, S. H.; Bantz, K. C.; Lindquist, N. C.; Oh, S. H.; Haynes, C. L. *Langmuir*. **2009**, *25*, 13685-13693. Self-Assembled Plasmonic Nanohole Arrays

- (198) Jensen, T. R.; Malinsky, M. D.; Haynes, C. L.; Van Duyne, R. P. *Journal of Physical Chemistry B*. **2000**, *104*, 10549-10556. Nanosphere lithography: Tunable localized surface plasmon resonance spectra of silver nanoparticles
- (199) Shumaker-Parry, J. S.; Rochholz, H.; Kreiter, M. *Advanced Materials*. **2005**, *17*, 2131-2134. Fabrication of crescent-shaped optical antennas
- (200) Aizpurua, J.; Hanarp, P.; Sutherland, D. S.; Kall, M.; Bryant, G. W.; de Abajo, F. J. G. *Physical Review Letters*. **2003**, *90*. Optical properties of gold nanorings
- (201) Fredriksson, H.; Alaverdyan, Y.; Dmitriev, A.; Langhammer, C.; Sutherland, D. S.; Zaech, M.; Kasemo, B. *Advanced Materials*. **2007**, *19*, 4297-4302. Hole-mask colloidal lithography
- (202) Hanarp, P.; Sutherland, D. S.; Gold, J.; Kasemo, B. *Colloids and Surfaces a-Physicochemical and Engineering Aspects*. **2003**, *214*, 23-36. Control of nanoparticle film structure for colloidal lithography
- (203) Hulteen, J. C.; van Duyne, R. P. *Journal of Vacuum Science & Technology a-Vacuum Surfaces and Films*. **1995**, *13*, 1553-1558. Nanosphere Lithography - A Materials General Fabrication Process for Periodic Particle Array Surfaces
- (204) Jensen, T. R.; Duval, M. L.; Kelly, K. L.; Lazarides, A. A.; Schatz, G. C.; Van Duyne, R. P. *Journal of Physical Chemistry B*. **1999**, *103*, 9846-9853. Nanosphere Lithography: Effect of the External Dielectric Medium on the Surface Plasmon Resonance Spectrum of a Periodic Array of Silver Nanoparticles
- (205) Svedendahl, M.; Chen, S.; Dmitriev, A.; Kall, M. *Nano Letters*. **2009**, *9*, 4428-4433. Refractometric Sensing Using Propagating versus Localized Surface Plasmons: A Direct Comparison
- (206) Curry, A.; Nusz, G.; Chilkoti, A.; Wax, A. *Optics Express*. **2005**, *13*, 2668-2677. Substrate effect on refractive index dependence of plasmon resonance for individual silver nanoparticles observed using darkfield microscopy
- (207) Nusz, G. J.; Marinakos, S. M.; Curry, A. C.; Dahlin, A.; Hook, F.; Wax, A.; Chilkoti, A. *Analytical Chemistry*. **2008**, *80*, 984-989. Label-free plasmonic detection of biomolecular binding by a single gold nanorod
- (208) Dahlin, A. B.; Chen, S.; Jonsson, M. P.; Gunnarsson, L.; Kall, M.; Hook, F. *Analytical Chemistry*. **2009**, *81*, 6572-6580. High-Resolution Microspectroscopy of Plasmonic Nanostructures for Miniaturized Biosensing
- (209) Johansen, K.; Stalberg, R.; Lundstrom, I.; Liedberg, B. *Measurement Science and Technology*. **2000**, *11*, 1630-1638. Surface plasmon resonance: instrumental resolution using photo diode arrays
- (210) Höök, F.; Kasemo, B., The QCM technique for biomacromolecular recognition: technical and theoretical aspects. In *The Springer Series on Chemical Sensors and Biosensors*, Wolfbeis, O. S., Ed. 2006.

- 
- (211) Nomura, T.; Okuhara, M. *Analytica Chimica Acta*. **1982**, *142*, 281-284. Frequency-shifts of piezoelectric quartz crystals immersed in organic liquids
- (212) Keller, C. A.; Kasemo, B. *Biophysical Journal*. **1998**, *75*, 1397-1402. Surface specific kinetics of lipid vesicle adsorption measured with a quartz crystal microbalance
- (213) Sauerbrey, G. *Zeitschrift Fur Physik*. **1959**, *155*, 206-222. Verwendung von schwingquarzen zur wagung dunner schichten und zur mikrowagung
- (214) Reimhult, E.; Larsson, C.; Kasemo, B.; Hook, F. *Analytical Chemistry*. **2004**, *76*, 7211-7220. Simultaneous surface plasmon resonance and quartz crystal microbalance with dissipation monitoring measurements of biomolecular adsorption events involving structural transformations and variations in coupled water
- (215) Rodahl, M.; Kasemo, B. *Review of Scientific Instruments*. **1996**, *67*, 3238-3241. A simple setup to simultaneously measure the resonant frequency and the absolute dissipation factor of a quartz crystal microbalance
- (216) Rodahl, M.; Kasemo, B. *Sensors and Actuators A: Physical*. **1996**, *54*, 448-456. On the measurement of thin liquid overlayers with the quartz-crystal microbalance
- (217) Voinova, M. V.; Rodahl, M.; Jonson, M.; Kasemo, B. *Physica Scripta*. **1999**, *59*, 391-396. Viscoelastic acoustic response of layered polymer films at fluid-solid interfaces: Continuum mechanics approach
- (218) Hall, W. P.; Anker, J. N.; Lin, Y.; Modica, J.; Mrksich, M.; Van Duyne, R. P. *Journal of the American Chemical Society*. **2008**, *130*, 5836-5837. A calcium-modulated plasmonic switch
- (219) Wang, G.; Rodahl, M.; Edvardsson, M.; Svedhem, S.; Ohlsson, G.; Hook, F.; Kasemo, B. *Review of Scientific Instruments*. **2008**, *79*, 075107-7. A combined reflectometry and quartz crystal microbalance with dissipation setup for surface interaction studies
- (220) Eftekhari, F.; Escobedo, C.; Ferreira, J.; Duan, X.; Girotto, E. M.; Brolo, A. G.; Gordon, R.; Sinton, D. *Analytical Chemistry*. **2009**, *81*, 4308-4311. Nanoholes As Nanochannels: Flow-through Plasmonic Sensing
- (221) Yanik, A. A.; Huang, M.; Artar, A.; Chang, T. Y.; Altug, H. *Applied Physics Letters*. **2010**, *96*. Integrated nanoplasmonic-nanofluidic biosensors with targeted delivery of analytes
- (222) Gu, R. Y.; Li, M.; Su, C. C.; Long, F.; Routh, M. D.; Yang, F.; McDermott, G.; Yu, E. W. *Acta Crystallographica Section F-Structural Biology and Crystallization Communications*. **2008**, *64*, 584-588. Conformational change of the AcrR regulator reveals a possible mechanism of induction
- (223) Branden, M.; Dahlin, S.; Hook, F. *ChemPhysChem*. **2008**, *9*, 2480-2485. Label-Free Measurements of Molecular Transport across Liposome Membranes using Evanescent-Wave Sensing

- (224) Brändén, M.; Tabaei, S. R.; Fischer, G.; Neutze, R.; Höök, F. *Biophysical Journal*. **2010**, *99*, 1-10. Refractive-Index Based Screening of Membrane-Protein Mediated Transfer across Biological Membranes
- (225) Jönsson, P.; Jonsson, M. P.; Höök, F. *Nano Letters*. **2010**. Sealing of Sub-Micrometer Wells by a Shear-Driven Lipid Bilayer
- (226) Schmitt, E. K.; Nurnabi, M.; Bushby, R. J.; Steinem, C. *Soft Matter*. **2008**, *4*, 250-253. Electrically insulating pore-suspending membranes on highly ordered porous alumina obtained from vesicle spreading
- (227) Han, X. J.; Studer, A.; Sehr, H.; Geissbuhler, I.; Di Berardino, M.; Winkler, F. K.; Tiefenauer, L. X. *Advanced Materials*. **2007**, *19*, 4466-4470. Nanopore arrays for stable and functional free-standing lipid bilayers
- (228) Dekker, C. *Nat Nano*. **2007**, *2*, 209-215. Solid-state nanopores
- (229) McNally, B.; Wanunu, M.; Meller, A. *Nano Letters*. **2008**, *8*, 3418-3422. Electromechanical Unzipping of Individual DNA Molecules Using Synthetic Sub-2 nm Pores
- (230) Keyser, U. F.; Koeleman, B. N.; van Dorp, S.; Krapf, D.; Smeets, R. M. M.; Lemay, S. G.; Dekker, N. H.; Dekker, C. *Nat Phys*. **2006**, *2*, 473-477. Direct force measurements on DNA in a solid-state nanopore
- (231) Hall, A. R.; van Dorp, S.; Lemay, S. G.; Dekker, C. *Nano Letters*. **2009**, *9*, 4441-4445. Electrophoretic Force on a Protein-Coated DNA Molecule in a Solid-State Nanopore
- (232) Wu, D. P.; Steckl, A. J. *Lab on a Chip*. **2009**, *9*, 1890-1896. High speed nanofluidic protein accumulator
- (233) Stein, D.; Deurvorst, Z.; van der Heyden, F. H. J.; Koopmans, W. J. A.; Gabel, A.; Dekker, C. *Nano Letters*. **2010**, *10*, 765-772. Electrokinetic Concentration of DNA Polymers in Nanofluidic Channels
- (234) Levene, M. J.; Korlach, J.; Turner, S. W.; Foquet, M.; Craighead, H. G.; Webb, W. W. *Science*. **2003**, *299*, 682-686. Zero-Mode Waveguides for Single-Molecule Analysis at High Concentrations
- (235) Edel, J. B.; Wu, M.; Baird, B.; Craighead, H. G. *Biophysical Journal*. **2005**, *88*, L43-L45. High spatial resolution observation of single-molecule dynamics in living cell membranes
- (236) Jensen, T. R.; Van Duyne, R. P.; Johnson, S. A.; Maroni, V. A. *Applied Spectroscopy*. **2000**, *54*, 371-377. Surface-enhanced infrared spectroscopy: A comparison of metal island films with discrete and nondiscrete surface plasmons